REPORT DOCUMENTATION PAGE

Form Approved OMB No. 0704-0188

1. REPORT DATE *(DD-MM-YYYY)* 15-07-2010	2. REPORT TYPE Final Report	3. DATES COVERED *(From – To)* 02-Feb-07 - 15-Jul-10

4. TITLE AND SUBTITLE	5a. CONTRACT NUMBER
High-temperature ceramic matrix composites with high corrosion resistance	STCU Registration No: P-286
	5b. GRANT NUMBER
	5c. PROGRAM ELEMENT NUMBER

6. AUTHOR(S)	5d. PROJECT NUMBER
Mr. Oleg Nikolayevich Grigoriev	**5d. TASK NUMBER**
	5e. WORK UNIT NUMBER

7. PERFORMING ORGANIZATION NAME(S) AND ADDRESS(ES)	8. PERFORMING ORGANIZATION REPORT NUMBER
Institute for Problems of Materials Science Krzhyzhanovsky str., 3 Kiev 03680 Ukraine	N/A

9. SPONSORING/MONITORING AGENCY NAME(S) AND ADDRESS(ES)	10. SPONSOR/MONITOR'S ACRONYM(S)
EOARD Unit 4515 BOX 14 APO AE 09421	
	11. SPONSOR/MONITOR'S REPORT NUMBER(S) STCU 06-8012

12. DISTRIBUTION/AVAILABILITY STATEMENT

Approved for public release; distribution is unlimited.

13. SUPPLEMENTARY NOTES

14. ABSTRACT

This report results from a contract tasking Institute for Problems of Materials Science as follows: In this Project the new composites of ZrB2-SiC system will be created, their structure and high-temperature mechanical and corrosion properties will be studied up to 1600 C. The effect of (Zr, Mo)Si2 additives on both high-temperature corrosion resistance and high-temperature strength of composites above will be investigated. The new technologies of protective coatings will be developed with the use of thermal-chemical and also electrochemical (polarization) methods. The results obtained will be used for the development of a model of high-temperature oxidation of chosen ceramic systems. We are planning in this Project the obtaining of dense composites by activated sintering under pressure (hot pressing) using nanosized row materials with MoSi2 additives. Low porosity, composition modification and protective coating formation at high-temperature treatment will provide high level of strength and enhanced corrosion resistance. This Project also supposes the development of theoretical speculation for high-temperature oxidation parameters determination using both specific models and experimental kinetic curves of oxide layer growth for the systems under study. Such modeling concerns the peculiarities of oxide layer formation at the scale-ceramic substrate boundary including the investigation of oxide layers stability as to pittings, voids and other real scale defects. As a result of Project fulfillment a new knowledge for structural state and properties of ceramic composites management techniques will be obtained. So, new structural ceramic materials with higher working temperatures will be developed and studied in details.

15. SUBJECT TERMS

EOARD, Materials, Laminates and Composite Materials

16. SECURITY CLASSIFICATION OF:			17. LIMITATION OF ABSTRACT	18, NUMBER OF PAGES	19a. NAME OF RESPONSIBLE PERSON
a. REPORT UNCLAS	**b. ABSTRACT** UNCLAS	**c. THIS PAGE** UNCLAS	UL	150	WYNN SANDERS, Maj, USAF
					19b. TELEPHONE NUMBER *(Include area code)* +44 (0)1895 616 007

Standard Form 298 (Rev. 8/98)
Prescribed by ANSI Std. Z39-18

FINAL REPORT

High-temperature ceramic matrix composites with high corrosion resistance

Project manager: Oleg Grigoriev, Dr. Sci., Corresponding member of NAS

Phone: +38-044-4241321, Fax: +38-044-4242131, E-mail:oleggrig@ipms.kiev.ua

Institutions: Institute for Problems of Materials Science

Financing parties: USA

Operative commencement date: 01.02.2007

Project duration: 3 years

Date of submission: 30.05.2010

Table of Contents

List of Figures

Fig. 3.52. Samples of ceramics after oxidation, SiCz and SiCst – silicon carbide from different manufacturers.

Fig.3.53. Oxidation kinetics of ZrB_2-5%$ZrZi_2$ (a), ZrB_2-15%$ZrSi_2$ (b) and ZrB_2-50%$ZrSi_2$ (c) ceramics in oxygen; T, °C: a) 1-1000, 2-1100, 3-800; b) 1-700, 2-900, 3-1100, 4-1200; c)1-600, 2-850, 3-1000, 4-1200.

Fig.3.54. Curves of isothermal oxidation of US4 (dark blue curve) and USS4 (magenta curve) samples at 1500 °C.

Fig. 3.55. SEM microphotograph of cross section of oxidized US3 sample surface after 30 min oxidation at 1500 °C. Oxide film has two-layer structure.

Fig.3.56. XRD pattern of US4 ceramics after oxidation at 1500 °C, 50 h.

Fig.3.57. XRD pattern of USS4 ceramics after oxidation at 1500 °C, 50 h.

Fig. 3.58. Structure of oxidation scale according to Chamberlain (2005).

Fig. 3.59. Phase relations in layers of oxide scale.

Fig. 3.60. Microphotograph of typical oxidation scale and chemical elements mapping.

Fig. 3.61. Top surface view of ZrB_2-SiC-$ZrSi_2$ ceramics after oxidation at 1500 °C for 35 h in pure oxygen.

Fig. 3.62. Kinetic dependences of sample mass gain on oxidation time for SiC-ZrB_2-$ZrSi_2$ composites of different composition.

Fig. 3.63. Dependence of mass gain on $ZrSi_2$ content (vol.%) in charge for oxidation at 1500 °C for 50 h in oxygen.

Fig. 3.64. Top surface view for USS 41 composite after oxidation

Fig. 3.65. Top surface view for USS 43 composite after oxidation.

Fig. 3.66. Top surface view for USS 46 composite after oxidation.

Fig. 3.67. View of USS 43 ceramics sample after oxidation in oxygen at 1500 °C for 24 h (from top to below): 1) pure SiO_2 scale, extremely variable; 2) zone, outlining original sample geometry with a mush of ZrO_2 in silica; 3) SiC-depleted porous zone with a high morphology; 4) unaltered material.

Fig. 3.68. View of USS 43 (a) and USS 41 (b) ceramics sample, oxidized in oxygen at 1500 °C for 24 h.

Fig.3.69. Impurity check (on USS41, 24 h, 1500 °C, O_2).

Fig. 3.70. The view of ceramics surface after oxidation in the oxygen flow in the presence of Fe_2O_3, NiO, Al_2O_3 oxides and Na_2CO_3.

Summary

With the aid of optimization of ZrB_2-SiC-$ZrSi_2$ ceramics composition and in order to achieve their highest properties we carried out the investigations concerning the effect of ceramics composition (the $ZrB_2/ZrSi_2$ ratio) on their structure and properties. The investigations of the mechanical properties of ceramics mentioned above – hardness, strength, fracture toughness – were carried out in detail. The sintering of powders was fulfilled under pressure in graphite dies. The temperature range of sintering process was $1650 – 2100^oC$, duration of sintering – $15 – 20$ min. The optimum regimes of sintering for materials of $ZrB_2 – SiC$ and $ZrB_2 – ZrSi_2 – SiC$ systems were established.

The introduction of $ZrSi_2$ (all other factors being the same) assists in activating sintering and therefore reduces porosity in ZrB_2-SiC based ceramics and widens the range of silicon carbide concentrations where formation of pore-free materials has been observed. The structure of these materials is heterogeneous. The final phase composition depends on the amount of $ZrSi_2$ introduced. If the zirconium silicide content is lower than 8 vol.% the phase composition is ZrB_2-SiC-Zr(Hf)C(B), otherwise, the phase composition is ZrB_2-SiC-Zr(Hf)C(B)-$ZrSi_{2(modified)}$.

For the raw materials and hot pressing conditions used in this study, the content of zirconium silicide is optimal at about 2 vol.%. At higher zirconium silicide contents (above 8 vol.%) degradation of the additional liquid phase in the resulting ceramics, during longer isothermal holds at elevated temperatures, was discovered. Further, degradation of the grain boundary amorphous phase resulted in the appearance of porosity at the grain-boundaries and a decrease in bending strength.

The mechanical properties of ZrB_2-SiC and ZrB_2-SiC-$ZrSi_2$ hot pressed ceramics (with grain sizes 10–15 µm) in the composition range 0–60 and 0–14 vol. % of SiC and $ZrSi_2$, respectively, were studied. The introduction of SiC improves mechanical properties (hardness 18–20 GPa, bend strengths 400–500 MPa, contact strength in tension 400–650 MPa) and the maximum of strength characteristics is formed at high SiC content. The dependencies of mechanical properties of ceramics on silicon carbide content are in a good accordance with conclusions of a thermo-mechanical model based on the mechanical properties of heterogeneous ceramics. The addition of $ZrSi_2$ (up to 4 vol. %) slightly affects bending strength of ceramics but essentially improves the contact strength and homogeneity characteristic (Weibull modulus from 7 to 24) at low

temperature. It has been established during strength testings of ZrB_2–$MoSi_2$ composite samples that the introduction of insignificant amount of second phase has essentially heightened their strength, the maximum strengths was reached at 44.0 vol. % $MoSi_2$. However, the high-temperature (1400 °C) strength decreases from ~430 MPa to ~320 MPa for double (ZrB_2-SiC) and triple (ZrB_2-SiC-$ZrSi_2$) as well as for ZrB_2–$MoSi_2$ ceramics.

The investigations indicated that ZrB_2–SiC–$ZrSi_2$ ceramics with the optimal composition (2wt% of $ZrSi_2$), had the best oxidation resistance for long-duration (50 h) exposure to pure oxygen at 1500 °C. The ZrB_2–SiC–$ZrSi_2$ ceramic had 3.4 times higher resistance to oxidation based on mass gain compared to the ZrB_2–SiC. In comparison with other non-oxide ceramics, such oxidation resistance is exceptionally high (the mass gain is $<10mg/cm^2$ at 1500 °C after 50 h oxidation in pure oxygen). The oxidation process had kinetics that showed nearly ideal parabolic behavior for long times.

The investigation of structure and phase composition of the surface layers formed in the oxygen flux at 1500 °C shows that the oxide scale corresponds to the Chamberlain's model. With the aid DTA- and TG-methods as well a XRD and petrographic analyses of scale compositions the kinetics and mechanism of high-temperature oxidation in air up to 1700 °C of ZrB_2-SiC-$ZrSi_2$ ceramics have been studied. The five-stage oxidation mechanism has been established at the consecutive increase of samples heating with the rate 20 °/min. The succession of the processes proved to be a the following:1) oxygen desorption-adsorption; 2) formation of ZrO_2 and B_2O_3 oxides; 3) formation of α-SiO_2 crystobalite and $ZrSiO_4$ zircon; 4) formation of SiO_2 amorphous phase; 5) formation of upper borosilicate protective film with ZrO_2 and $ZrSiO_4$ inclusions at the SiC content < 40 mas.%. It has been shown that the small additives of $ZrSi_2$ (< 4 mas.%) in interval samples significantly lower the oxidation rate at the first oxidation stages.

The modified equations of oxidation kinetics were derived. The modification took into account uncertainties and scattering of results at the initial oxidation stage. Based on the experimental data a new oxidation model was developed. The model predictions showed good agreement of calculated and experimental oxidation kinetic curves. It was shown that the increase of oxidation resistance of triple ceramics (ZrB_2–SiC–$ZrSi_2$) is due to decreased oxygen diffusion rate in subsurface layer. The role of the subsurface layer is enhanced by the fact that this layer is more uniform in thickness compared with the outer layer of glass which is varied in thickness up to discontinuity. Comparison with experimental data shows that the calculated model parameters fully correspond to the physical meaning of the oxidation process.

Taking into account a possible use of ZrB_2-SiC-$ZrSi_2$ ceramics as material for gas turbine engines, the influence of Fe_2O_3, NiO, Al_2O_3 oxide and Na_2CO_3 salt chemical impurities on the ceramic samples surface and on the peculiarities of oxidation character and their surface damages have been established. It has been shown that the Na_2CO_3 and NiO additives, in fact, have not practically affected high-temperature oxidation of ZrB_2-SiC-$ZrSi_2$ ceramics while the Al_2O_3 and Fe_2O_3 ones have had significant influence on the scale formed.

The thickness, composition, morphology and structure of different oxide layers formed on the ZrB_2-$MoSi_2$ ceramics samples of different composition oxidized in the air at high temperatures (up to 1600-1700 °C) may significantly differ from each other. In ceramics ZrB_2-14 mas. % $MoSi_2$ a double layer scale formed during the oxidation: the upper is amorphous sublayer of silica; the second sublayer is a dense scale of needle-shaped ZrO_2 crystals, which reinforced surface and provided additional protection against oxidation.

The electrochemical (anodic) oxidation in 3% NaCl solution of hot-pressed ZrB_2, $MoSi_2$, 93 vol.% ZrB_2 – 7 vol.% $MoSi_2$, 56 vol.% ZrB_2 – 44 vol.% $MoSi_2$ ceramics and fused ZrB_2 samples have been studied using potential-dynamic polarization curve method. It has been shown that the all of ceramics studied are characterized by the high enough corrosion resistance in the 3% NaCl solution, i.e. also in the marine water. The electrochemical oxidation data obtained, on the whole, proved to be in agreement with the high-temperature oxidation data for the ceramics mentioned above. For the $MoSi_2$ oxidation the kinetic data obtained can be explained in the terms of Mott-Cabrera theory for thin oxide films formation.

1. Introduction

Ceramic borides, such as hafnium diboride (HfB_2) and zirconium diboride (ZrB_2), are members of a family of materials with extremely high melting temperatures (above 3200 °C) which have been referred to as Ultra High Temperature Ceramics (UHTCs). Being resistant to thermal shock and oxidation, UHTCs are regarded as potential candidates for thermal protection systems (TPS), leading edges, and propulsion components in future hypersonic flight vehicles and reentry vehicles and other structural application. At present the developments in the field of UHTCs is one of the focal points of material science. In studies of diboride based UHTCs, recent research has demonstrated that mechanical properties and high-temperature oxidation/ablation resistance are enhanced with the addition of silicon carbide (SiC) over a wide range of SiC content[1-5]. A large number of studies have been devoted to a search for additives to the diborides to work as a sintering activators and corrosion inhibitors[6-24]. The introduction of silicon carbide into ZrB_2 (20-25 vol.%) improves its resistance to high-temperature oxidation. Protective oxide film in the ZrB_2 - SiC system consists of a continuous and dense corrosion-resistant (SiO_2-B_2O_3) glassy film with the fine grains of ZrO_2 scattered in it. The addition of some nitrides (Si_3N_4, AlN, ZrN), silicides ($MoSi_2$, $ZrSi_2$) and carbides (B_4C, WC) in small quantities (up to 5%) have also been shown to enhance sintering and strength of ZrB_2-SiC composites[6-12]. The achieved level of mechanical and service properties proved to be high enough (strength at room temperature is equal to 1000 MPa and more and ~ 500 MPa at 1500 °C[3]. However, the oxidation resistance of most studied $Zr(Hf)B_2$-SiC ceramics is insufficient to ensure the long-time resource at working temperatures above 1500 °C. The search of means to increase the resistance of these ceramics to high-temperature oxidation has shown a promising direction –introduction to their composition of secondary borides (TaB_2)[24], in the presence of which borosilicate glass films modified by second metal were formed, ensuring the reduction of oxidation rate.

In past studies of this research group[2,11,12], the activation of sintering of ZrB_2-SiC ceramics in the presence of boron carbide has been investigated. The results showed that boron carbide activates sintering and causes reduction reactions with surface oxide impurities. It also promotes grain boundary refining and an increase in high-temperature strength. The eutectic temperature for the SiC - ZrB_2 - B_4C system is about 2090 °C[13] and hot pressing over a range of temperatures was accompanied by a partial melting of the compositions. The optimum temperature for hot pressing (1950 – 2050 °C) in the considered system depends on the material composition. For each composition, it was found to be within a rather narrow temperature range (± 20 °C). Deviation

from the optimum temperature causes either porosity or grain size growth, accompanied by a sharp decrease in strength. The adjusted hot pressing regimes ensure the improvement of ceramics which have porosity in the range of 1-3%. These ceramics did not show a degradation in strength over a wide range of testing temperatures (up to 1400 °C), which can be associated with the enhanced purity of the grain boundaries.

The research has shown that the ZrB_2-$ZrSi_2$ system is characterized by a lower oxidation rate compared with pure ZrB_2[14,15]. Addition of Zr, Mo, Ta silicides and others improve sinterability, as well as oxidation resistance of ZrB_2- SiC ceramics[16-22]. It is well known that $ZrSi_2$ additives (20-40 vol. %) promote sintering activation with formation of dense ceramics even at 1550 °C[9,23]. However, the range of application of such ceramics is limited by low melting temperature of $ZrSi_2$. In this study the amount of silicide additive is limited by several percents which is enough for liquid-phase sintering of these ceramics at T>1800 °C. The disilicides additives proved to be especially efficient because they are alternative (beside SiC) sources of silicon for SiO_2 formation. The enhanced oxidation resistance of ceramics with silicide additives may be explained in the following ways: 1) metal oxide, for example Ta_2O_5, formed at oxidation of $TaSi_2$, in the borosilicate glass leads to formation of immiscible phase-separated glasses with higher viscosity and lower permeability to oxygen[16,22]; 2) metal addition (in particular, Ta) results in a substitution of Ta on the Zr site in ZrO_2, reducing concentration of oxygen vacancies in ZrO_2. The lower concentration of oxygen vacancies decreases oxygen transport through the growing oxide scale[21]; 3) in the case of silicides ($ZrSi_2$, $MoSi_2$, $CrSi_2$) presence, $ZrSiO_4$ is formed at oxidation, and it promotes the increase of oxidation resistance[14,15].

The effect of additives of silicides on the mechanical properties of ceramics was investigated to a lesser extent. A wide combination of technical requirements is imposed on high performance structural ceramics materials. Sufficiently low creep rate as well as high resistance to high-temperature oxidation and corrosion, high level of strength and fracture toughness are among the most important ones. This complex set of material property requirements, in turn, leads to a combination of contradictory and often incompatible demands to the structural state and composition of ceramics. Therefore, development of structural ceramics always involves optimization of the structural state and composition on the basis of some compromise in properties.

The main goal of the current research is the investigation and estimation of: 1) potential benefits from the introduction of silicide additives (for example, $ZrSi_x$) in ZrB_2-SiC ceramics for the activation of sintering and reduction of hot pressing temperature; 2) mechanical properties,

STCU   *PROJECT P286 – FINAL REPORT*   PAGE 14

depending on composition and structure characteristics of ZrB_2-$SiC(ZrSi_2)$ ceramics; 3) ability of a silicide additive ($ZrSi_2$) in ZrB_2-SiC ceramics to decrease the oxidation rate at temperatures above 1400 °C, when oxidation mechanisms proposed by Talmy et. al.[16] and Opila et. al.[21] do not work. In order to optimize the composition of the ceramics for the study, initial sintering experiments with varying ratios of ZrB_2-$ZrSi_2$ and ZrB_2-SiC were carried out. Besides, in the frame of investigation we obtained sets of samples of ZrB_2–$MoSi_2$ system. We studied the peculiarities of mechanical behavior and high-temperature corrosion of both ZrB_2–SiC–$ZrSi_2$ triple and ZrB_2–$MoSi_2$ binary ceramics. Because of this, now we studied the influence of $ZrSi_2$ and $MoSi_2$ additives on the strength and corrosion characteristics.

The processes of high-temperature oxidation were studied in the regime of long-term isothermal exposure that allowed investigate experimentally (and theoretically) the kinetics of oxidation in pure oxygen. A new oxidation model based on the available experimental data is presented.

In the framework of this report the study of influence of different impurities on the oxidation rate of these ceramics in the isothemal conditions was fulfilled. Despite the fact that mechanisms of ceramics oxidation have been studied satisfactorily enough, the effect of impurities on ceramic surfaces on the oxidation process was not established. We have studied the influence of some metal oxides and salt additives which can be present on the surface of ceramic samples under their high-temperature oxidation in oxygen at the temperature up to 1500 °C. These may be the components of fuel combustion products, small parts of engine as a result of its partial wear, namely Fe_2O_3, NiO oxide particles as well as technological impurities which may be present at the sample surface on the account of ceramics manufacturing. This study allows predict the oxidation process under real operating conditions of the material.

The next our goal had to be the study of mechanism of high-temperature oxidation in air up to 1700 °C of 35 mas.% ZrB_2-65 mas.% SiC; 36.8 mas.% ZrB_2-60 mas.% SiC – 3.2 mas.% $ZrSi_2$ and 67.3 mas.% ZrB_2-26 mas.% SiC – 6.7 mas.% $ZrSi_2$ ceramics with the aid of DTA- and TG-methods. Also we have investigated the mechanism of high-temperature oxidation up to 1600 °C of two kinds of ZrB_2- $MoSi_2$ ceramics: with high and low $MoSi_2$ content, i.e. with 44 and 14 mas.% $MoSi_2$. The investigations in the regime of continuous heating of the samples up to 1600-1650 °C enabled us to establish the consecution of chemical reactions and processes taking place at ceramics oxidation during the temperature rise.

As the mechanisms of electrochemical oxidation of ceramics on the base of binary refractory compounds (borides, silicides, etc.) have a lot of similar to their high-temperature oxidation, we

also had to study the anodic oxidation in 3% NaCl solution, imitating the marine water, of ceramic samples of ZrB_2–$MoSi_2$ system with comparatively small and large content of ZrB_2 and $MoSi_2$.

As the definition of high-temperature oxidation process peculiarities and mechanisms of electrochemical oxidation of binary ceramics samples, in particular for ZrB_2–$MoSi_2$ system, is possible only on the base of study of every component (ZrB_2 and $MoSi_2$) oxidation in detail, the significant care should be given to the study of oxidation mechanisms for individual zirconium boride and, especially, molybdenum disilicide.

2. Methods, Assumptions, and Procedures

In the framework of the Project the manufacturing conditions and properties of ceramic composites of ZrB_2 - SiC - $ZrSi_2$, ZrB_2 - SiC - $MoSi_2$ as well as SiC - ZrB_2 - B_4C systems are studied.

2.1. Characteristics of powders.

Two kinds of α-SiC powders were used: 1) technical abrasive powders, M5 grade, produced by the Zaporozhie Abrasives Plant, Ukraine and 2) powders of UF05 and UF10 grades from the N.C. Starck Company, Germany, designed for ceramics production. Both powders were mixtures of polytypes: mainly, 6H, 15R and 3C.

Some powder properties in the as-received state are given in Table 2.1. Besides, the synthesis of ZrB_2, $ZrSi_2$, and $MoSi_2$ powder sets has been carried out at IPMS using reactions of carbon-thermal reduction of oxides. The corresponding powders obtained have been characterized using XRD and chemical analyses. ZrB_2 powder contained 78.8 wt. % B, 0.7 wt. % C and < 0.1 wt. % O, corresponding to $ZrB_{1.95}$ + 3.5 % B_4C. Except for the impurities indicated in Table 2.1, the SiC_{M5} powders contained Fe in an amount up to 0.5 wt. %.

The study of SiC-ZrB_2-B_4C system was carried out with SiC powder from the Starck Company (Germany) and ZrB_2 powders produced at the IPMS. To activate sintering, boron carbide (HS grade, N.C. Starck Germany) was introduced in an amount of 5 - 12 wt.%.

Table 2.1. Characteristics of powders.

Powder	Particle size, d_{50}, μm	Oxygen content, wt.%	Free carbon, wt. %
SiC_{M5}	5	1.5	1 - 2
SiC_{UF05}	1.47	0.55	-
SiC_{UF10}	0.7	1.2	0.17

SiC powders were very different in their defectiveness and in sintering capacity. The powders UF05 and M5 were characterized with low width of X-ray diffraction peaks and good resolution of K_α-doublets at high reflection angles ($2\theta > 100°$) and, therefore, had a high degree of structural perfection (Fig. 2.1.). At the same time, the XRD peaks of UF10 were very broad due to high density of defects (stacking faults, polytypes interlayer, and non-homogeneous microstrains, in accordance with TEM data), which, apparently, facilitated an increase in their activity during sintering.

a)

b)
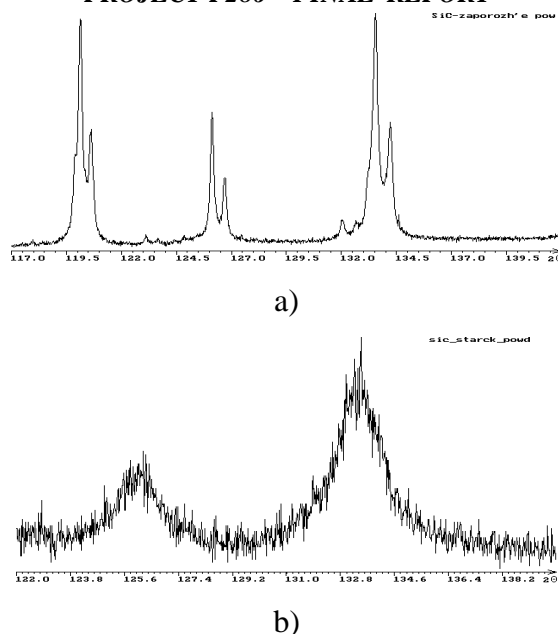
Fig.2.1. XRD curves for large-grain SiC_{M5} powders (a) and SiC_{UF10} powder (b).

The results of XRD analysis are given in Fig 2.2-2.4. For all the cases, the powders were practically monophase ones, possibly, the additives of corresponding metals in silicide powders were present in insignificant amounts.

For achievement of maximal authenticity of the subsequent work a special rigging was made for preparation of charge which includes grinding of components and additives. The grinding of powders and charges is carried out during 3-9 hours in the planetary mill in the acetone medium using the ZrB_2 grinding balls. Grinding balls were made of pure powders by hot pressing. The absence of additives – sintering activators – resulted in residual porosity and low density of ball material as well as transfer of the ball material to the charge. This was taken into account in the charge composition. The drums of planetary mill were fabricated out of caprolactone wear-resistant polymer.

PDF-No	In Range	Matched	FOM	SOM	Name Min.	Formula
34- 423	4	4	0.316	1.250	Boron Zirconium	ZrB_2
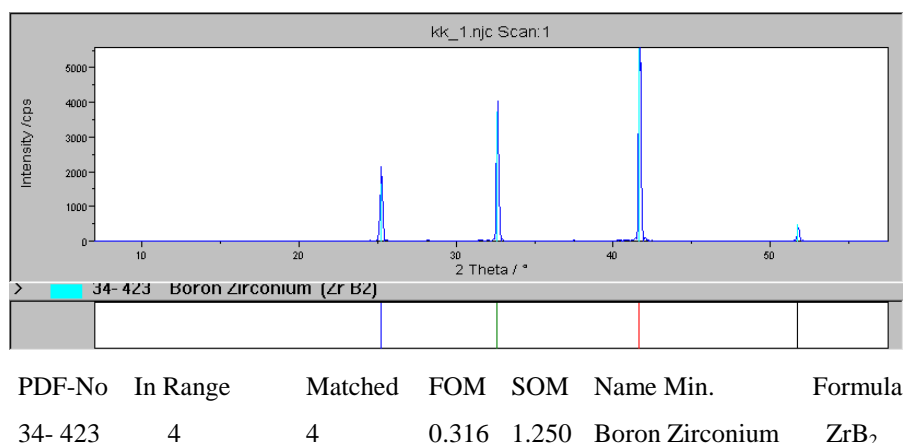
Fig.2.2. The fragment of XRD pattern for ZrB_2 powder.
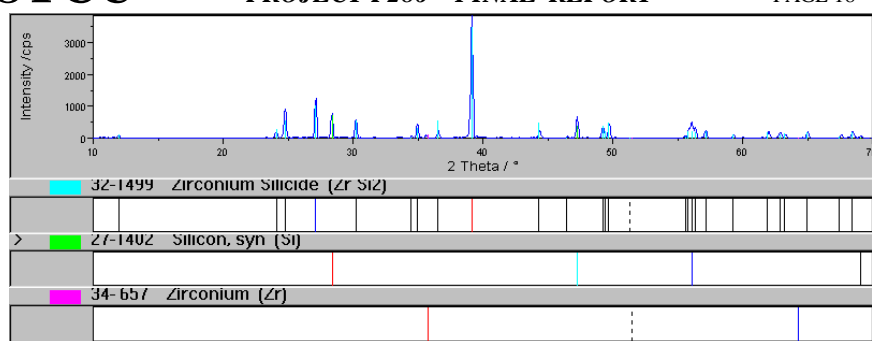
PDF-No	In Range	Matched	FOM	SOM	Name Min.	Formula
27-1402	4	4	0.130	3.162	Silicon, syn	Si-etalon
32-1499	27	26	0.627	1.316	Zirconium silicide	$ZrSi_2$

Fig.2.3. The fragment of XRD pattern for $ZrSi_2$ powder.
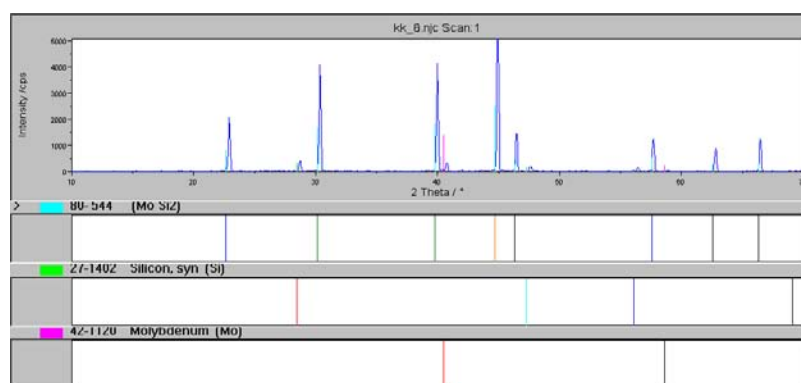
PDF-No	In Range	Matched	FOM	SOM	Name Min.	Formula
80- 544	8	8	1.857	2.028		$MoSi_2$
27-1402	4	4	2.471	2.550	Silicon, syn	Si-etalon

Fig.2.4. The fragment of XRD pattern for molybdenum silicide.

In the experiments concerning the effect of boron carbide additives on hot pressing and high-temperature properties of composites of SiC-ZrB_2-B_4C system, the charges were prepared in the mills lined with boron carbide using boron carbide and silicon grinding balls. Grinding was carried out to the particle size ~3 μm. Grinding kinetics for the SiC-ZrB_2 charge is shown in Table 2. 2.

Table 2.2. The grinding kinetics for SiC-ZrB_2 charge.

Charge particle size, μm	Grinding time, hours			
	3	5	7	9
Average size, μm	2.9	2.5	1.9	1.7
Maximum size, μm	12	8	6	4

The grinding time of 9 h ensuring the optimum dispersion and good mixture of powder was found to be the optimum one despite the fact thatparticle sizes after 5 h grinding were acceptable for hot pressing. The optimum time of grinding was chosen individually.

The size of the charge particles was determined by sedimentation with a Laser Micron Sizer.

2.2. Hot pressing.

Hot pressing was carried out using the SPD120 installation with induction heating at the Institute for Problems of Materials Science on the base of P-125 press installation in graphite dies without protective atmosphere. The temperature of isothermal exposure was in the range of 1600-2150 °C under pressure of 26-30 MPa, exposure time – 20 min, the rate of heating and cooling – up to 100 ^{o}/min. A graphite accessory for hot pressing of powders has been specially fabricated.

The samples for the study of mechanical properties had size of 5x5x45 mm and 50x50x10 mm (plates); they were fabricated in multiplace dies. After isothermal exposure axial pressure was withdrawn, samples were cooled in moulds with the rate of 35 ^{o}/min down to T=1200-1500 °C. Then the ceramics together with mould were placed into graphite container for final cooling down to room temperature. During hot pressing equipment indications were recorded, and shrinkage kinetics was calculated.

It is necessary to point out the peculiarities of hot pressing process. Unlike the vacuum hot pressing, ceramics sintering without protective medium is carried out under the condition of CO-CO_2 partially reducing atmosphere as a result of the use of graphite rigging. Because of this a series of chemical interactions may take place with the participation of residual charge oxide phases, as well as CO and CO_2. The features of these processes were not sufficiently studied. However, experimental data (at our disposal) show that under sintering the refining of ceramics with the formation of ZrB_2 secondary phase takes place as well as significant evolution of gases, namely, SiO, B_2O_3, CO_2, etc. That is why the optimization of hot pressing regimes plays an important role as well as ensuring of gas evolution, the latter being achieved with isothermal exposures at intermediate temperatures and due to the use of maximum pressures at the last process stages. As a result, it enables us to manufacture ceramics parts, for example, plates with the sizes of 90x90x10 mm^3 with uniform structural and physical-mechanical characteristics (with variation of 5-10%).

2.3. Experiments on sintering of selected compositions.

ZrB$_2$-ZrSi$_2$-SiC system.

The compositions and regimes of ceramics samples fabrication for ZrB$_2$-SiC and ZrB$_2$-ZrSi$_2$-SiC systems are given in Tables 2.3 and 2.4. In the tables the values of bending strength and sample porosity are presented as well.

Table 2.3. Composition of ZrB$_2$-SiC ceramics system and regimes of their hot pressing.

#	Samples	Charge composition, vol.%		Hot pressing regimes			Bending strength, MPa	Porosity, %
		SiC	ZrB$_2$	τ of isothermal duration, min	T of isothermal duration, ^{o}C	P, MPa		
1	US1	-	100	15	2175	30	325	10
2	US2	17	83	15	2175	30	490	0
3	US3	23	77	15	2150	30	465	0
4	US4	50	50	15	2125	30	365	5.8
5	US6	65	35	15	2125	30	270	14

Table 2.4. Composition of ZrB$_2$-ZrSi$_2$-SiC ceramics system and regimes of their hot pressing.

#	Samples	Charge composition, vol.%			Hot pressing regimes			Bending strength, MPa	Porosity, %
		SiC	ZrB$_2$*	ZrSi$_2$*	τ of isothermal duration, min	T of isothermal duration, ^{o}C	P, MPa		
1	USS1	-	93.5	6.5	15	2125	30	370	11
2	USS3	26	67	7	10	2125	30	223	3.5
3	USS4	50	46	4	15	2125	30	450	0
4	USS6	60	37	3	20	2125	30	380	5.7
5	USS6	60	37	3	30	2125	30	270	11.5
6	USS6	60	37	3	45	2125	30	260	13

*The ratio of ZrB$_2$: ZrSi$_2$ in a charge was equal to 92 : 8. The deviation of composition from this ratio was caused by the admixture of ZrB$_2$ ball material during grinding.

We also studied the peculiarities of mechanical behavior of ZrB_2-SiC-$ZrSi_2$ triple ceramics, which were the variation of USS4 ceramics. Thus, 6 compositions of ceramics mentioned above were fabricated, and 8 samples of every composition were manufactured (Tabl. 2.5). The porosity of the samples obtained was $< 2\%$.

Table 2.5. The composition of charges for the samples of ZrB_2-$ZrSi_2$-SiC system

	Phase content [wt%]			Sintered at [°C]
	SiC	ZrB_2	$ZrSi_2$	
USS41	33.2	64.7	2.1	2125
USS42	33.5	62.8	3.7	2125
USS43	33.6	58.8	7.6	2125
USS44	33.9	55.8	10.4	2125
USS45	34.1	52.7	13.1	2125
USS46	34.4	49.0	16.6	2125

The ZrB_2 : $ZrSi_2$ ratio of these samples was varied in the ranges given in the Table 2.6 below:

Table 2.6. The ZrB_2 : $ZrSi_2$ ratio for ceramic composites

Marking index	USS-41	USS-42	USS-43	USS-44	USS-45	USS-46
ZrB_2 vol.%	96	93	86	81	76	73
$ZrSi_2$ vol.%	4	7	14	19	24	27

The strength testing at high temperatures have been also fulfilled for the sample series of the following composition:

USS-32 - 75 vol. % (97 vol. % ZrB_2+3 vol. % $ZrSi_2$) +25 vol. % SiC

USS-43 - 52 vol. % (84.5vol. % ZrB_2+15.5 vol. % $ZrSi_2$) +48 vol. % SiC

USS-72 - 33vol. % (88 vol. % ZrB_2+12vol. % $ZrSi_2$) +66.7 vol. % SiC

Taking into account the preliminary results of high-temperature strength and oxidation tests, the US-20 composition based ceramics were chosen for the further studies.

The compositions were varied in the ranges given in the Table 2.7 below:

Table 2.7. The charge composition of ceramics investigated.

Marking index	US-20	USS-22	USS-23
ZrB_2 vol.%	81.4	78	75.4
SiC vol. %	18.6	17.8	17.2
$ZrSi_2$ vol.%		4.2	7.4

For all the samples the ZrB_2 /SiC volume ratio was equal to 4.4/1. For the grinding the ZrB_2 balls were fabricated, and the additional inclusion of ZrB_2 in a charge was taken into account in calculation of material composition formula. For the manufacturing of samples the hot pressing method was used, the process temperature was 2100 °C, the isothermal exposure was 10 min. The porosity of the samples obtained was < 2 %.

It is well known that the ceramics composition before the hot pressing should be refined in order to remove undesirable oxide impurity phases. Taking into account the results obtained we have done the additional attempt to clean the ceramics at the hot pressing, in order to eliminate undesirable oxide phases (additives). In order to eliminate the amorphous oxide phases with the aid of carbo- (carbide) thermal reduction we incorporated into ceramics composition carbon-containing additives , in particular, B_4C. Besides, TaB_2 and YB_2 additives have been introduced into the composition of ceramics, the latter with the intent to improve the high-temperature characteristics of USS-22 system composites. The main characteristics of these ceramics are presented in Table 2.8.

Table 2.8. Physical-mechanical characteristics of composites of USS-22 system.

Samples	Density, g/cm^3	Porosity, %	Bending strength, MPa	Deviation, MPa
USS-22	5.6	< 2	478.7	24.4
USS22T (USS-22+ 2 vol.% TaB_2)	5.48	3	435.0	15.4
USS22Y (USS-22+ 2 vol.% YB_6)	4.99	9	381.5	58.5
USS22B (USS-22+ 2 vol.% B_4C)	5.00	7	376.6	33.6

One can see in Table 2.8 that practically all the samples obtained have considerable residual porosity and as a result somewhat lesser strength characteristics.

The results of XRD analysis are presented in Fig. 3.29, 3.30 and 3.31.

USS-22+ 2 vol.% TaB$_2$
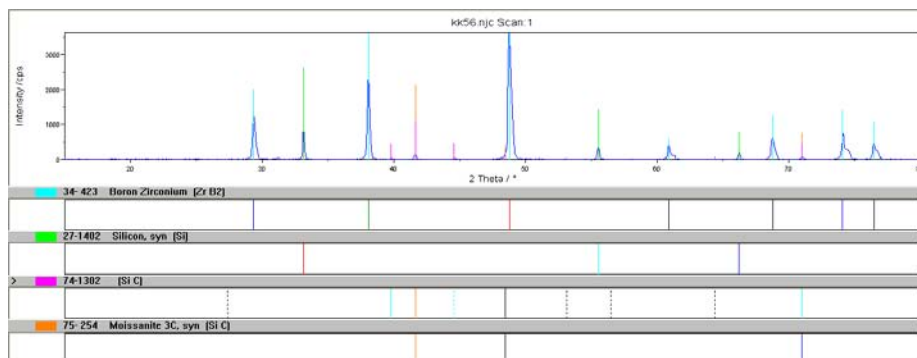
PDF-No	In Range	Matched	FOM	SOM	Name Min.	Formula
34- 423	7	7	0.091	1.690	Boron Zirconium	ZrB$_2$
27-1402	3	3	0.177	2.582	Silicon, syn	Si
75- 254	3	3	0.540	2.582	Moissanite 3C, syn	SiC
74-1302	9	4	0.643	4.000		SiC

Fig. 2.5. XRD pattern for USS-22+ 2 vol.% TaB$_2$ hot-pressed samples.

One can see in XRD pattern for USS-22T ceramics the lines of Si standard sample, α-SiC, β-SiC and ZrB$_2$. The ZrB$_2$ lines at large angles have the second component (solid solution or other boride with the lattice parameters less than for zirconium boride).

One can see in XRD pattern for USS-22+ 2 vol.% YB$_6$ ceramics (Fig. 2.6) also the lines of Si standard sample, α-SiC, β-SiC and ZrB$_2$; probably, the lines of yttrium silicide are present as well.

In the XRD pattern for USS-22+ 2 vol.% B$_4$C ceramics (Fig. 2.7) the lines of Si standard sample, α-SiC, β-SiC and also ZrB$_2$ (without other component) as well as the line of (002) graphite are present.
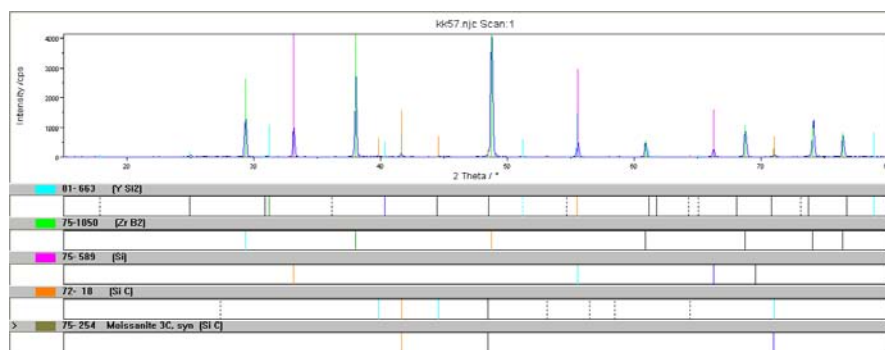
PDF-No	In Range	Matched	FOM	SOM	Name Min.	Formula
75- 589	4	4	0.092	2.828		Si
75-1050	7	7	0.115	2.138		ZrB$_2$
72- 18	10	6	0.458	3.360		SiC
75- 254	3	3	0.647	3.266	Moissanite 3C, syn	SiC
81- 663	21	14	2.494	1.695		YSi$_2$

Fig. 2.6. XRD pattern for USS-22+ 2 vol.% YB$_6$ hot-pressed samples.
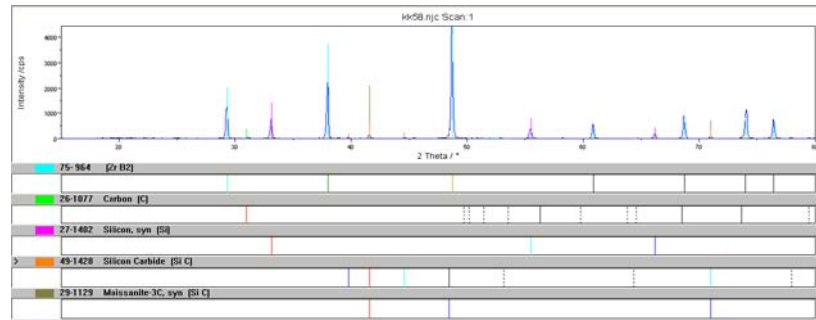
PDF-No	In Range	Matched	FOM	SOM	Name Min.	Formula
75- 964	7	7	0.457	1.813		ZrB_2
29-1129	3	3	0.512	2.769	Moissanite-3C, syn	SiC
27-1402	3	3	0.590	2.769	Silicon, syn	Si
49-1428	8	5	0.701	3.432	Silicon Carbide	SiC
26-1077	12	4	1.085	3.916	Carbon	C

Fig. 2.7. XRD pattern for USS-22+ 2 vol.% B_4C hot-pressed samples.

As the obtained results confirmed, the introduction of additives has led to the reduction of ceramics strength (Table 2.8). In the case of USS-22B it may be connected with the residual carbon which was not entirely used for the reduction of initial charge oxides in the process of hot pressing. Results may be also caused by high residual porosity of the samples (Table 2.8).

Samples of ceramics of ZrB_2-$MoSi_2$ system.

The charges of five compositions for the samples of ZrB_2-$MoSi_2$ system were prepared. (Table 2.9).

Table 2.9. The composition of charges for the samples of ZrB_2-$MoSi_2$ systems.

Type of samples	ZrB_2, wt.%	$MoSi_2$, wt. %
M2	93	7
M3	86	14
M4	80	20
M5	56	44
MP5	63	37

Hot pressing of samples was carried out under the pressure of 30 MPa during isothermal exposure in the temperature range of 1775–1800 °C. The MP5 charge was used for the obtaining of samples at the temperatures of 1750, 1830 and 1900 °C.

SiC-ZrB$_2$-B$_4$C system

Hot pressing modes applied to SiC - ZrB$_2$ **-** B$_4$C system were analogous to the ones used for SiC - ZrB$_2$ ceramics fabrication. However, an optimization of hot pressing temperature was carried out.

Temperature of eutectic melting for SiC - ZrB$_2$ - B$_4$C triple system equals to 2150 °C and hot pressing at this temperature was accompanied by a partial melting of compositions. The optimum temperature of hot pressing (1950 – 2050 °C) in the system depends on the material composition and for each composition lies in a rather narrow range ($\pm$ 20 °C); the deviation from the optimum temperature is followed by either porosity or grain size growth with a sharp decrease of strength. The adjusted hot pressing regimes ensured manufacturing of ceramicswith porosity in the range of 1-3%.

The manufacturing conditions and strength of HP-composites are given in Table 2.10.

Table 2.10. Compositions and conditions of charge preparation for SiC - ZrB$_2$ - B$_4$C ceramics

Charge composition, vol.% (calculated, accounting for boron carbide milling contributed by grinding balls)	Milling conditions in acetone media	Properties of HP samples 4-point bending strength (stdev), MPa
SiC$_{UF05}$ + 6%B$_4$C	9h, SiC balls	321(17)
SiC$_{UF10}$ + 8%B$_4$C	6 h, B$_4$C balls	318(40)
SiC$_{UF10}$+10%ZrB$_2$	3h, SiC balls	246(46)
SiC$_{UF05}$+22%ZrB$_2$	3h, SiC balls	290(54)
SiC$_{UF10}$+10%ZrB$_2$ + 8%B$_4$C	3 h, B$_4$C balls	400(32)
SiC$_{UF10}$+13%ZrB$_2$ + 8%B$_4$C	7h, B$_4$C balls	391(38)
SiC$_{UF10}$+21%ZrB$_2$ + 8%B$_4$C	7h, B$_4$C balls	403(74)
SiC$_{UF05}$+35%ZrB$_2$ + 10%B$_4$C	9h, B$_4$C balls	532(60)
SiC$_{UF05}$+47%ZrB$_2$ + 10%B$_4$C	9h, B$_4$C balls	576(64)

2.4. Samples Characterization

Grinding using diamond wheels with a grain size of 125/100 and 80/63 μm was carried out after hot pressing.

Complex (XRD and microscopy) investigation of structural state of the obtained composites

Ceramics phase composition was determined by XRD method. The investigations were performed using HZG-4 and DRON-3M devices with filtered radiation of Fe and Cu anodes using discontinuous diagram registration mode in the angle range $2\theta = 20 - 155^0$ to provide qualitative phase analysis and diffraction line intensity measurements, as well as in point-by-point scanning mode for precise determination of crystal lattice parameters in the range of higher reflection angles and diffraction line width analysis. Measurements were fulfilled by θ -2θ scheme with Bragg-Brentano focusing. To decrease background signal, selective absorbing Mn-filters for Fe-radiation and Ni-filter for Cu-radiation were used. The initial treatment of XRD data (separation of background, deduction of $K_{\alpha2}$ component, determination of place and shape peak parameters) as well as qualitative phase analysis was performed using the New-profile and Rayflex program packages.

The microstructure of ceramics was investigated by optical (BH-2, Olympus) and scanning electron microscopy (LEO 1550 SEM). The fluctuation factor for MeB_2 content (ratio of standard deviation to the average) was introduced as a characteristic of heterogeneous distribution of second phase in ceramics with subsequent plotting of dependencies of the fluctuation factor vs. region size, by which the averaging was established. With this purpose, MeB_2 contents in the regions of different S size were determined on micrographs by the point quantitative analysis. Minimum area size was comparable to the distance between particles (12 μm) with 48-57 analyzed fields for various samples; maximum area size was equal to 85 μm with 6-8 analyzed fields.

The investigation of initial samples and different oxide layers of the scale formed has been carried out by Auger-electron spectroscopy (AES) with gradual etching of oxide film layers under Ar^+-ions bombardment using Auger spectrometer LAS-2000, Riber, France. The relative content of metal, silicon, and oxygen atoms was determined from Auger-peak intensity in AES-spectra of the oxide coating nanolayers. The element composition of samples before and after their oxidation during different oxidation stages has been also determined using the method of energy-dispersion X-ray spectral analysis with the aid of Oxford Link microprobe for a scanning electron microscope. The pictures of non-oxidized and oxidized sample surfaces for different temperatures and appropriate oxidation stages have been obtained using SEM method.

Investigations of strength properties in a wide temperature range.

Bending strength of the samples 4 –12 pieces per point was measured by three and four-point bending on the spans of 30 mm and 20x40 mm. For a high-temperature measurement of ceramics strength in air at three- and four-point bending, a special accessory out of hot-pressed silicon nitride was fabricated. The maximum testing temperature was 1400 °C. Special heating unit for samples heating (Fig. 2.8) was fabricated to work together with NIKIMP-1246 testing machine (Russia) equipped by special furnace.
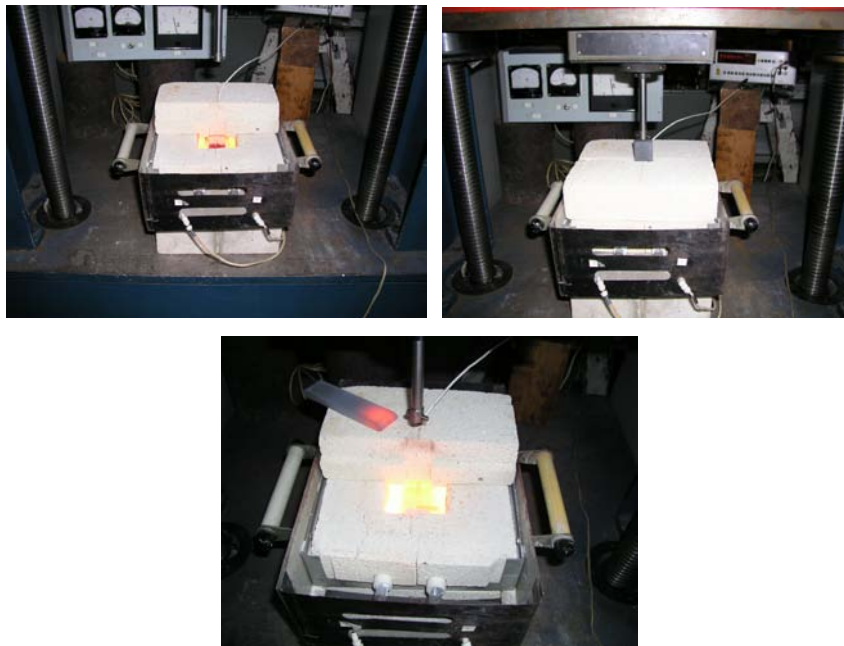
Fig. 2.8. High-temperature attachment mounted at the installation for mechanical testing of ceramics in oxidizing medium.

An indentation model and characteristics of contact strength

In this study, for the certification of the materials obtained we used indentation methods enabling to determine not only hardness but also characteristics of contact strength at tension and compression as well as fracture toughness. A new model of indentation of brittle heterophase materials was developed in which macrohardness is considered as a characteristic of resistance of materials to fracture and consequently it, naturally, depends on both strength at one-axis compression Y, and on strength at one-axis tension σ_f[25].

The model assumes that three zones are formed in the neighborhood of impression (see Fig. 2.9): $r > c$ – elastic zone (1); $a \leq r \leq c$ — zone of a material fractured by radial cracks of normal opening (2); $r < a$ – core (3) from compressed fractured material which has initially belonged to zone (2). The obtained formulas establish dependence between hardness HM and material parameters Y, σ_f, E, ν and make possible evaluation of material strength at one-axis compression Y by experimentally measured hardness HM.

The special feature of the model is that the hardness and strength at one axis compression are connected by a ratio similar to Taybor's ratio

$$HM = CY, \tag{2.1}$$

where value C (which, generally speaking, is a function of HM, σ_f, ν, E) for brittle materials can be bigger than 3, with interval of typical values 4-10. Y further is referred to as contact strength at compression of indented material.
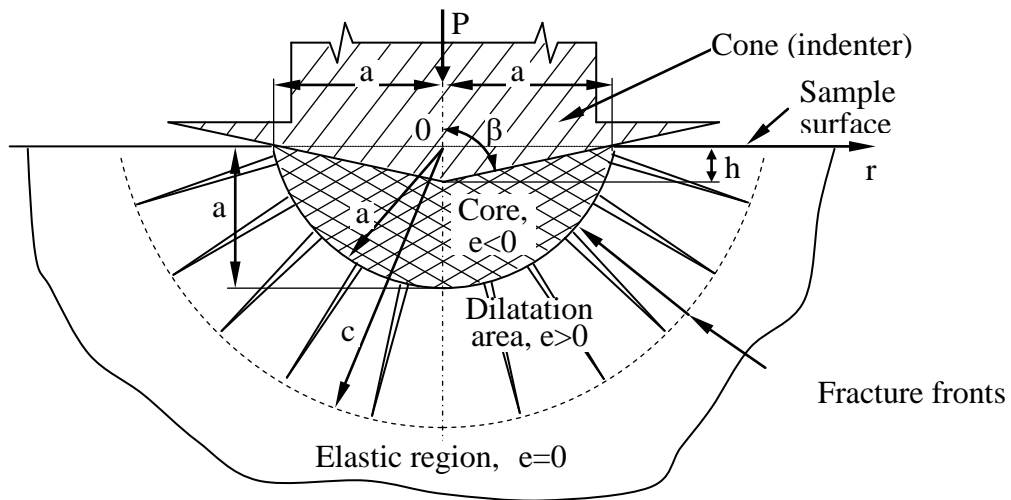
$r > c$ – elastic area (volumetric deformation $e = 0$); $a \leq r \leq c$ - area of dilatation and pores formation (volumetric deformation $e > 0$); $r < a$ – core (volumetric deformation $e < 0$).

Fig. 2.9. Scheme of a model in spherical coordinates $0r\theta\varphi$.

On the basis of these assumptions the following formulas for the definition of Y for a material with initial porosity θ_0 were obtained:

$$HM = CY, \quad C = \frac{2(1-\theta_c)^{3/2}}{3\sqrt{\theta_c}}, \quad \theta_c = 1 - \exp(-e_c), \tag{2.2}$$

$$e_c = \frac{HM}{E}\left[1-(1-\nu)\sqrt{\frac{2\sigma_f}{HM}}\right],$$

$$e_k = -\frac{\cot\beta}{2} + \frac{3}{2}\frac{HM}{E}\left(2-(1-\nu)\sqrt{\frac{2\sigma_f}{HM}}\right) + \frac{8\left(1-\nu_i^2\right)HM}{\pi E_i},$$

$$\theta_k = \frac{e_k - e_{ks} + \theta^*}{1+e_k}, \quad e_{ks} = -\frac{3HM(1-2\nu)}{E}, \quad \theta^* \approx \theta_0 + \theta_c$$

where θ_c is the porosity of material at r = a+0, θ_k is the average porosity in the core, e_k is the average volumetric deformation in the core, e_c is the volumetric deformation at r = a+0, e_{ks} is the average volumetric deformation of a solid phase of core, E_i, ν_i are the elastic constants of the indenter.

The average hydrostatic pressure p and average intensity of shearing stresses τ in the core are defined by formulas:

$$p = -HM\cdot(1-\theta_k), \quad \tau = HM\cdot\theta_k\sqrt{\frac{3}{2}}$$

Formulas (2.2) are obtained for porosity functions:

$$\varphi = (1-\theta)^2, \quad \psi = \frac{2}{3}\frac{(1-\theta)^3}{\theta}.$$

We should note that in this model the sizes of zone 2 and 3 (see Fig. 2.9) are related by the ratio

$$\frac{a}{c} = \sqrt{\frac{2\sigma_f}{HM}} \leq 1,$$

thus, zone 2 is absent in materials, for which $2\sigma_f > HM$. For these materials, as it follows from formulas (2.2), $e_c > 0$ and $\theta_c > 0$ ($\theta_c \neq 0$). Therefore the considered model is meaningful only for materials, for which $2\sigma_f \leq HM$, i.e. for materials in which radial cracks are formed at indentation tests. In formulas (2.2) porosity θ_c can not be considered as independent parameter. In fact if θ_c is independent then from formula $HM = CY$ follows, that $HM \to \infty$ at $\theta_c \to 0$, similarly, to hydrostatic pressure in models of compactable porous body where the principle of inaccessibility of pore-free state is realized.

Thus, the relationship of contact strength and hardness is defined by the relation similar to Taybor's relation for hardness and yield stress in ductile materials. However, we defined value Y as strength at one-axis compression of brittle material when this material undergoes multiple

fracturing (due to shearing stresses) on the boundary between the core r = a and cracked material, followed by compaction from porosity on the core boundary θ_c to average porosity in the core θ_k.

Contact strength at tension σ_f

Dependence (1) is not enough to define Y and σ_f by known values HM, ν, E. The authors suggested a statistical model of formation of radial cracks on sample surface in the vicinity of indenter indentation which uses Weibull's hypothesis of "weak link" and establishes parameters of appropriate distribution which defines strength at tension σ_f and homogeneity m of the material. Thus, the model provides a theoretical background for the method of definition of important mechanical properties of brittle materials (strength at tension σ_f, strength at compression Y, and fracture toughness K_{1c}) by experimental measurement of their hardness and lengths of radial cracks on sample surface in the vicinity of hardness indentation.

Hemispherical zone with fragmented core ("non-elasticity" zone) formed at indentation is the cause of tensile near-surface stresses which decrease as the distance from the indenter increases. Fig.2.10 illustrates a scheme of static penetration of indenter in ceramics, near-surface radial cracks in the vicinity of indentation and distribution of tensile stresses in the layer e ≈ a/10 (a – radius of indentation).

Contact strength at tension σ_f is defined as a value of tensile stresses at a point of arrest of radial crack r = c:

$$\sigma_f = \sigma_\theta (r = c),\tag{2.3}$$

where c – average length of a crack, starting from the center of indentation and σ_θ - near-surface tensile stress outside of indentation which is defined as:

$$\sigma_\theta (r) = \frac{HM}{\sqrt{3}} \left(\frac{a}{r} \right)^2, \quad r > a \quad ,\tag{2.4}$$

where HM – Meyer's hardness.

Thus, in lieu of usually used static strength limit at tension σ_f under conditions of one-axis loading we entered a new characteristic – contact strength of ceramics at tension for which further we will use the same designation σ_f, as earlier.

The statistical analysis of processes of formation of radial cracks we carried out using the hypothesis of Weibull's "weak link" according to which the probability of fracture under tensile stress which is less than σ, can be determined by means of function of distribution:

$$F(\sigma) = \begin{cases} 1 - \exp\left(-\left(\dfrac{\sigma}{b}\right)^{m-1}\right), & \sigma \geq 0 \\ 0, & \sigma < 0 \end{cases} \quad , \text{ where } b = \left[\dfrac{\sqrt{3}e^2(m-1)\sigma_0^m}{\pi HMa^2}\right]^{1/(m-1)} \tag{2.5}$$
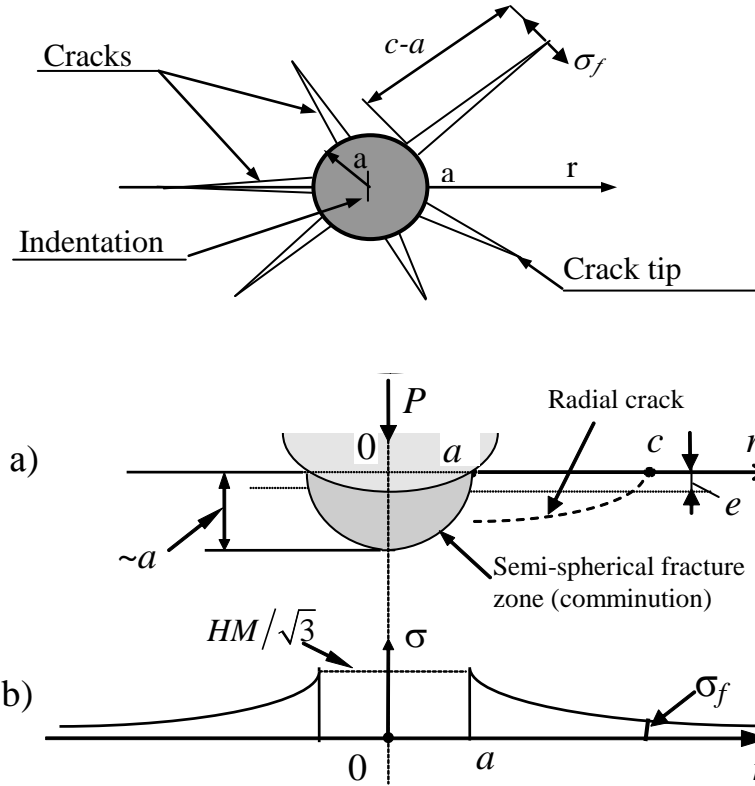
a) scheme of loading of sample by spherical indenter – top view and cross section (a – radius of contact area, c – length of a radial crack which is measured from indentation's center, e ≈ a/10 – depth of near-surface layer, P – loading on indenter);

b) distribution of tensile stresses outside indentation (HM – Meyer's hardness, σ_f – contact strength at tension)

Fig. 2.10. Scheme of static penetration of spherical indenter in brittle bodies.

Parameters of statistical distribution m, σ_{in} can be obtained, for example, by graphic method from graphs usually used in this case for data sets of contact strength in coordinates lnln (1-F)–1-lnσ. The validity of the assumption on adequacy of the proposed distribution of contact strength by formula (2.5) is tested by closeness of the observable strength to theoretical linear dependence.

Microstructural strength

For brittle materials typical are significant differences between values of strength at compression and tension. An opportunity of determination of contact strength of brittle materials at compression and tension in indentation experiments stipulated the investigation of nature of these differences. According to[26] fracture is considered as a process of damage accumulation of (microcracks) which is possible when stresses of the second kind (σ_{II}) in microvolumes of material are tensile and greater than some critical value S (average resistance of particles of microstructure to brittle fracture). Assuming that: 1) stresses of the second kind are distributed by the law which is approximated by normal distribution, and 2) dispersion of distribution of stresses of the second kind is proportional to volumetric density of energy of elastic deformations of the first kind, the authors[26] obtained a relation which defines parameter S through value σ_f and Y:

$$S = \frac{Y \cdot \sigma_f}{Y - \sigma_f} \tag{2.6}$$

The increase of parameter S at close values σ_f and Y (low ratio Y/σ_f) corresponds to an increase of strength of microstructural elements (grains or their boundaries) and decrease of damageability of composite ceramic materials.

Fracture toughness

For the determination of K_{1c} fracture toughness of composite ceramics we used the IF (indentation fracture)-method. For the fracture toughness calculation the Niahara-Haselman relations[27] were used:

$$K_{1c} = 0,035 H \frac{\sqrt{a}}{\phi} \left(\frac{E\phi}{H} \right)^{0,4} \left(\frac{l}{a} \right)^{-0,5}, \quad for \quad 0,25 \leq \frac{c}{a} \leq 2 \tag{2.7}$$

$$K_{1c} = 0,129 H \frac{\sqrt{a}}{\phi} \left(\frac{E\phi}{H} \right)^{0,4} \left(\frac{c}{a} \right)^{-1,5}, \quad for \quad \frac{c}{a} > 2...2,5$$

where a ia the half of indentation diagonal, μm; H is the Vickers hardness , GPa; E is the Young's module, GPa; Φ is the coefficient (H = Φ. σ_m); l is the crack length, measured from the indentation corner, μm; c is the crack length, measured from the centre of indentation, μm.

We established also the analytical connection between σ_f (contact strength) and critical coefficient of tension intensity K_{1c} (fracture toughness):

$$K_{1c} = \frac{2\alpha \sigma_f \sqrt{a}}{\sqrt{2\pi}} \left(\frac{c}{a} \right)^2 (T(L))^{-1}, \tag{2.8}$$

as a result of consideration of radial cracks development using methods of fracture physics.

Here α is the coefficient taking into account the difference of radical crack shape and sample geometry from half-infinite crack, T(L) is a dimensionless parameter which maybe conditionally named as coefficient of tension intensity; the latter being generated by indenter on the crack with the size a, normalized to the K_{1c}, material fracture toughness. The T(L) parameter can be determined by the following equation:

$$T(L) = \left(\frac{\sqrt{L}}{1+L} + \frac{\ln\left(1 + 2L + 2\sqrt{L(1+L)}\right)}{2(1+L)^{3/2}} \right)^{-1} = \frac{2\alpha H M \sqrt{a}}{\sqrt{6\pi} \, K_{1c}}, \tag{2.9}$$

where L = (c-a)/a is the relative crack size.

The T(L) function graphic (Fig. 2.11) enables to analyze the mechanism of initiation and propagation of cracks. Since the radial crack size in fact is determined by equation (2.9), there can be different cases (depending on the value of dimensionless parameter T): 1) equation (2.9) has no solution; 2) equation (2.9) has one solution; equation (2.9) has two solutions.
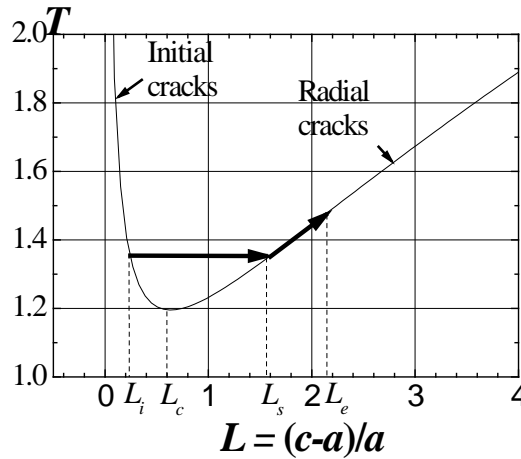
Fig. 2.11. Graphic of T(L) function. L_i is the critical size of unstable initial crack; L_c is the radial crack size which corresponds to T_c= 1.196; L_s is the size of crack which is formed under initial loading; L_b, L_e are the crack sizes in result of load increase.

One can assume that the initial crack, from which radial crack is developed, is directly formed under a load in the field of non-elastic deformations (under indenter) that is presented as the lower graphic branch. Then the first case corresponds to small values of T or small values of a and N when radial cracks are not formed. In the T– L graphic coordinates it means that T curve in the accordance with equation (2.9) and T(L) curve do not intersect (Fig. 2.11). The second case corresponds to T = T_c ≈ 1.196, and, thus, T = T_c and T(L) curve (Fig. 2.11) meet in the point (L_c = 0.6,

$T_c = 1.196$). This intersection may be considered as the condition of first experimentally observed radial crack formation. At the critical contact radius $a_c = 2{,}14\pi K_{1c}^2 / \alpha^2 H M^2$ and critical indenter load $N_c = 4{,}6\pi^3 K_{1c}^4 / \alpha^4 H M^3$ its size is equal to $(c_c - a_c) \approx 0.6a$. At the indenter load $N > N_c$ the values of T increase. The third case is realized when equation (2.7) have two solutions: L_i and L_s (Fig. 2.5). In this case germ crack of critical size L_i ($L_i < L_c$) is unstable and is catstrophically grow up to length L_s. The stable crack development to the L_e length corresponds to the further increase of indenter load.

The (2.8) and (2.9) equation allow to study the β coefficient structure for the known $K_{1c} = \beta N/c^{3/2}$ equation. So, it proves to be that β depends on the relative crack length c/a – γ coefficient as well as their shape and sample geometry – α coefficient:

$$\beta = \alpha\gamma, \quad \gamma = \frac{2}{\pi\sqrt{6\pi}}\left(\frac{\sqrt{1-(a/c)}}{(a/c)} - \frac{1}{2}\ln\left|\frac{\sqrt{1-(a/c)}-1}{\sqrt{1-(a/c)}+1}\right|\right) \tag{2.10}$$

The results of test experiments concerning determination of α, β and γ, carried out for technically important ceramics and hard alloys, showed that the increase of relative crack length c/a corresponds to a systematical decrease of α value (Fig. 2.12). This is connected with a transition of surface radial cracks to the entirely developed half-disk ones. Such transition for the brittle materials, as a rule, takes place in the interval of crack relative length of $2 < c/a < 4$.

Fig. 2.12. Coefficients α, β and γ of TiN–AlN ceramics (a) and of hard alloys (b) in dependence on relative crack length c/a.

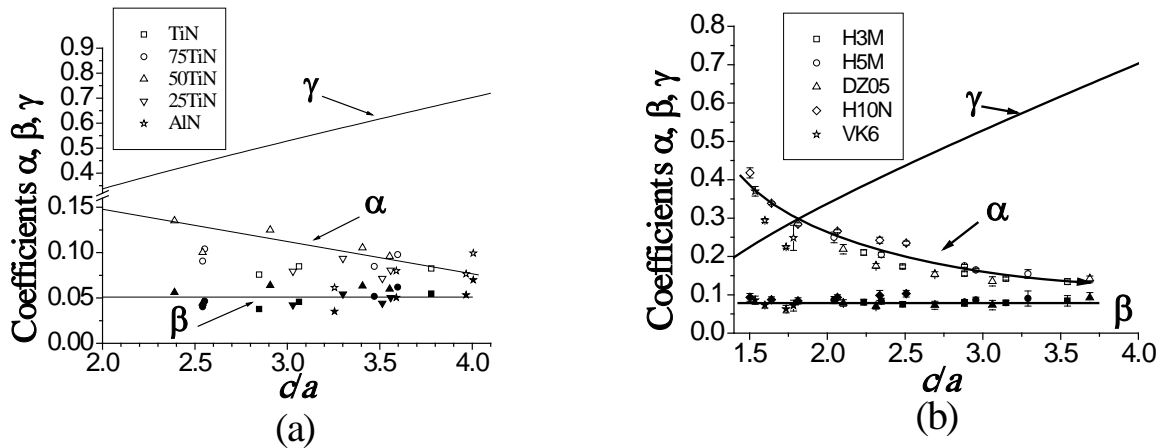## Methods of corrosion testing, investigations of oxidation kinetic characteristics

Works related to the installation and adjusting of laboratory equipment for measuring of TG - and DTA- curves of non-isothermal high temperature oxidation of both samples of individual

components and composite ceramic materials to the maximal temperature 1600 °C have been carried out. At the first stage of the tentative testing of the Hungarian derivatograph "K" the work was conducted obtaining experimental differential thermoanalysis curves (measuring of relative thermal effect of reactions at the different stages of a sample's interaction with oxygen in air) at the atmospheric pressure.

At the same time, laboratory electrochemical setting has been installed and tested, which was used for the preliminary anodic formation of a protective oxide nanofilm on ceramic samples with satisfactory conductivity in order to increase corrosion stability of ceramics for their subsequent high-temperature treatment.

The potential-dynamic polarization curves were obtained using electrochemical setting on the base of PI-50-1 potential-static device. An electrolytic cell consists of ceramic anode, platinum cathode, electrolyte (3% solution of NaCl) and standard silver chloride-silver reference electrode of Ag/AgCl/KCl. The choice of neutral medium of sodium chloride as the electrolyte is explained by the fact that some binary refractory compounds, for example, transition metals disilicides are unstable in the acid environment while NaCl solution, as a rule, is substantially instrumental in the anodic formation of a thin oxide film on the ceramic samples. In the process of formation of preliminary protective nanofilms two regimes of the electrochemical measurements are possible: potential-dynamic one – with a potential sweep rate of 0.5 mV/s, and chronamperometric one - at the fixed potential value.

The oxidation of samples was carried out in the programmed furnace "Bahr" using the following regimes:

1.   Heating with the rate of 10 K/min in the argon medium up to 1400 °C;

2.   Heating with the rate of 2 K/min in the argon medium up to 1500 °C;

3.   Exposure of samples at 1500 °C in the medium of oxygen flux;

4.   Cooling with the rate of 2 K/min in the argon medium down to 1400 °C;

5.   Cooling with the rate of 10 K/min in the argon medium down to room temperature.

Samples were held at 1500 °C in flowing oxygen for 0.5, 3, 15, 30 and 50 h. Before the thermal treatment and after every thermal cycle all the samples were weighed (Sartorius ultra-balance). Thus, the change of sample mass gain was measured gravimetrically during high-temperature oxidation.

The long-term (up to 50 h) high-temperature oxidation (in flowing pure oxygen) experimental set-up is presented in Fig. 2.13 in detail. This set-up allows carrying out oxidation

experiments for different ceramic samples in similar conditions and, using periodic weighing of samples extracted from the furnace, to obtain the corresponding mass gains.

a)   b)
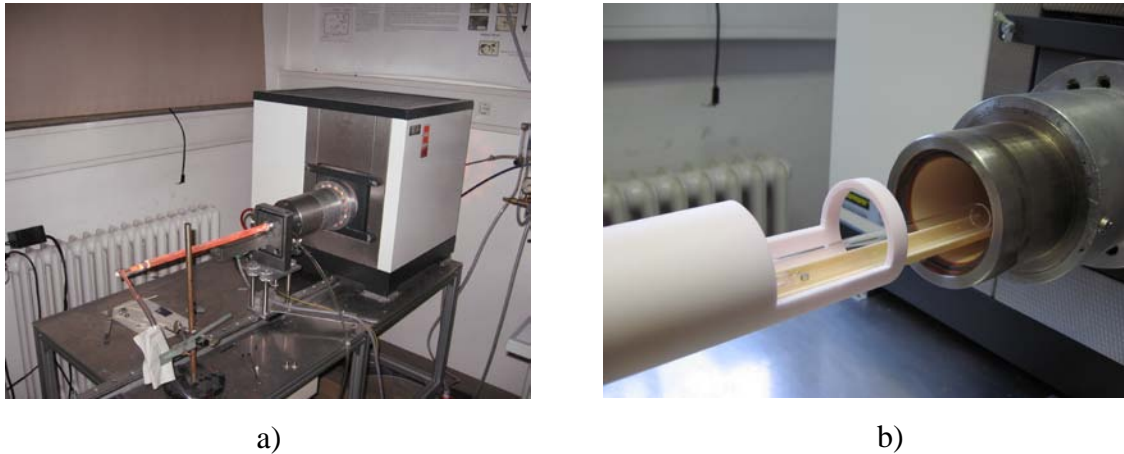
Fig. 2.13. Experimental oxidation tests set-up.

2.4. According to the working plan we have transfered to NASA GRC (Dr. Ali Sayir):

1. Prismatic samples, 4x20x42 mm in size, of three compositions (US20, USS22, USS22-T), 2 samples of each composition, in all - 6 pieces, for determination of thermal expansion coefficient;

2. Prismatic samples, 3x3x20 mm in size of three compositions (US20, USS22, USS22-T), In all - 9 pieces, 3 samples of each composition, for determination of Zeebeck coefficient;

3. Cylindrical samples, D = 12 mm, h = 3 mm of three compositions (US20, USS22, USS22-T), in all - 30 pieces, 10 samples of each composition, for determination of thermal conduction;

4. Prismatic samples, 10x10x40 mm in size of three compositions (US20, USS22, USS22-T), in all - 6 pieces, 2 samples of each composition, for determination of volumetric modulus of elasticity

5. Cylindrical samples, D = 5 mm, h = 1 mm of three compositions (US20, USS22, USS22-T), in all - 12 pieces, 4 samples of each composition, for determination of heat capacity;

6. Cylindrical samples, D = 24 mm, h = 7.85 mm of one compositions (USS22), in all - 6 pieces, 10 samples of each composition, for determination of wear resistance.

The results of samples testing fulfilled up to this time in NASA GRC are presented in Appendix 1.

3. Results and Discussion

3.1. Phase diagrams of Zr-Si-B-C system

The development of new materials is always based on the analysis of state diagrams of appropriate systems.

That is why we present below the literature data concerning the phase diagrams of Zr-Si-B-C system which were studied in papers[28]. The proposed subsolidus compatibility is shown in Fig 3.1.
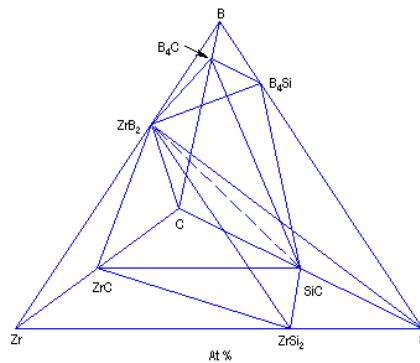
Fig. 3.1. The layout for tetrahedra of state diagram of Zr-Si-B-C system.

The calculated compatibility tetrahedra are such as shown in the following table.

Zr	Si	B	C	ZrC	SiC	B_4C	ZrB_2	$ZrSi_2$	B_4Si
x	-	-	-	x	-	-	x	x	-
-	-	-	x	x	x	-	x	-	-
-	x	-	-	-	x	-	x	-	x
-	-	-	-	-	x	x	x	-	x
-	-	-	x	-	x	x	x	-	-
-	-	x	-	-	-	x	x	-	x
-	-	-	-	x	x	-	x	x	-
-	x	-	-	-	x	-	x	x	-

(x = compatible phase present)

According to these data, the only four-element tie-line is ZrB_2-SiC. However, there are many other phases not included in this diagram, including six certain Zr-Si alloys and the questionable Si-B and B-C phases. The quaternary eutectic temperature is lower than 1360 °C, which is the temperature of the $ZrSi_2$-Si binary eutectic.

Pseudobinary phase diagram of the ZrB_2-SiC system is presented in Fig. 3.2. This system is pseudobinary owing to the peritectic decomposition of SiC at 2760 °C. The system still shows simple eutectic behavior. Constancy of the lattice parameters and microhardness suggest that the degree of mutual solid solubility is very small. The liquidus was extrapolated by the authors from the apparent experimental eutectic to the known melting or decomposition temperatures.
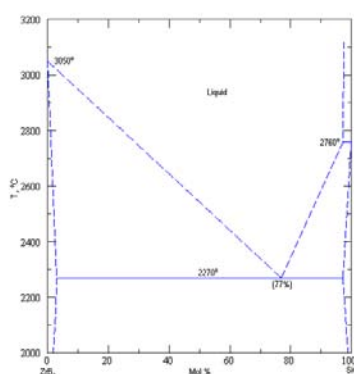
Fig.3.2. Phase diagram of the ZrB_2-SiC system.

3.2. Study of structural state of ceramics samples prepared.

ZrB_2-SiC-$ZrSi_2$ system.

For the ZrB_2– SiC ceramics the hot pressing leads only to some change of silicon carbide polytype composition while the ceramic phase composition does not change compared with the charge (Fig. 3.3). In order to study the interaction of zirconium boride with zirconium silicide we prepared the mixtures with 20 vol. % of silicide, the latter being hot pressed in the temperature range of 1600-2100 °C.

It was established (Fig 3.4 a, b) that in the temperature range pointed out the small amounts of SiC (3C) and ZrO_2 (m) as well as new phase with cubic lattice were formed because of $ZrSi_2$ decomposition and further interaction with composite components and gas sintering media (CO-CO_2). The parameters of new phase of variable composition (changing depending on the sintering regime and ceramics composition) were either close to those of ZrC zirconium carbide or intermediate between the parameters of ZrB and ZrO cubic phases. Thus, one can assume that under hot pressing the formation of ZrC monoboride or solid solution phase (ZrBC - carbo-boride)

took place. This conclusion is confirmed by literature data and the results of SEM and EPMA studies. According to these data, in the composition of such composites are also found, beside the ZrB_2 grains, the grains containing Zr and C or Zr, C and B elements. Hot pressing of HfB_2-SiC composite by Gash et al also resulted in formation of a third phase, which low intensity peaks in X-ray diffraction were attributed to cubic hafnium carbide. However, thorough analysis of the XRD patterns shown in the paper reveals appreciable misfit between the experimental and reference data. The source of carbon for carbide formation should be SiC, which content is mentioned to decrease slightly (2-3 %) after sintering. In our case the essential reduction of lattice parameters of new phase compared with such ones for zirconium carbide may be caused by non-stoichiometry of compound which is formed ($ZrC_{1-x}B_{1-y}$).

Similar secondary phases were found by other authors (Monteverde et al) who probably did not pay due attention to the structure and chemical composition of the phases in question. Usually they are described as cubic solid solution of carbides and nitrides of zirconium and hafnium sometimes stabilized by nitrogen.
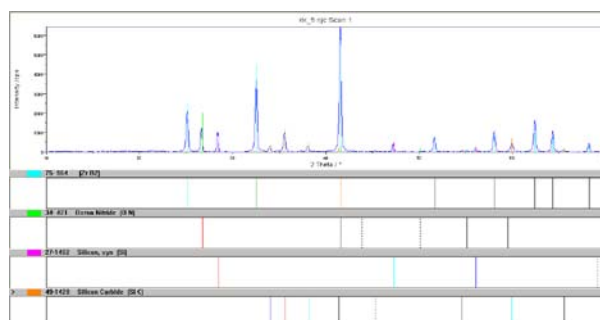
PDF-No	In Range	Matched	FOM	SOM	Name Min.	Formula
49-1428	8	7	0.709	2.366	Silicon Carbide	SiC (6H+3C)
75- 964	8	8	0.772	1.936		ZrB_2
27-1402	4	3	0.777	2.739	Silicon, syn	Si - etalon
34-421	8		0.873	2.179	Boron Nitride	BN*

* Boron nitride as a residuum of luting on the sample surface.

Fig.3.3. XRD pattern for ceramics of ZrB_2 – SiC system manufactured at 2100 °C.

The lattice parameters of ZrB_2, within the limits of experiment errors, remain unchanged, i.e. the formation of solid solutions on the base of ZrB_2 is not observed.

The materials of three-component system were prepared by addition to the powder mixture (92 vol.% ZrB_2 and 8 vol. % $ZrSi_2$) of 0.26; 49.4 and 60.4 vol.% of SiC powder. On the XRD pattern of hot-pressed samples (Fig. 3.5) one can see, beside ZrB_2 and SiC phases, also ZrB zirconium monoboride and, maybe, SiO_2 silicon oxide. The ZrB_2 lattice parameters proved to be also unchanged and, therefore, solid solutions on its base did not form.
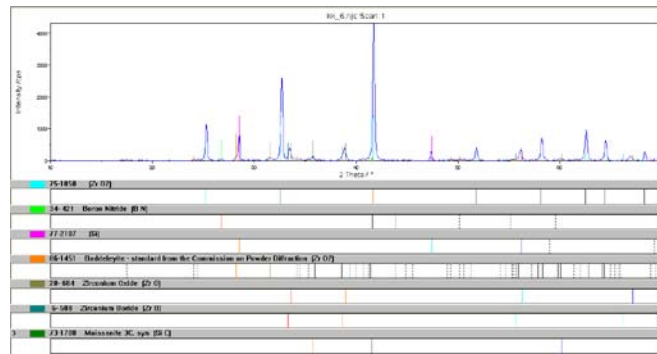
PDF-No	In Range	Matched	FOM	SOM	Name Min.	Formula
77-2107	5	3	0.327	6.161	Etalon	Si
34- 421	6	2	0.409	8.626	Boron Nitride	BN
73-1708	3	3	0.597	4.929	Moissanite 3C, syn	SiC
75-1050	8	8	0.753	2.264		ZrB$_2$
20- 684	4	4	1.024	4.002	Zirconium Oxide	ZrO
6- 508 5	4	4	1.795	4.002	Zirconium Boride	ZrB

a)
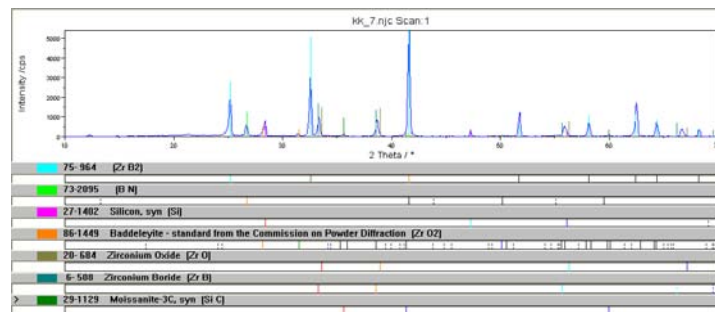
PDF-No	In Range	Matched	FOM	SOM	Name Min.	Formula
75- 964	8	8	0.239	2.449		ZrB$_2$
29-1129	3	3	0.343	5.333	Moissanite-3C, syn	SiC
27-1402	4	3	0.513	3.464	Silicon, syn	Si-etalon
6- 508 5	4	4	1.128	4.330	Zirconium Boride	ZrB
20- 684	4	4	2.404	4.330	Zirconium Oxide	ZrO

b)

Fig. 3.4. XRD pattern of ZrB$_2$ – 20 % ZrSi$_2$ sample manufactured at 1850 (a) and 2100 °C (b).
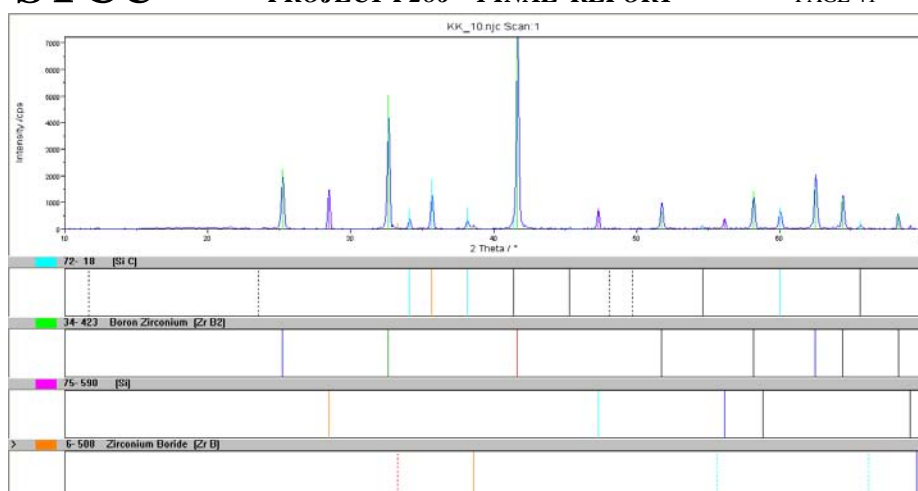
PDF-No	In Range	Matched	FOM	SOM	Name Min.	Formula
34- 423	8	8	0.152	2.345	Boron Zirconium	ZrB_2
75- 590	5	5	0.240	2.966		Si-etalon
72- 18 12	9		0.425	2.937		SiC(6H+3C)
6-508	4	3	4.285	4.146	Zirconium Boride	ZrB

Fig. 3.5. Fragment of XRD pattern for the USS4ceramics of ZrB_2 - $ZrSi_2$ – SiC system.

The microstructures of samples fabricated are presented in Fig. 3.6. As a rule, the darkened regions with maximum density on the optical microphoto pictures correspond to porosity regions. It relates to both total and additional porosity resulting from abrasive treatment, the latter being connected with partial crumbling of one of material phases, mainly, boride. The porosity of US3-USS3-US4-USS4 composites does not exceed 3 %. For the other composites the porosity is essential and achieves a value ~ 10 % that conforms to the data of density measurement.

The improvement of surface state in the case of samples prepared for investigation by SEM method led to a decrease of apparent porosity. In this case the porosity level proved to be close to the porosity inherent to the material itself. In all the cases the grain size of structural components (silicon carbide, zirconium boride and, maybe, ZrB boride phase) of composites studied proved to be in the range of 2 – 20 μm.

a

b

c

d

e

f

g

h
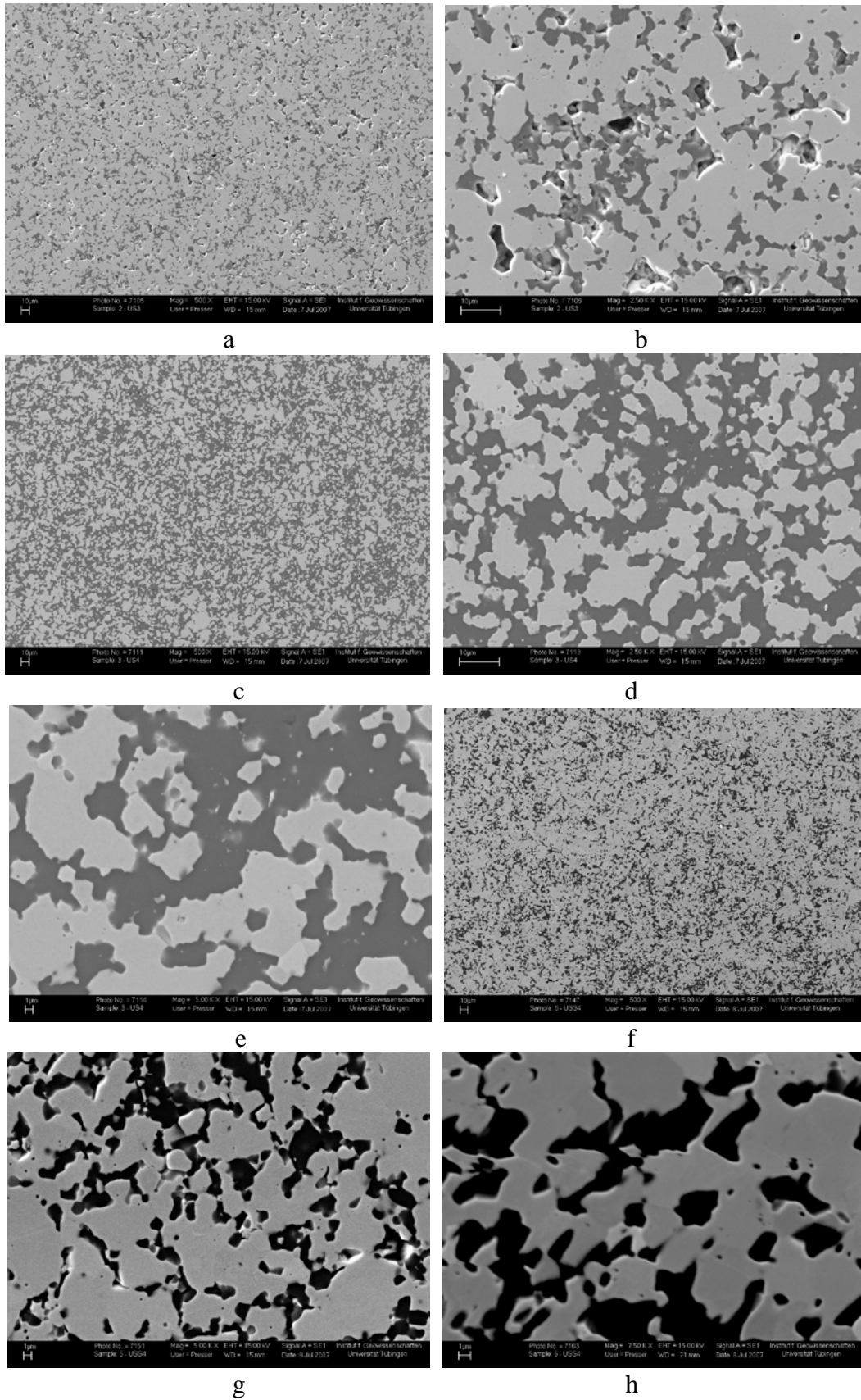
Fig. 3.6. SEM microphotopictures for the ceramics of different composition: US3 - a, b; US4 - c,d,e;USS4 - f,g,h.

The analysis of optical and SEM micropictures showed that for their both types in the field of ZrB_2 grains there are the grains with the coefficient of light diffraction (or electron dissipation) which is near but differs from the such for zirconium diboride (Fig. 3.6h). The EPMA analysis carried out allowed to identify these grains as zirconium ones as well as ZrC and Zr(BC) ones, the latter corresponding to new phases with cubic lattice on the XRD pattern obtained (Fig. 3.7).
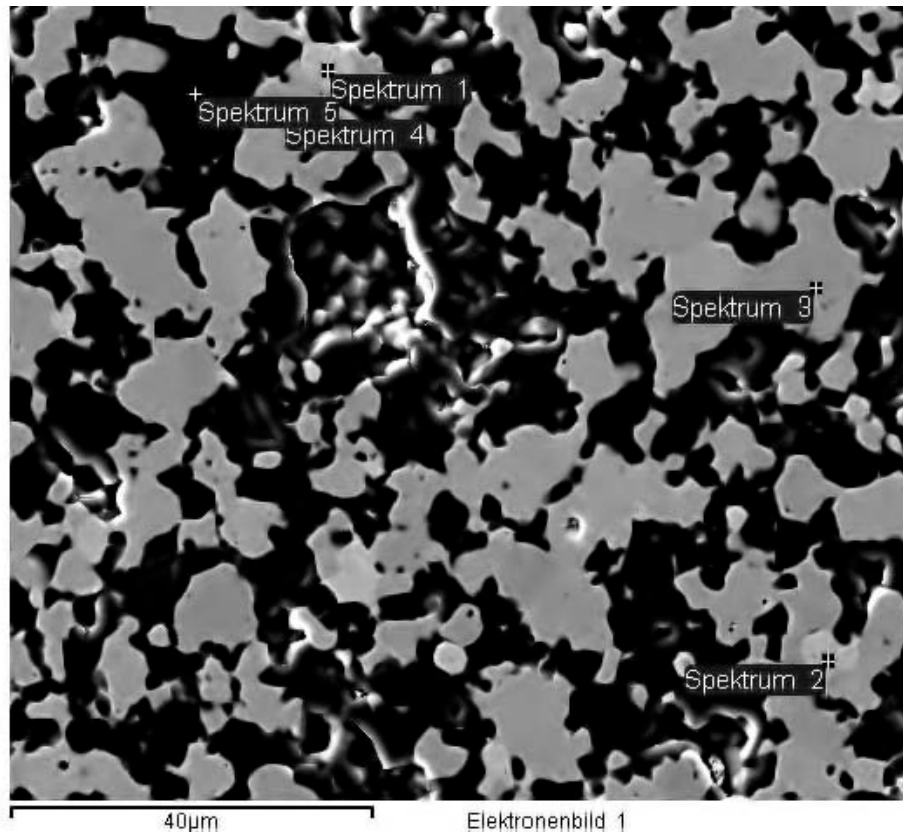
Spektrum	In Statistik	B	C	Si	Zr	Hf
Spektrum 1	Ja	18.52505	52.63655		27.62228	1.216127
Spektrum 2	Ja		65.73185		33.38235	0.8857954
Spektrum 3	Ja	77.27189			22.72811	
Spektrum 4	Ja	76.57462			23.42539	
Spektrum 5	Ja		58.76441	41.23559		

Alle Resultate in Atom%

Fig. 3.7. Results of EDX chemical analysis of USS6 composite

The state diagram of Zr-Si system presented in Fig. 3.8 points out to perytectical type of $ZrSi_2$ decomposition with an appearance of Zr-Si liquid phase at the temperatures of hot pressing exceeding 1620 °C. The interaction of this liquid with the charge components can lead to the formation of some intermediate compounds, the latter being confirmed in the XRD pictures. The analysis points out to the following reaction:

$$ZrSi_2 \rightarrow ZrSi_x + \text{Zr-Si (L)}.$$

The interaction of liquid components (Zr and Si) with the basic phases of composite leads to the formation of ZrC, $ZrSi_x$ and SiB_x intermediate compounds as well as enrichment of liquid by boron:
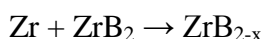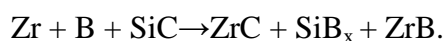
$$Zr + ZrB_2 \rightarrow ZrB_{2-x}$$

(this reaction is responsible for the formation of ring structures in boride grains),

$$Zr + SiC \rightarrow ZrC + ZrSi_x ,$$

$$Si + ZrB_2 \rightarrow ZrSi_x + SiB_x + \text{Si-B (L at } T_{hp} > 1800 \text{ °C)},$$

$$Zr + B + SiC \rightarrow ZrC + SiB_x + ZrB.$$
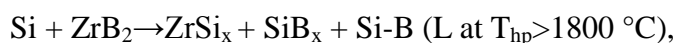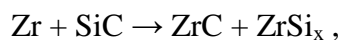
The interaction of intermediate phases with each other leads to the formation of secondary zirconium diboride and silicon carbide:

$$ZrC + Si + SiB_x \rightarrow ZrB_2 + SiC;$$

$$ZrSi_x + ZrC + SiB_x \rightarrow ZrB_2 + SiC.$$
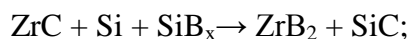
It can be noted that a possibility of some reactions pointed out is confirmed by appropriate approximate thermodynamical calculations as well as a possibility of chemical reactions with the participation of "cluster structures". The presence of CO-CO_2 medium which is a second (after silicon carbide) source of carbon in the system was not taken into account.

The formation of liquid itself promote the composite compaction by the mechanism of liquid-phase sintering. At high content of zirconium silicide (more than 20 % in USS45-USS46 composites) the large amount of Zr-Si-B liquid being formed leads to an appearance of amorphous phase which was found out by XRD method.
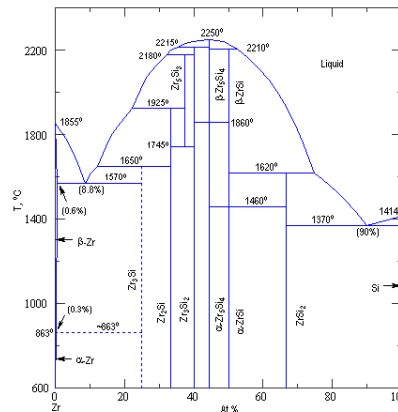
Fig. 3.8. State diagram of Zr-Si system.

The EDX spectra (Fig. 3.10) confirm the conclusion above as well as point out that in the third phase of USS sets there are the hafnium additives. Since this is almost not observed in the samples of US set, one may suppose that the hafnium got into the system together with $ZrSi_2$, the latter playing the main role in the mechanism of ZrB cubic phase formation. Further, the role of ZrB cubic phase in the mechanisms of sintering process and high-temperature oxidation of ceramics themselves will be shown.
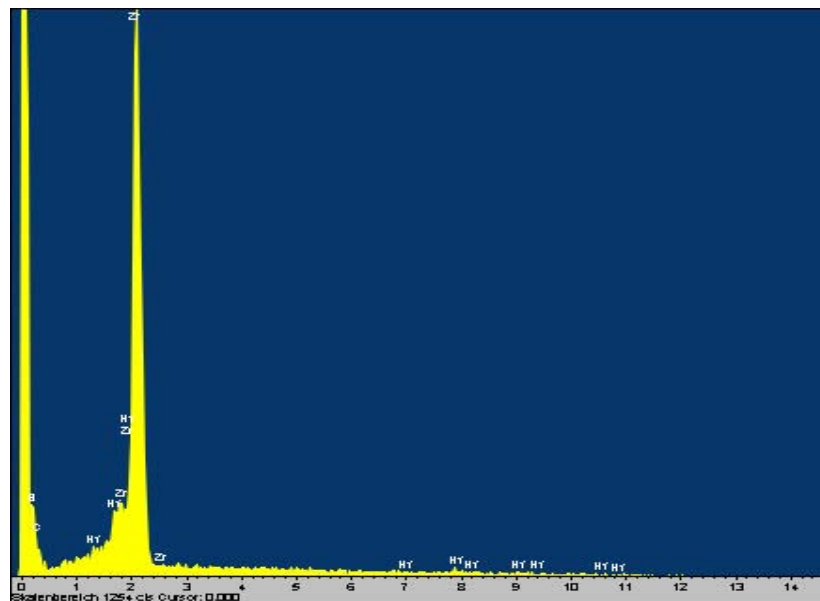
Fig. 3.10. EDX spectrum of third phase grain of USS4 sample

In Fig. 3.8 one can see the lattice parameters of this cubic phase while in Fig. 3.9 – the dependence of cubic phase volume content on $ZrSi_2$ content. The microstructure of ceramic composite with grains of cubic phase and results of EDX local analysis are presented on Fig. 3.10.
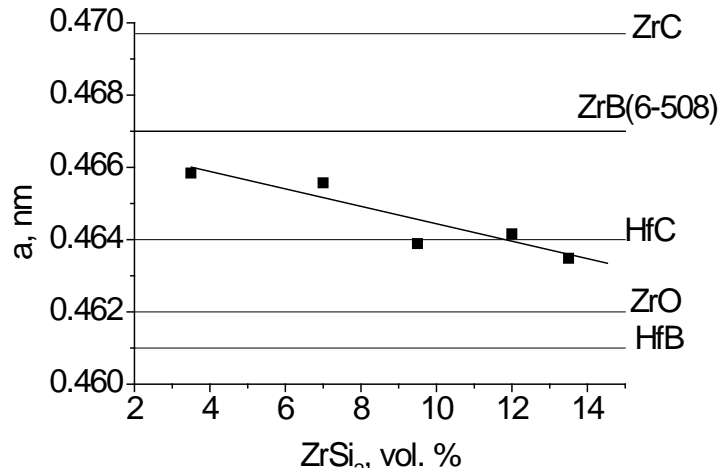
Fig. 3.9. Lattice parameters of new cubic phase in comparison with known ones.
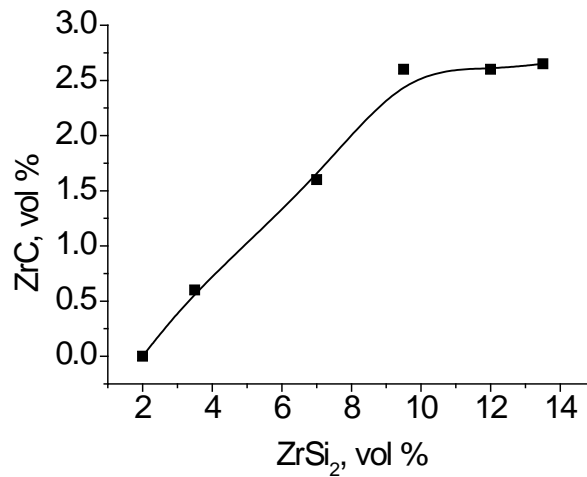
Fig. 3.10. Dependence of cubic phase volume content from $ZrSi_2$ volume content in the

charge.
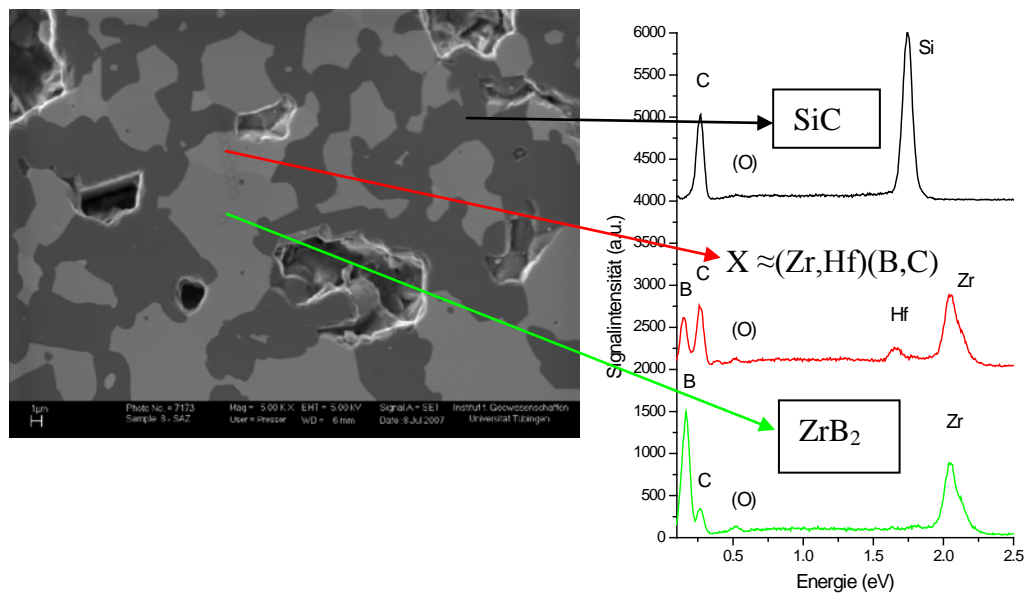
Fig. 3.11. Structure and chemical composition of ceramics.

As it was shown at the analysis of structures obtained as well as shrinkage curves for composites under hot pressing in combination with strength data, the introduction of zirconium silicide in the charge composition was accompanied by sintering activation with a growth of shrinkage rate at given temperature and/or a possibility to obtain dense material at the decrease of ceramics hot pressing temperature by 150 – 200 °C, compared with the ceramics which did not contain zirconium silicide. The activation of sintering by the zirconium silicide additives also allows ensure low porosity of composites with a high content of silicon carbide (Fig. 3.12).
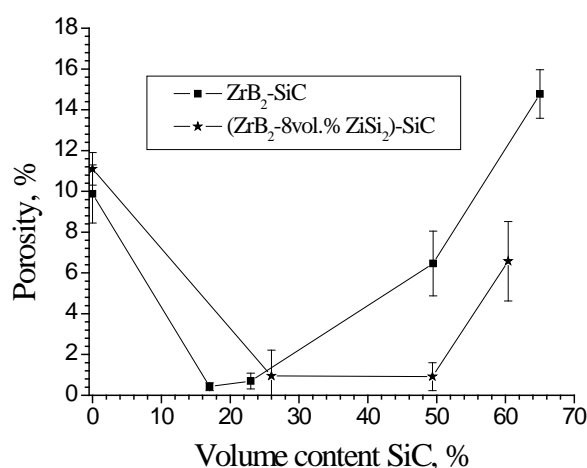
Fig. 3.12. Dependence of porosity on ceramics composition.

Microscopy and XRD-research of phase ZrB_2-$MoSi_2$ composition.

On the XRD – pattern of the charge (Fig. 3.13) the lines of charge components are detected as well as the additional lines of additive phase (possibly, similar to MoB_2 in the quantity $\leq 1\%$). As a result of charge components interactions under the regimes of hot pressing the phase composition of ceramics in the surface layers is essentially changed. Resulting from a partial oxidation the small amounts of zirconium oxide are present. As a rule, the Zr(CB) phase with the lattice of NaCl type is observed (the same as in the ZrB_2-SiC system). At the temperatures of the pressing in the interval of 1750-1900 °C and small times of isothermal exposure the phase of SiC and MoB_2 were found (see Fig. 3.14)

At the optimum regimes of hot pressing the composition of hot-pressed samples proved to be near to the charge compositions, howeverSiC and ZrO_2 phases are also observed (Fig. 3.15)

As a whole, the results obtained testify that under used hot pressing conditions the interaction of charge components with the participation of $MoSi_2$ results in formation of SiC and molybdenum borides as well as Zr(CB) cubic phase.
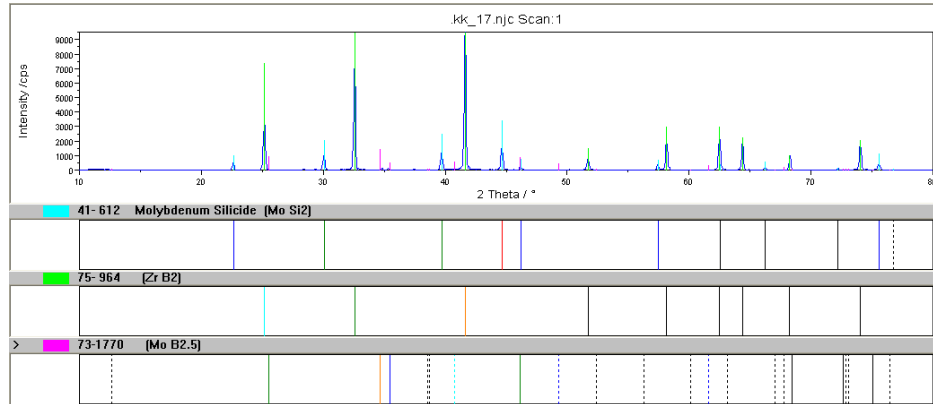
Fig. 3.13. Typical XRD picture of ZrB_2-$MoSi_2$ charge.

The structure of materials obtained is shown in Fig. 3.16. One can see from microphotos that the grain size of main grains achieves the value of 10 μm.
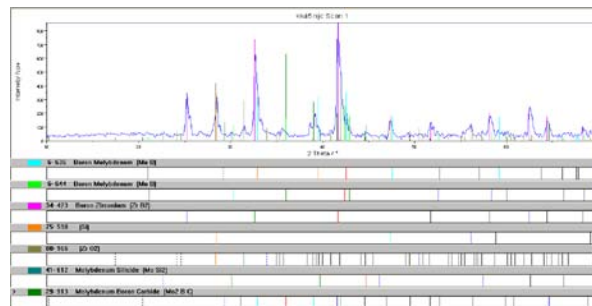
Fig. 3.14. XRD pictures of hot-pressed samples of MP5 composition obtained at 1830 °C.
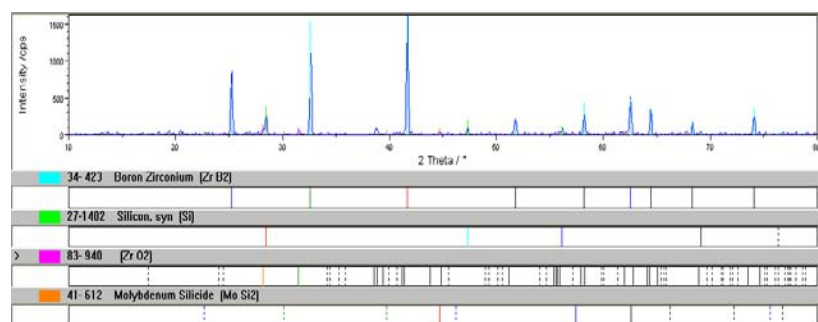
Fig. 3.15. XRD-pattern of hot pressed sample of M4 composition.
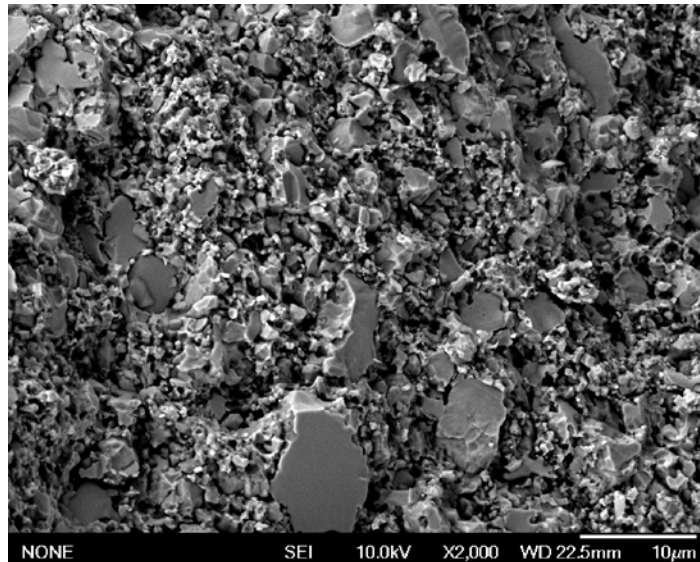
Fig. 3.16. SEM picture of as-received M4 sample (ZrB_2-44 w. % $MoSi_2$).

ZrB_2-SiC-B_4C system.

Three-hour milling of charge results in non-homogeneous, to a large extend, composition of hot-pressed ceramics. Agglomerations of ZrB_2 can reach the size of 30 microns, the fluctuation factors for volume fraction of the second phase in micro- and in macro volumes are high (Fig. 3.17).

The appearance of big agglomerations in the studied system can be connected with increased differences in density of SiC - ZrB_2 - B_4C, which may cause powders stratification at the phase of charge drying due to high density of ZrB_2. Moreover, ceramics polished surfaces are characterized with greater apparent porosity, resulted from material pitting in abrasive processing.

This certifies to a decreased strength of interphase boundaries and/or an increased level of interphase thermal stresses, which directly follows from the large CTE difference of SiC and ZrB_2 phases. Therefore, to ensure high strength, SiC - ZrB_2 ceramics should have higher parameters of dispersion and structural homogeneity. The prolongation of milling time up to 7 - 9 hours together with milling quality control made possible to attain necessary characteristics of structural homogeneity and dispersion and to obtain bend strength for the samples with high ZrB_2 content, at the 4-point testing scheme, of 530 - 570 MPa (Table 2.10).

a

b
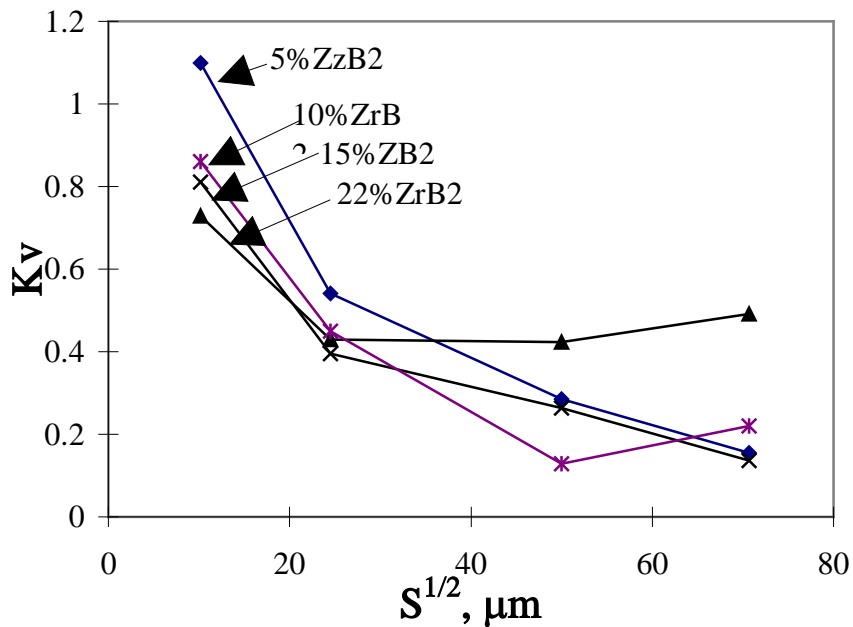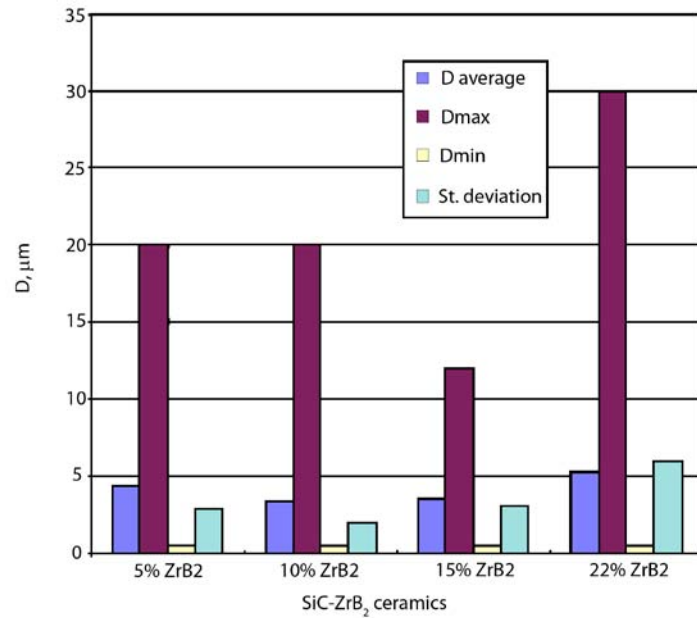
Fig. 3.17. ZrB$_2$ grain size (a) and fluctuation factor K$_v$ for ZrB$_2$ volumetric content (b) for SiC - ZrB$_2$ composites.

3.3. Study of strength properties of UHTCs.

UHTC structure and composition optimization.

Region of brittle fracture of ceramics under study extends to the 1600-2000 °C. At higher temperatures (2000 – 3200 °C) mechanical behaviour is determined by plastic deformation processes that can also lead to fracture. The peculiarity of ceramic materials where relaxation of internal stresses is absent in the first interval and stress relaxation is impeded in the second is

determined by the extreme importance of stress concentrators and inhomogeneities. This is the reason why the analysis of stress-strain state of the ceramic composite with the aim of investigation of dependence of fracture characteristics on non-homogeneous fields of internal stresses is so important.

The present analysis considers thermal stresses, stipulated by the difference in linear expansion coefficients (α) of composite phases. Taking into account the material's macroscopic homogeneity and isotropic distribution of phase components, one can make an assumption on hydrostatic nature of tensile and compressive stresses in each of its phase $(\sigma_{11})i = (\sigma_{22})i = (\sigma_{33})i = \overline{\sigma}_i$, governed by the conditions of stress equilibrium $\Sigma Y_i \overline{\sigma}_i = 0$. Calculation of internal thermal stresses in composites was performed on the base of statistical approach [29], using physical characteristics from each phase and the following ratios:

$$\langle \sigma_{ij} \rangle_1 = Y_2 \eta \delta_{ij} ; \qquad \langle \sigma_{iij} \rangle_2 = -Y_1 \eta \delta_{ij} ;$$

$$\eta = \frac{\gamma}{K_1 K_2 + \langle K \rangle \gamma} \{(K_1 - K_2)p_s - 3K_1 K_2 [(\alpha_1 - \alpha_2)\Delta T + (l_1 - l_2)]\} ;$$

$$\gamma = (4/3)\langle G \rangle ; \quad \langle G \rangle = Y_1 G_1 + Y_2 G_2 ; \quad \langle K \rangle = Y_1 K_1 + Y_2 K_2 ;$$

Intensity of internal stresses could be characterized by internal energy, which relates to the unit of micro volume,

$$\langle U \rangle = Y_1 \langle U_1 \rangle + Y_2 \langle U_2 \rangle ;$$

The internal energies of components are defined as:

$$\langle U_1 \rangle = \frac{\eta^2 Y_2^2}{2K_1} ; \qquad \langle U_2 \rangle = \frac{\eta^2 Y_1^2}{2K_2}$$

Where G_i is the shear modulus of i-th phase; E is the Young's modulus; ν is the Poisson's ratio; Y_i is the volume fraction of i-th phase; α_i are the coefficients of linear temperature expansion; K_i is the modulus of bulk compression of i-th phase; l_i is the specific volume of i-th component; p_s is the external pressure at sintering; U_i is the internal energy of elastic strain of i-th phase.

At known values of elastic and thermal characteristics of composite phases, the value of internal stresses is determined by ΔT - temperature differences between the temperature of viscous-elastic transition T_{ve} and final temperature, down to which the material is cooled after hot pressing (typically, room temperature).

From the results of the calculations (Fig. 3.18), the maximum value for the internal tensile and compressive stresses reaches approximately 2 GPa in ZrB_2 and SiC, respectively, and take place for even a small content of the corresponding phases. With an increase of the content of

these phases the stresses level in them decreases. The dependencies of specific energy of elastic deformation on composition are presented in Fig. 3.18.

The values of specific energies of elastic deformation of the phases are maximized in the range of 25-40 % of the same phase content. Thus, the total specific energy of elastic deformation of the composite (U_{total}) was found to be a maximum at the equivolume phase content. This determines the tendency of the ceramics to spontaneously fracture due to thermal stresses.

The increase of composite fracture toughness and strength can be achieved by such selection of components, ratios their volume fractions and grain sizes, when the matrix, subjected to the effect of residual thermal stresses, will be in compressed state, and isolated second phase inclusions - in tension state. The crack than will be forced to propagate in compressed matrix, coming around second phase, due to the peculiarities of non-homogeneous field of stresses in their vicinity.

We used the mathematical formulation of fracture toughness criteria for the ceramic matrix composite and optimization method for composite composition and structure[30], taking into account the fields of internal thermal stresses.
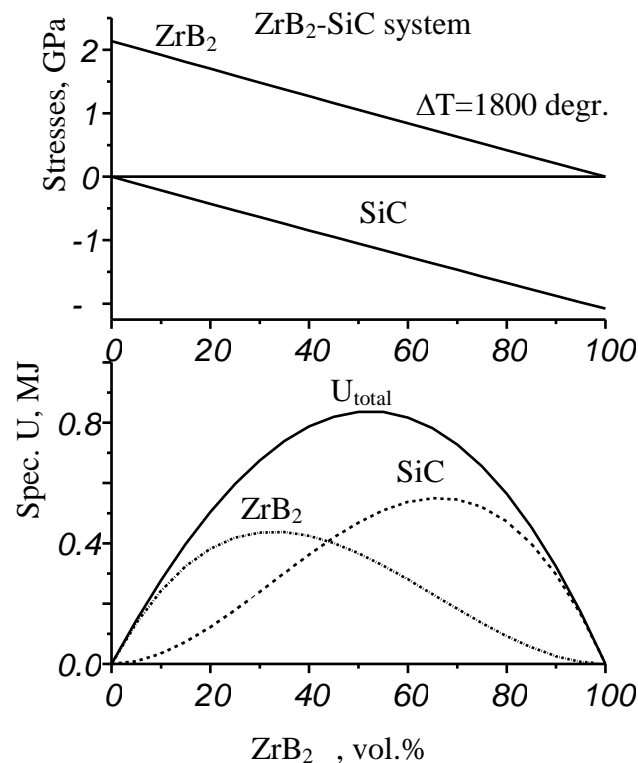
Fig. 3.18. The dependencies of internal stresses and specific energy of elastic strains U in SiC and ZrB$_2$ composite phases versus ZrB$_2$ content.

In simple cases, composite fracture toughness is expressed by the relation:

$$\widetilde{K}_I = \widetilde{K}_{Ic} = \min_i (a_i^{-1} (K_{Ic}^i - D\sigma^{ri}));$$

and optimum composite composition is determined by the criteria:

$$\widetilde{K}_{Ic}^{opt} = \underset{Y}{MAX}\ \underset{i}{MIN}\ (a_i^{-1} (K_{Ic}^i - D\sigma^{ri}));$$

$$\alpha_i = \frac{G_i |Y_i|}{\sum\limits_{i=1}^{N} G_i |Y_i|} \le 1; \qquad\qquad D = \frac{2\sqrt{C}}{\pi}$$

where σ^{ri} are the residual thermal stresses; G_i is the shear modulus of i- phase; C is the typical size of initial defects (cracks); K_I is the stress intensity factor for normal fracture (opening mode); K_{1C}^i is the fracture toughness of i-th component of composite.

Composite parameters, that were used in calculation of K_{1C}, are elastic phase characteristics, fracture toughness values of composite components and parameter D.

Generally, the introduction of high-TEC (thermal expansion coefficients) component into composite is accompanied by fracture toughness growth. The maximum of fracture toughness is shifted to lower second phase contents with an increase of mismatch of TEC, elastic characteristics as well as the typical size of structural defects (microcracks). Similar results were obtained for SiC-based composites with additives of other borides (TiB_2). For SiC-TiB_2 composites this conclusion is confirmed experimentally. However, in the case of ceramics with zirconium boride its high sintering capacity, compared with silicon carbide, as well as a presence of third (grain boundary) phases allows to obtain dense composites at high content of ZrB_2. Therefore, in this Project we studied systems mentioned above in the wide range of ZrB_2/SiC ratios.

The results of the calculations are presented in Fig. 3.19. According to the calculations, the compositions based on silicon carbide matrix appear to be the preferable ones. For the purposes of these calculations, the size of the microcracks was assumed to be equal to the average grain size, considered the same for both phases of composite. In the ZrB_2-SiC system, differences in the elastic characteristics and coefficients of thermal expansion are moderate. The calculations show that high fracture toughness can be achieved in a range of high zirconium diboride content (45-50 vol.%) with a small grain size (~ 2 μm). With an increase in grain size, the fracture toughness maximum shifts in the direction of lower zirconium diboride content while the fracture toughness minimum forms in the range of an equivolume content of components. For example, at defect

sizes of approximately 30 μm (this size can match the size of grains or agglomerates of ZrB_2) fracture toughness in the range of 45-50 vol. % ZrB_2 is decreased to values near zero. This corresponds to the criterion of spontaneous fracture of ceramics under the action of thermal

stresses, $2C_{cr} = 2 \underset{i}{MIN} \left[\left(\dfrac{\alpha_i^{-1} K_{1C}^i}{(2/\sqrt{\pi})\sigma^{ri}} \right)^2 \right]$,

where C_{cr} is the critical grain size for spontaneous failure under the action of thermal stresses.

It is well known that the reduction of grain size is accompanied by strength increase at ambient temperature. At present, there are technological sintering processes which indeed allow manufacture ZrB_2-SiC ceramics with an average grain size of 2 μm or less. In the region of equivolume phase contents it predicts a maximum in both fracture toughness and strength values due to both peculiarities of the internal stress-strain state and fine grain structure (d_{gs}~1-2 μm). However, at high temperatures fine grain size is expected to increase both creep and high-temperature oxidation rate[31-32]. That is why in this study such powders are used which gave a possibility to obtain ceramics with the grain size ~10-15 μm, which was very important for an assurance of basic level of properties over a wide temperature range. At such grain size, in order to preserve the necessary level of low-temperature fracture toughness (compensating for a certain decrease of strength because of structural roughening), ZrB_2 content should be reduced to 25-30 %, i.e. to turn from ZrB_2 –based to SiC-based composites.
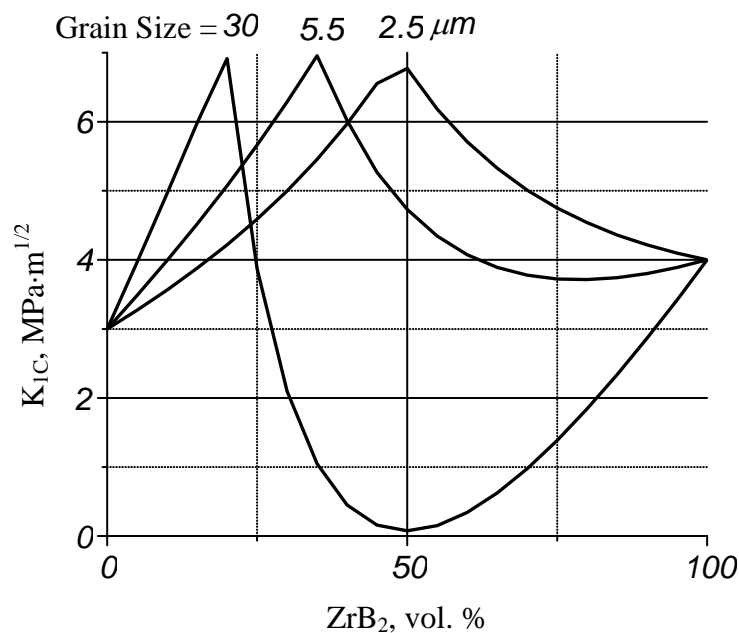
Fig. 3.19. Influence of grain size and composition on the fracture toughness of ZrB_2-SiC ceramics.

3.3.1. Room-temperature properties.

US1-US6, USS1-USS6 compositions.

In the framework of the study of mechanical properties the investigation of strength and hardness of composites at room temperature has been carried out. We measured hardness and strength under bending of hot-pressed ceramic materials of ZrB_2 –SiC and ZrB_2 – $ZrSi_2$ – SiC systems.

The research fulfilled showed that the bending strength of the composites directly depends on residual porosity and at small porosity ($\leq 5\%$) has high level. The tests of ZrB_2 –SiC and ZrB_2 – $ZrSi_2$ – SiC composite samples at the three-point bending ascertained that the maximum strength (460-440 MPa) was realized at SiC content of 17-23 vol.% (Fig. 3.20). The comparatively low values of bending strength obtained on this stage of investigations are connected with the porosity and large grain size.
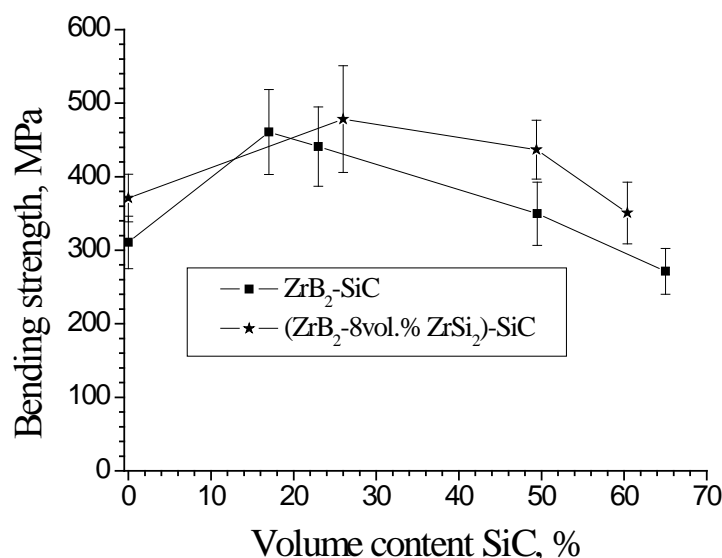
Fig. 3.20. Bending strength of hot-pressed ceramic materials of ZrB_2 –SiC and ZrB_2 – $ZrSi_2$ – SiC systems in dependence on SiC volume content in composite.

The investigations of structure, residual porosity and bending strength enabled to establish the optimum temperature and hot pressing pressure necessary for manufacturing of dense and strength composites. However, in the course of this study, the thermal instability of ceramics which contained in their charge zirconium disilicide additives has been found. At the hot pressing pressure of 30 MPa and temperature of 2125 °C sintering time of 15 min proved to be the optimum one for the chosen geometry of samples (beads of 6x6x35 mm sizes). The increase of

isothermal exposure time up to 45 min which is equivalent to additional annealing of material under pressure was accompanied by essential increase of porosity (up to 12 %) and a decrease of strength characteristics (Fig.3.21).
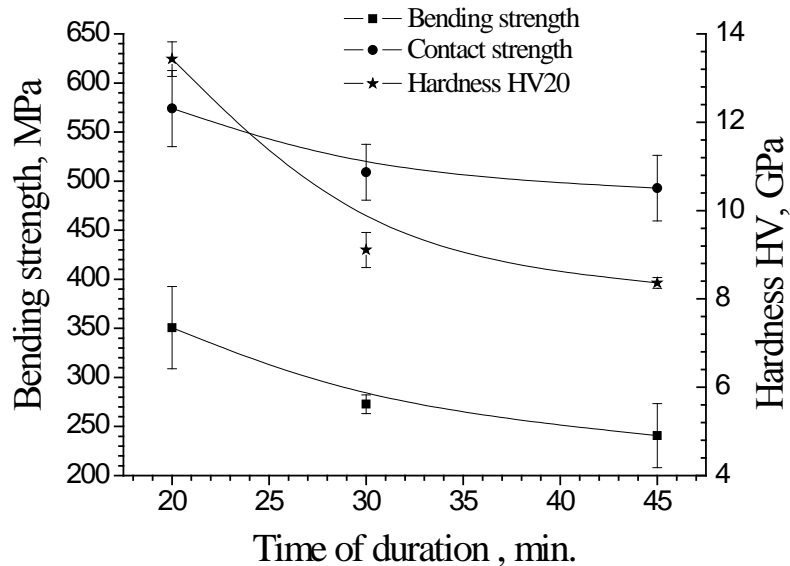
Fig. 3.21. Dependence of bending and contact strength as well as hardness of ($ZrB_2 – 8$ vol.% $ZrSi_2$) –60.4 vol.% SiC composite on time of isothermal exposure.

The strength degradation is connected with peculiarities of phase compositions of ceramics at high $ZrSi_2$ content. With the increase of $ZrSi_2$ content to more than 8% a considerableamount of an unstable amorphous phase is present, and even appears grain-boundary porosity (Fig. 3.22).

a   b
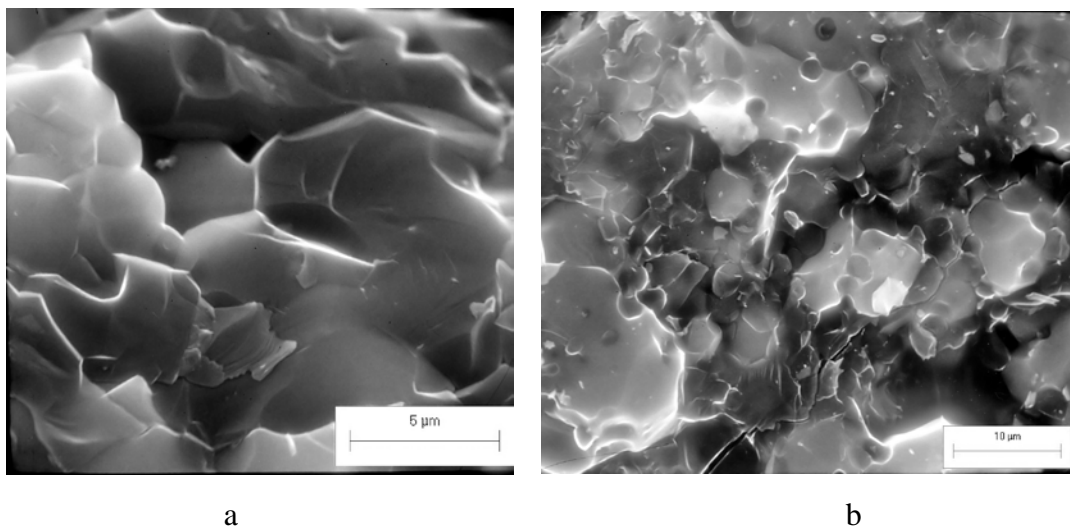
Fig. 3.22. Fracture surfaces of ceramics: a) 48% ZrB_2 – 2% $ZrSi_2$ – 50% SiC;
b) 36% ZrB_2 – 14% $ZrSi_2$ – 50%SiC.

The contact tests of ZrB_2 –SiC and ZrB_2 – $ZrSi_2$ – SiC ceramics showed that in the wide load range (2-300 N) these composites retained high hardness values (Fig. 3.23). It testifies that the materials have high resistance to fracture, especially under conditions of concentrated impact loads and erosion. One can see in Fig. 3.23 that at the decreasing of load up to 2 N hardness of all the samples rises while at the loads of 50-100 N there is a dip of hardness for some samples, and in the range of 156-300 N hardness practically does not change. The analysis of the data obtained shows that the introduction of SiC into the composite increases their hardness (Fig. 3.24). The composites with 49.4 vol.% SiC have the maximum hardness (~16-18 GPa).
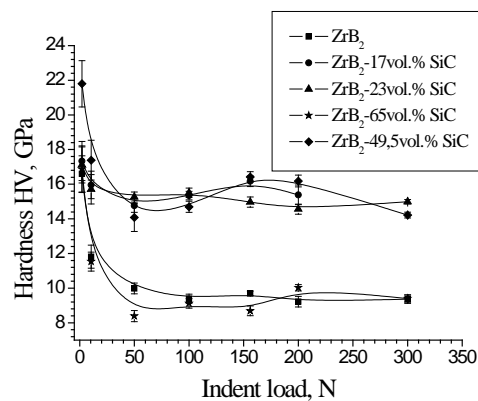
(a)
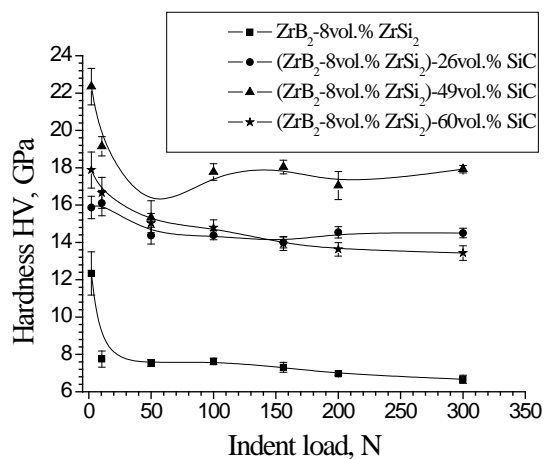
(b)

Fig. 3.23. Dependence of hardness of ZrB_2 –SiC (a) and ZrB_2 – $ZrSi_2$ – SiC (b) ceramics on the load to indenter.
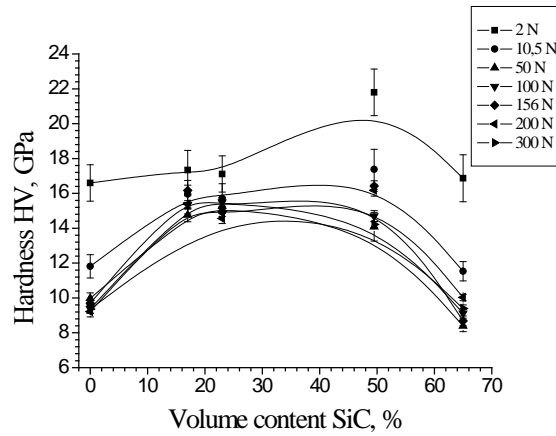
(a)
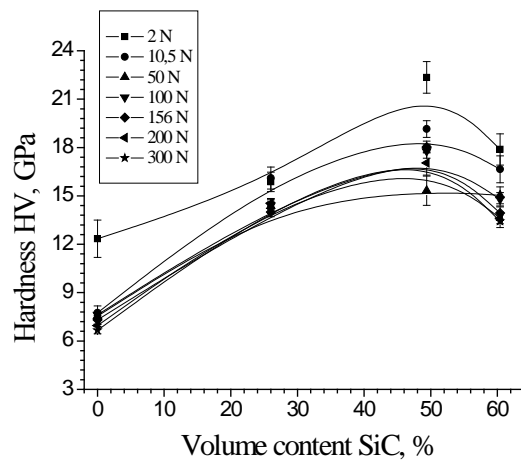
(b)

Fig. 3.24. Dependence of hardness of ZrB_2 –SiC (a) and ZrB_2 – $ZrSi_2$ – SiC (b)

ceramics on SiC content.

The results on the ZrB_2-SiC and ZrB_2-$ZrSi_2$-SiC composites fracture toughness are presented in Fig. 3.25. Here one can see that the fracture toughness depends on the indenter load. In the majority of cases the growth of load leads to the decrease of calculated fracture toughness. The increase of SiC volume content in ZrB_2-SiC composites leads to the increase of their fracture toughness (3.4 – 8.4 $MPa^*.m^{1/2}$). In the case of ZrB_2-$ZrSi_2$-SiC composites (Fig 3.25, b) the maximum values of fracture toughness (5.5 – 7.1 $MPa^*m^{1/2}$) are observed at 20 -30 vol.% SiC. Such behavior of ZrB_2-$ZrSi_2$-SiC composite is caused by both stress redistribution between phases and effect of mesoscopic mechanisms of toughness growth (phenomena of cracks tilting near inclusions of other phases and microcracking).

(a)

(b)
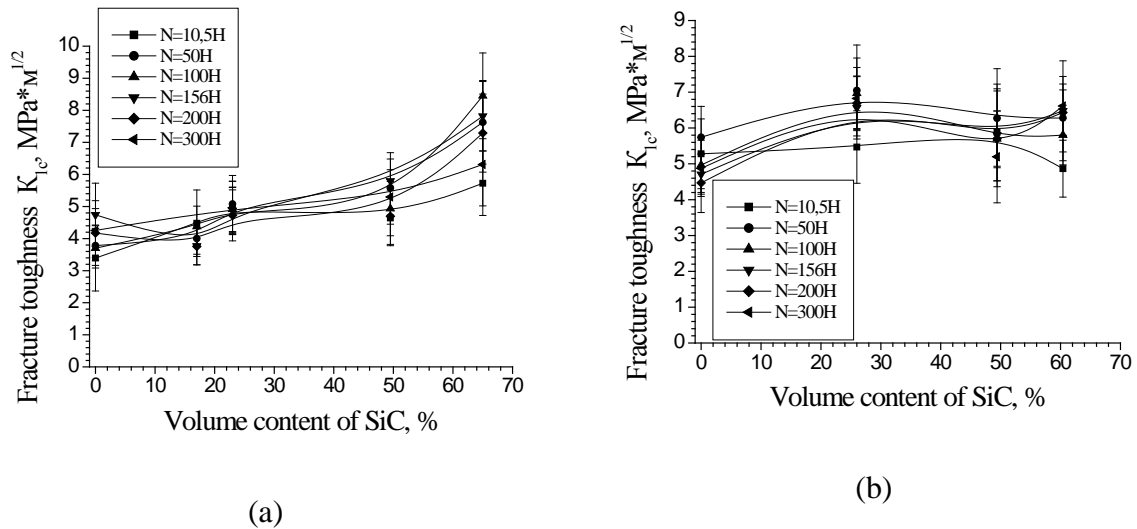
Fig. 3.25. Dependence of ZrB_2-SiC (a) and ZrB_2-$ZrSi_2$-SiC (b) ceramics fracture toughness on the SiC content and indenter load.

On the basis of hardness measurements carried out as well as length measurements for cracks which were formed around hardness indentation we have built the Weibull's statistic distributions for the contact strength of ZrB_2-SiC and ZrB_2-$ZrSi_2$-SiC composites (Fig. 3.26).

(a)   (b)
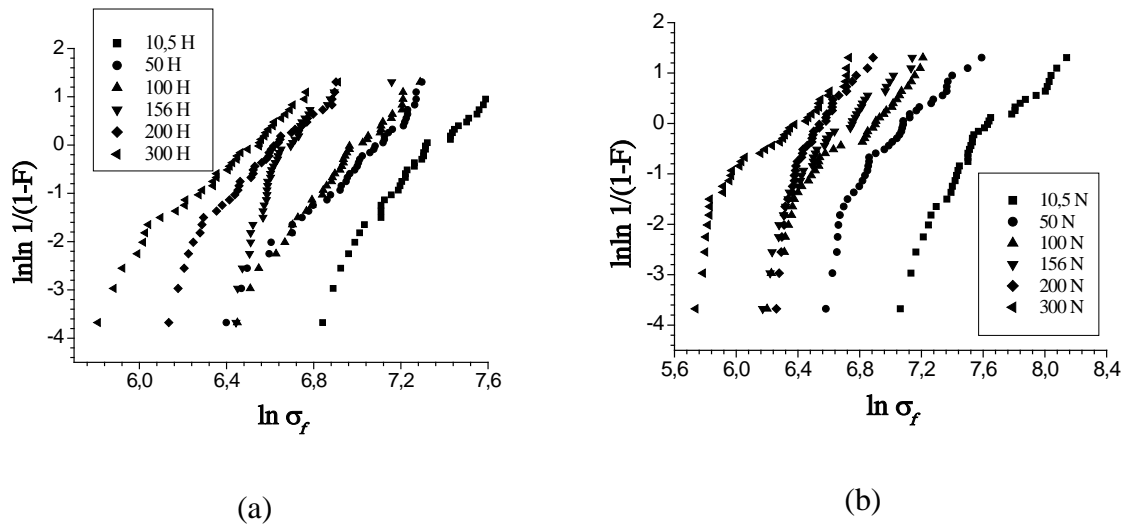
Fig. 3.26. Weibull's statistic distributions for the contact strength of ZrB_2- 65 vol.% SiC (a) and (ZrB_2-8 vol.% $ZrSi_2$)- 49.4 vol.% SiC (b) composites.

In the majority of cases the obtained distributions proved to be bimodal ones, i.e. they contain, as a rule, two straight line regions which correspond to two crack populations – "long" and "short" ones. Weibull module determined for "long" cracks varies in the range of 14 – 16 values while for the "short" ones it has the values in 3 – 5 range.

With a load growth the number of "long" cracks increases, the displacement of distribution to the left testifies to the decrease of contact strength characteristics. The separate Weibull analysis of "long" cracks population showed a scaled dependence of composite contact strength more clearly (Fig. 3.27). One can see in Fig. 3.27 that with the load increase the contact strength is sharply decreased and achieved the minimum value at the maximum load of 300 N.

(a)   (b)
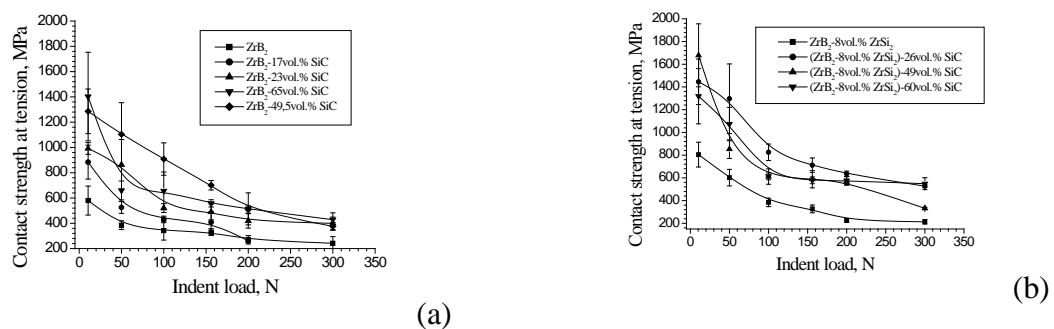
Fig.3.27. Dependence of ZrB_2-SiC (a) and ZrB_2-$ZrSi_2$-SiC (b) ceramics contact strength on the indenter load.

The results of calculation of contact strength at tension (CTS) and compression (CCS) as well as microstructure strength of ZrB_2-SiC and ZrB_2-$ZrSi_2$-SiC composites are presented in Fig. 3.28.

(a) (b)
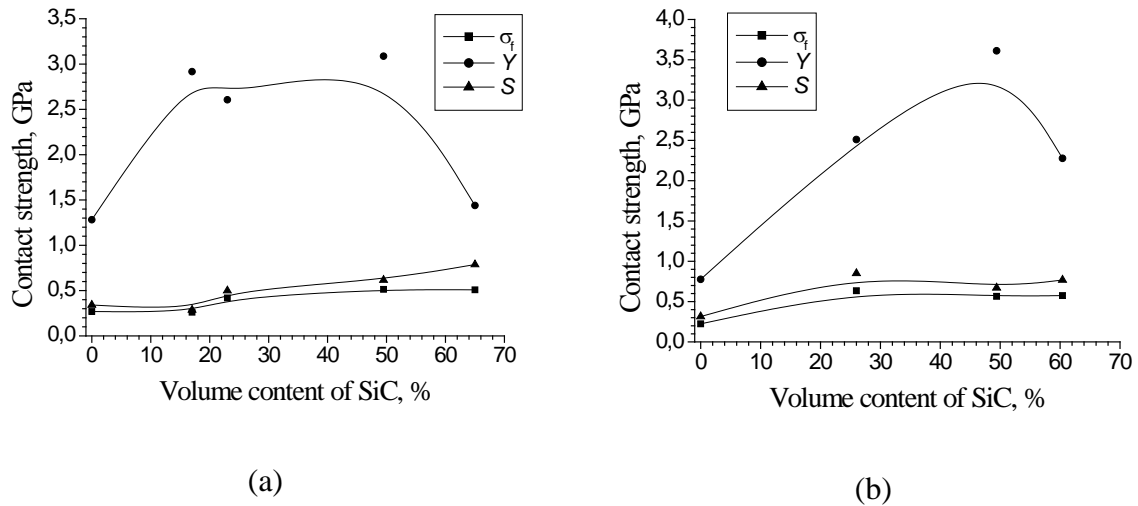
Fig. 3.28. Dependence of contact strength at tension CTS) and compression (CCS) as well as microstructure strength (S) of ZrB_2-SiC (a) and ZrB_2-$ZrSi_2$-SiC (b) ceramics on SiC content (load 200 N).

One can see in Fig. 3.28 that the introduction of SiC to the composites significantly increased characteristics of contact strength. The composites of ZrB_2-$ZrSi_2$-SiC system compared with the ZrB_2-SiC ones, as a whole, are characterized by a higher level of contact and microstructure strength. For ZrB_2-SiC system high values of contact strength at compression take place in the wide range of composition whereas for ZrB_2-$ZrSi_2$-SiC maximum of contact strength at compression is observed for high content of silicon carbide. It should be noted that introduction of SiC in both types of composites increases microstructural strength and decreases damage of material under thermal-mechanical action. The average values of contact strength (CTS) are characteristic for the "long" cracks type, and they are by 100 – 150 MPa higher than bending strength (Fig. 3.28).

Thus, the ceramic materials developed may be also successfully used under conditions of contact loading.

USS41-USS46 compositions.

The results of hardness measurements of these materials showed that in the wide interval of loads (2–300 N) these composites retained high hardness values (Fig. 3.29). Hardness of all samples with a decrease of load up to 2 N has increased. However, in the range of loads 10.5–50 N practically all composite samples have an inclination to microcracking with a resulting reduction of hardness.

With further increase of load hardness somewhat grows and is practically varied. The analysis of data obtained shows that introduction of $ZrSi_2$ to the composition increases hardness (Fig. 3.30).
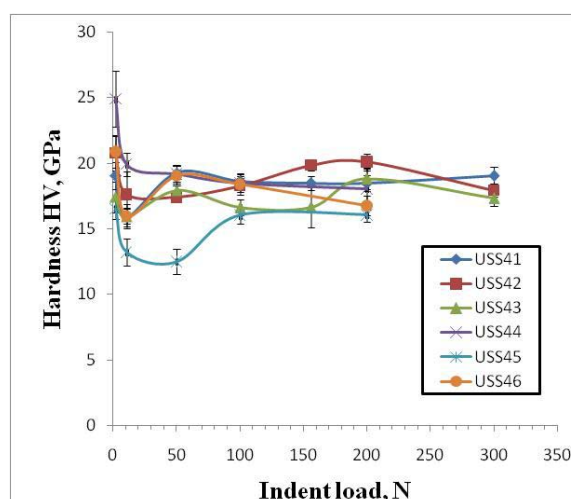
Fig. 3.29. Dependence of ZrB_2-SiC-$ZrSi_2$ ceramics hardness on the load to in an indenter.
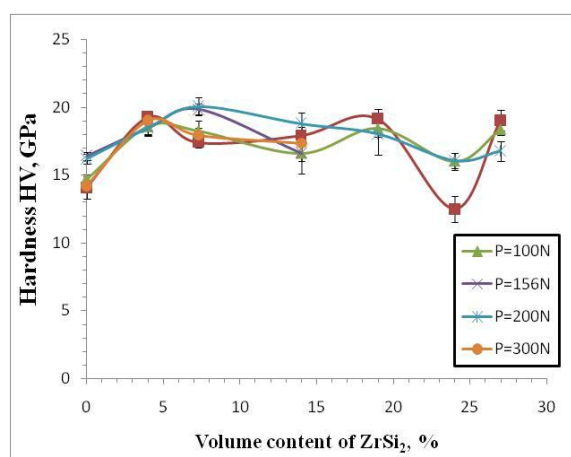
Fig. 3.30. Dependence of ceramics hardness on $ZrSi_2$ content.

Composites containing 4-20 vol.% $ZrSi_2$ are characterized by maximum hardness (19–20 Pa).

The data concerning ZrB_2-SiC-$ZrSi_2$ composite toughness coefficients are presented in Fig. 3.31. One can see that toughness coefficients depend on the load to an indenter. The increase of load, as it was also in the case of ZrB_2–$MoSi_2$, leads to the increase of calculated values of toughness coefficient. It may testify to the heightened resistance of composites to propagation of cracks.

From Fig. 3.31 can be seen that the increase of $ZrSi_2$ volume content in ZrB_2-SiC-$ZrSi_2$ composites has not practically affected their toughness coefficients, which was in the range of 2-3.4 $MPa \cdot m^{1/2}$.
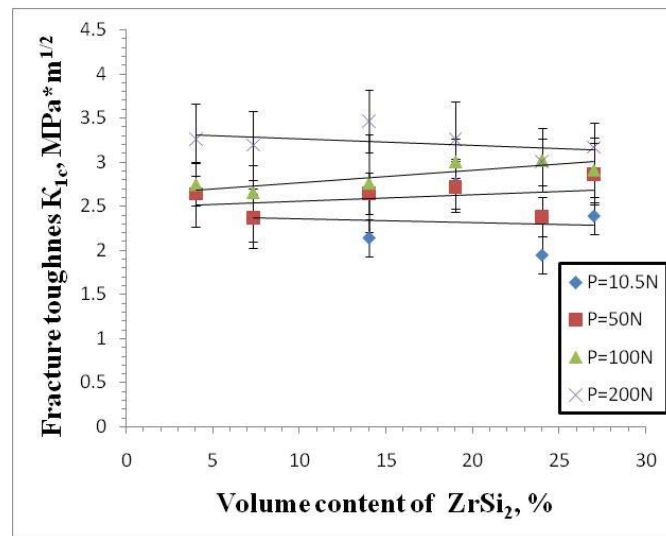
Fig. 3.31. The toughness coefficient of ZrB_2-SiC-$ZrSi_2$ ceramics materials in dependence on $ZrSi_2$ content and load to an indenter.

The statistical distributions of ceramics contact strength are presented in Fig. 3.32. The Weibull module m determined for the cracks is varied in the range of 17-21.

The dependence of contact strength HV on load H is presented in Fig. 3.33. Fig. 3.33 shows that with the increase of load the contact strength is sharply decreasing. But it is practically not varied in the wide load range (50-300 N).

As a whole, ZrB_2-SiC-$ZrSi_2$ composites are characterised by a higher level of contact strength than ZrB_2-$MoSi_2$ ones. The introduction of $MoSi_2$ to the composites (4-20 vol. %) significantly heightens their contact strength (Fig. 3.34).
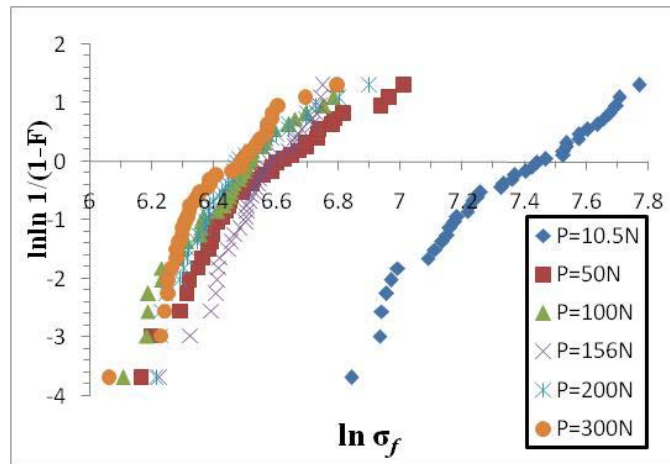
Fig. 3.32. Statistical Weibull's distributions for the contact strength of ZrB_2-SiC-7.5 vol % $ZrSi_2$ composition.
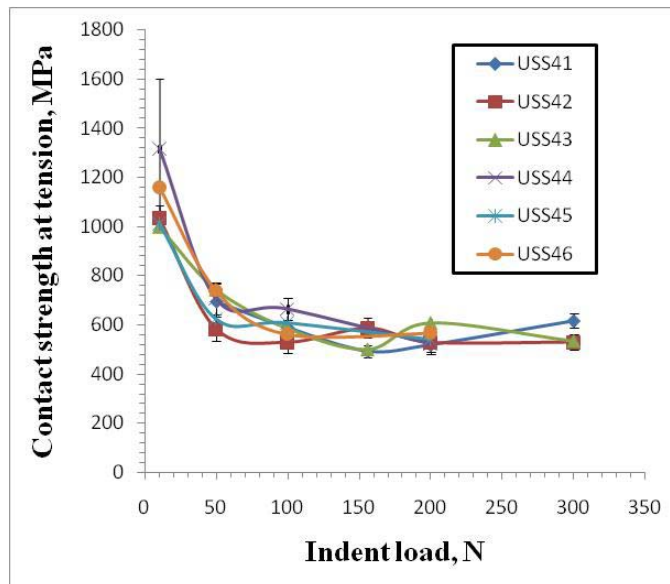
Fig. 3.33. Dependence of contact strength of ceramics of ZrB_2-SiC-$ZrSi_2$ system on the load to an indenter.
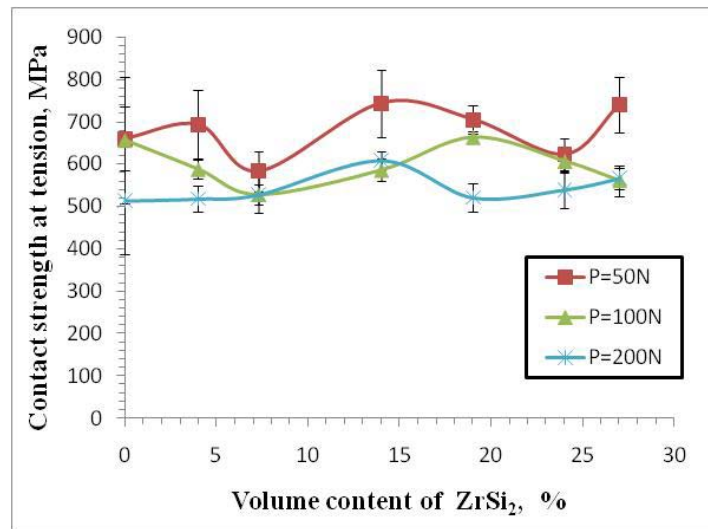
Fig. 3.34. Contact strength of ZrB_2-SiC-$ZrSi_2$ ceramics in dependence on content of $ZrSi_2$

These results are well coordinated with the data of macroscopic tests of ZrB_2-SiC-$ZrSi_2$ samples. Thus, the tests of ZrB_2-SiC-$ZrSi_2$ composites by three-point bending showed that the introduction of $ZrSi_2$ (4-20 vol.%) has led to an improvement of their strength characteristics (Fig. 3.35). Strength of such samples varies little and lies in the range of 400-450 MPa.
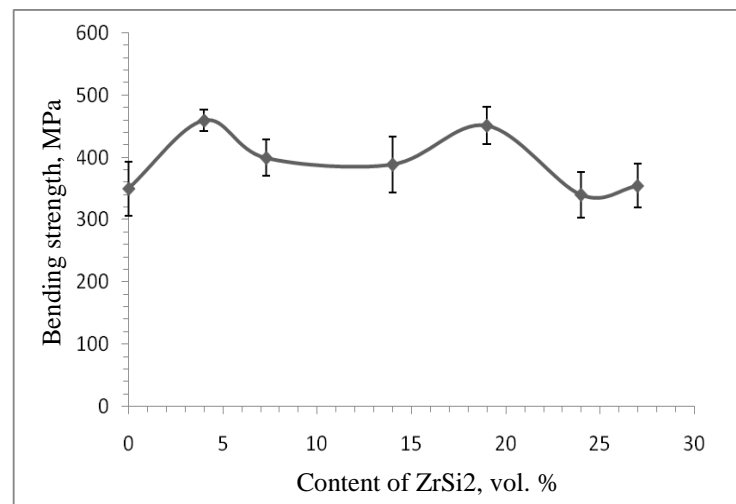
Fig. 3.35. Bending strength for hot-pressed ZrB_2-SiC-$ZrSi_2$ samples in dependence on $ZrSi_2$ volume content in the composite.

USS20-USS23 compositions.

We have continued the systematic study of US20 system composite with insignificant $ZrSi_2$ content using method of contact loading. The data on their hardness, fracture toughness and contact strength have been obtained.

Fig. 3.36 shows that the initial two-phase US20 composites have the highest hardness (17.8–14.6 GPa). The composite hardness is somewhat decreased at the rise of $ZrSi_2$ additive amount.
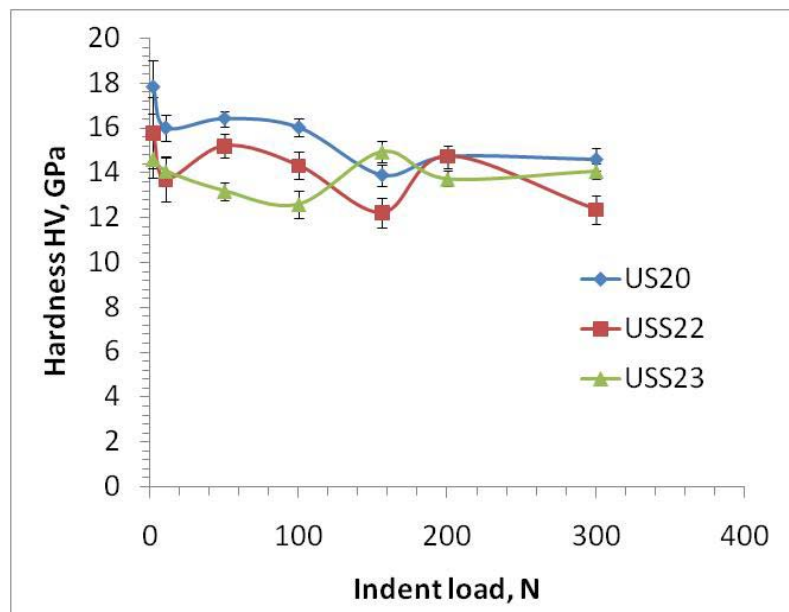
Fig. 3.36. Hardness of US-20, USS-22, USS-23 composite samples in dependence on loading.

It should be noted that the composite brittleness is decreased with the ZrB_2 volume content increase (see Fig. 3.37 and Fig. 3.38). The introduction of $ZrSi_2$ additive leads to the increase of USS-22, USS-23 composite contact strength as well as their fracture toughness, compared with US-20 samples. The corresponding values of these characteristics depend on the loading to indenter.
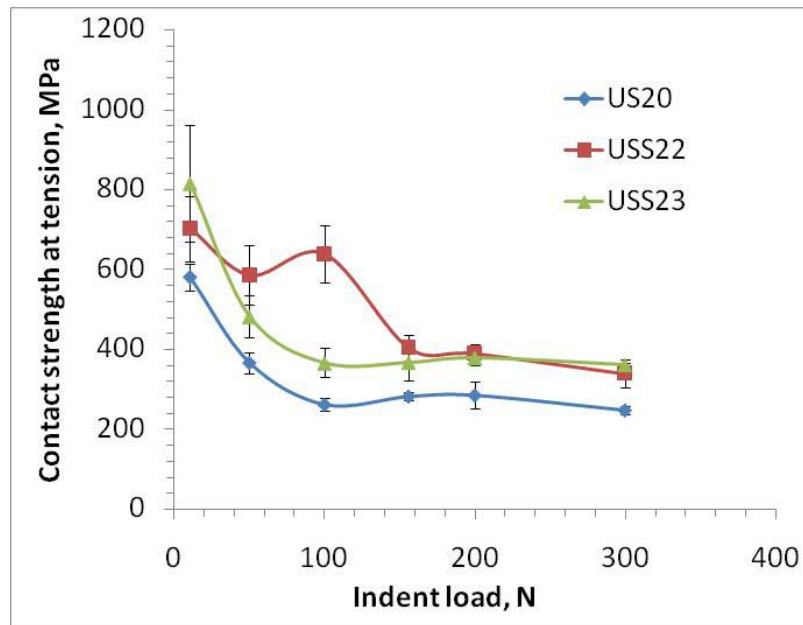
Fig. 3.37. Contact strength at tension of US-20, USS-22, USS-23 composite samples in dependence on loading.
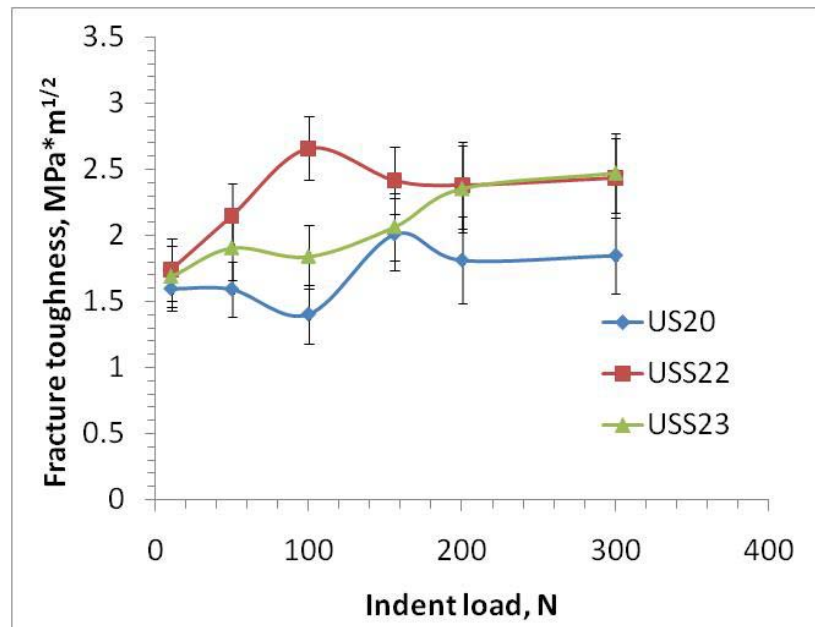
Fig. 3.38. Fracture toughness of US-20, USS-22, USS-23 composite samples in dependence on loading.

Fig.3.38 shows that the fracture toughness values depend on the loading to indenter. The increase of loading leads to the increase of the calculated fracture toughness. This unusual effect is connected with the increase of cracks length, and it points out to the increase of the resistance to

crack propagation at the failure. It testifies to the growing role of dissipative processes, accompanying the cracks growth, for example, in a micro-cracking process. Fig. 3.38 also shows that with the increase of $ZrSi_2$ volume content in the USS-22 system the increase of their fracture toughness is observed (up to 2.35–2.47 $MPa*m^{1/2}$).

Mechanical properties of ZrB_2-$MoSi_2$ ceramics.

Contact tests of ceramic materials of ZrB_2-$MoSi_2$ systems showed that in wide load range (92-300H) composites retain high hardness (Fig. 3.39). Fig. 3.39 shows that the decrease of load down to 2 N leads to the increase of hardness of all samples, at the load value of 156 N some samples show peculiar hardness peak, while in the 156-300 N range hardness is practically does not change.

The analysis of the data shows that the introduction of $MoSi_2$ into composition significantly lowers their hardness (Fig. 3.40). Composites which contain very small amount of $MoSi_2$ (7 vol. %) are characterized by maximum hardness (12.8-14 GPa).
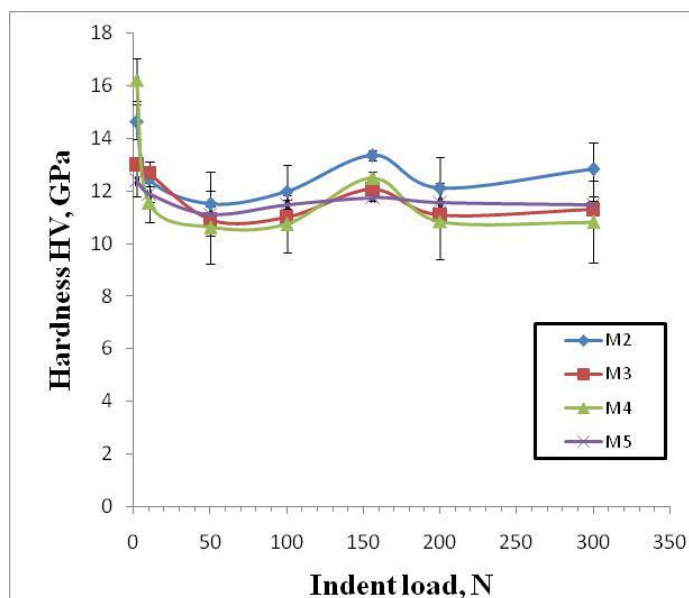
Fig. 3.39. Dependence of ZrB_2-$MoSi_2$ ceramics hardness on the load to indenter.
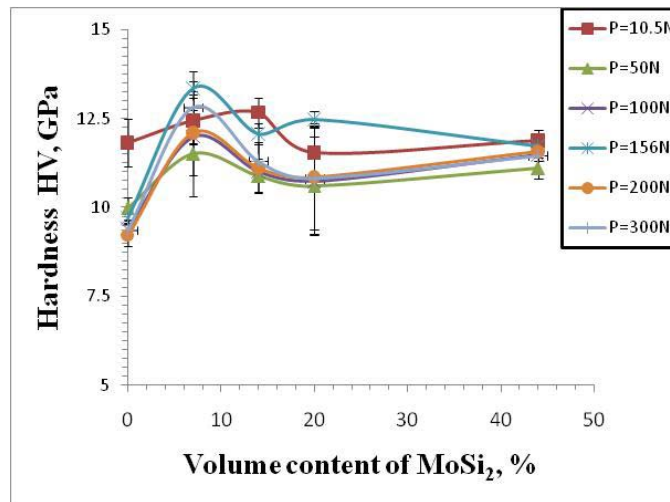
Fig. 3.40. Dependence of ZrB_2-$MoSi_2$ ceramics hardness on $MoSi_2$ content.

The obtained values of fracture toughness for ZrB_2-$MoSi_2$ system composites are presented in Fig. 3.41. One can see that the toughness coefficients depend on the load to indenter. Thus, in the majority of cases the growth of the load leads to the increase of calculated toughness coefficient. This comparatively unusual effect of toughness coefficient growth with an increase of load to indenter (i.e., in fact, with an increase of the length of cracks propagation) points out to a phenomenon of an increase of resistance to crack propagation and indicates to the presence of dissipative processes, which accompany crack growth (microcracking). Fig. 3.3.41 also shows that with an increase of $MoSi_2$ volume content in the ZrB_2-$MoSi_2$ composites their fracture toughness increased (2 - 3.4 MPa m$^{1/2}$).
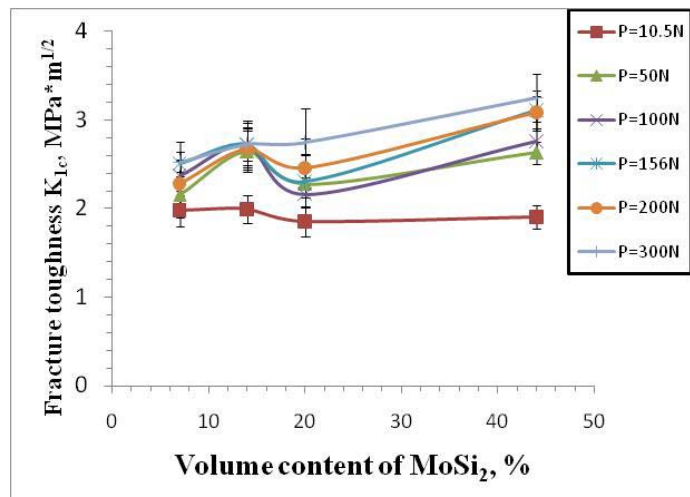
Fig. 3.41. Fracture toughness of ceramic materials of the ZrB_2-$MoSi_2$ system in dependence on the $MoSi_2$ content and load to indenter.

On the basis of hardness measurements as well as measurements of length of cracks formed near the hardness imprints we drew up the statistic distribution for the contact strength of ZrB_2-$MoSi_2$ composites (Fig. 3.42). In the majority of cases, the obtained distribution proved to be bimodal ones, i.e. they contain, as a rule, two straight line regions which may be related to two cracks populations – "long" and short" ones.

Weibull module m determined for the long cracks is varied from 16 to 20. Comparatively high Weibull module indicates to a heightened homogeneity or heightened relaxation capacity of the ceramic. With an increase of the load the number of long cracks increases whereas the shift of distribution to the left testifies to the decrease of contact strength characteristics. The separate Weibull analysis of long cracks population shows a sharply expressed scale effect of contact strength (Fig. 3.43).

Fig. 3.44 shows that with the load increase contact strength sharply decreases and has a minimum at maximum load 300 N. Generally, ZrB_2-$MoSi_2$ composites are characterized by a higher level of contact strength than ZrB_2-SiC ones. The introduction of $MoSi_2$ to the composition significantly heightens their contact strength (Fig. 3.44).

Testing of ZrB_2-$MoSi_2$ composite samples in the three-point bending showed that the introduction of insignificant amount of second phase essentially heightened their strength (530-580 MPa); the maximum strengths is realized at 44.0 vol. % $MoSi_2$ content (Fig. 3.45).
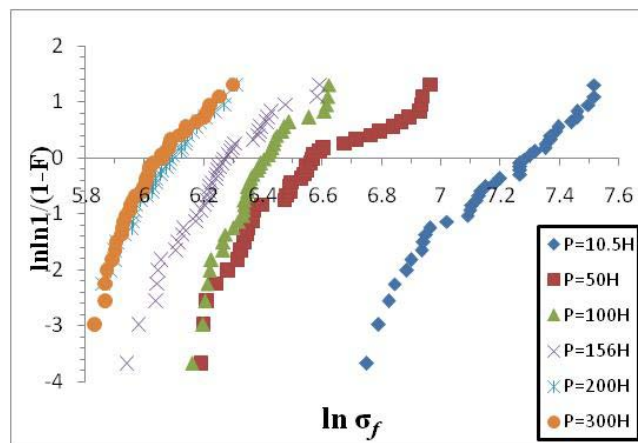
Fig. 3.42. Statistical Weibull distribution for contact strength of ZrB_2-7 vol. % $MoSi_2$ composites.
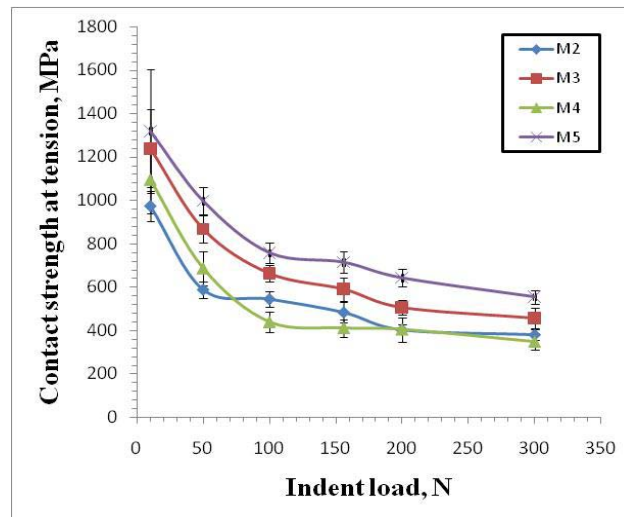
Fig. 3.43. Dependence of ZrB_2-$MoSi_2$ ceramic materials contact strength on indenter load.
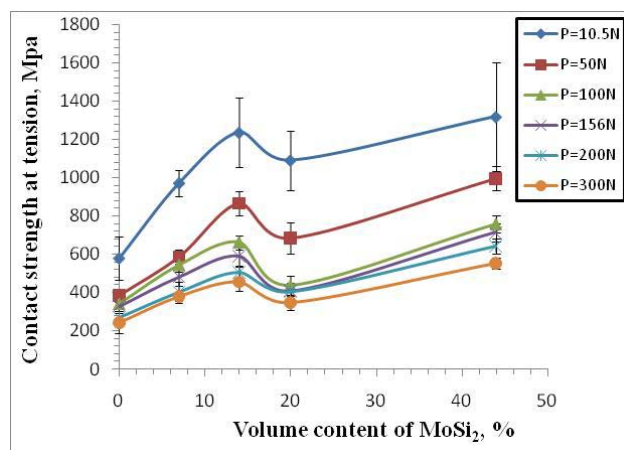
Fig. 3.44. Contact strengths of ZrB_2-$MoSi_2$ ceramics in dependence on $MoSi_2$ content.
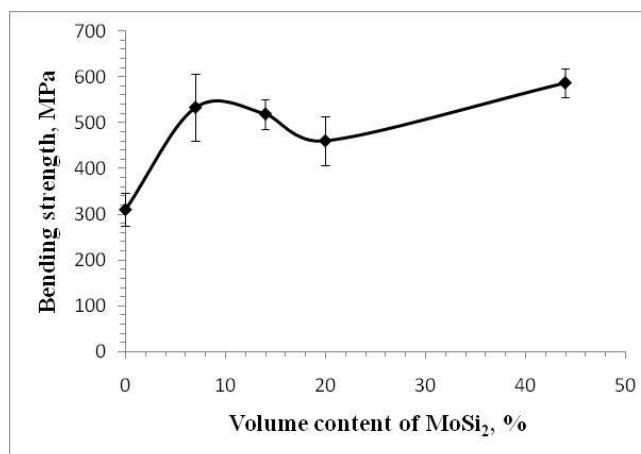
Fig. 3.45. Bending strengths of hot-pressed ZrB_2-$MoSi_2$ materials in dependence on $MoSi_2$ volume content.

3.3.2. High-temperature properties.

Bending strength measurements were carried out using 3- and 4-point testing scheme on the base of 40 and 40/20 mm, correspondingly. The typical testing results at room temperatures compared with the measurements at 1400 °C are presented in Fig. 3.46.

a)   b)
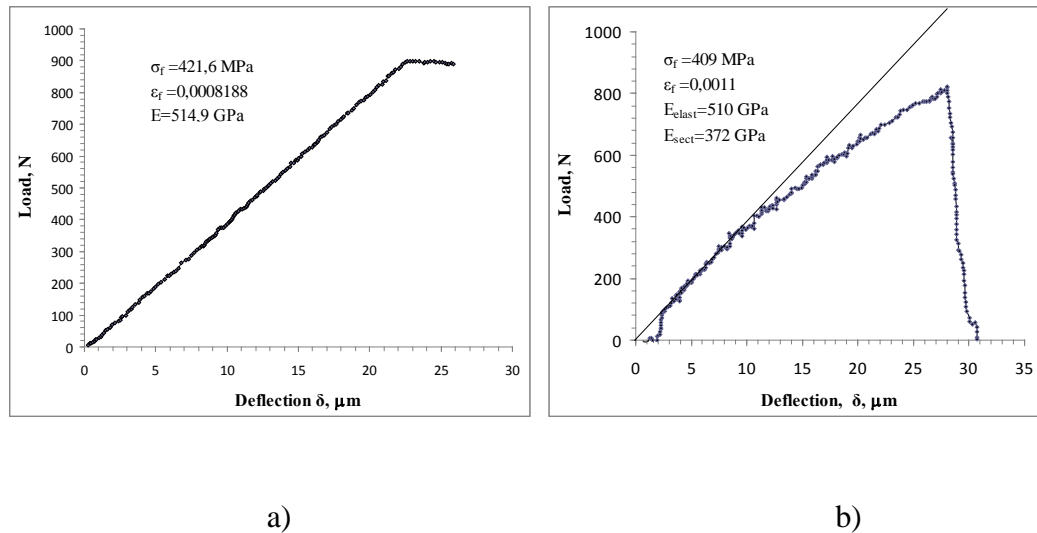
Fig. 3.46. Stress-strain diagrams for the US2 samples at RT (a) и 1400 °C (b).

It is well known that the reduction of grain size is accompanied by strength increase at room temperature. However, at high temperatures the decrease of grain size usually leads to the increase of both creep and high-temperature oxidation rate. That is why in this work the powders where used which, resulting from a sintering, gave a possibility to obtain ceramics with the grain size ~ 10 μm that was very important for an assurance of basic level of properties in the wide temperature range (20-1500 °C).

Fig. 3.46 shows that the stress-strain curve of US2 ceramics at room temperature is practically linear; Young module at room temperature is equal to 515 GPa (with the accuracy of ~ 2%), bending strength is equal to 420 MPa (4-point bending with a base of 40/20 mm). At 1400 °C significant nonlinearity of deformation diagram takes place. The proposed technology of ceramics manufacturing allows presence of some amount of oxygen (up to 1 mass %) in the form of oxides located at the grain boundaries. Usually, amorphous layers at the grain boundaries are responsible for the grain boundary creep of the composite and nonlinearity of the deformation diagram at high temperatures. Young module on the linear part of the deformation diagram is high (510 GPa), the effective module being equal to 326 GPa. Bending strength of the ceramics at 1400 °C compared to that at room temperature remains almost constant (410 MPa). Thus, US2

ceramics, which is regarded as a base material, has satisfactory bending strength and mechanic stability in the wide temperature range. Temperature dependencies of bending strength for some US and USS ceramics are presented in Fig. 3.47.
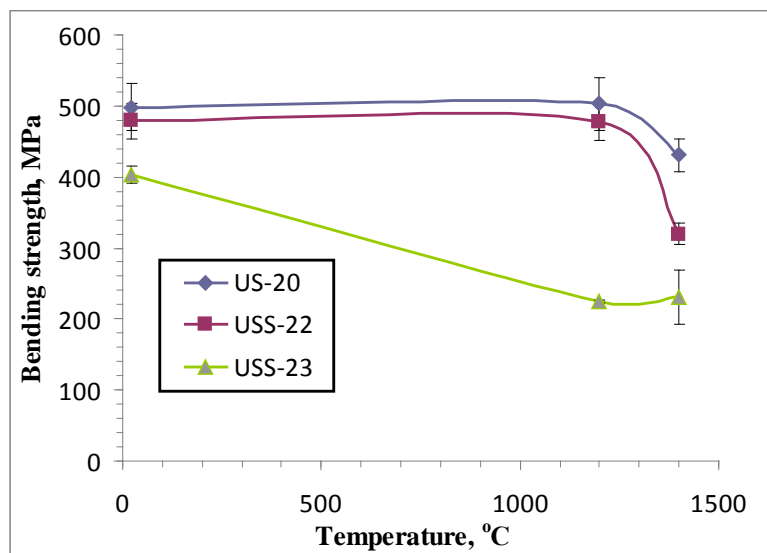
Fig. 3.47. Temperature dependence of bending strength for US and USS ceramics.

Compositions: US-20 – 81.4 vol.% ZrB_2+18.6 vol.% SiC

USS-22 - 78 vol.% ZrB_2+17.6 vol.% SiC+4.2 vol.% $ZrSi_2$

USS-23 - 75.4 vol.% ZrB_2+17.2 vol.% SiC+7.4 vol.% $ZrSi_2$

High-temperature measurements of strength showed that beginning from 1000 °C essential lowering of strength took place for ZrB_2-SiC-$ZrSi_2$ samples with high content of $ZrSi_2$ (Fig. 3.48). Testing has been carried out for the sample series of the following composition:

USS-32 – 75 vol. % (97 vol. % ZrB_2+3 vol. % $ZrSi_2$) +25 vol. % SiC

USS-43 - 52 vol. % (84.5vol. % ZrB_2+15.5 vol. % $ZrSi_2$) +48 vol. % SiC

USS-72 - 33vol. % (88 vol. % ZrB_2+12vol. % $ZrSi_2$) +66.7 vol. % SiC
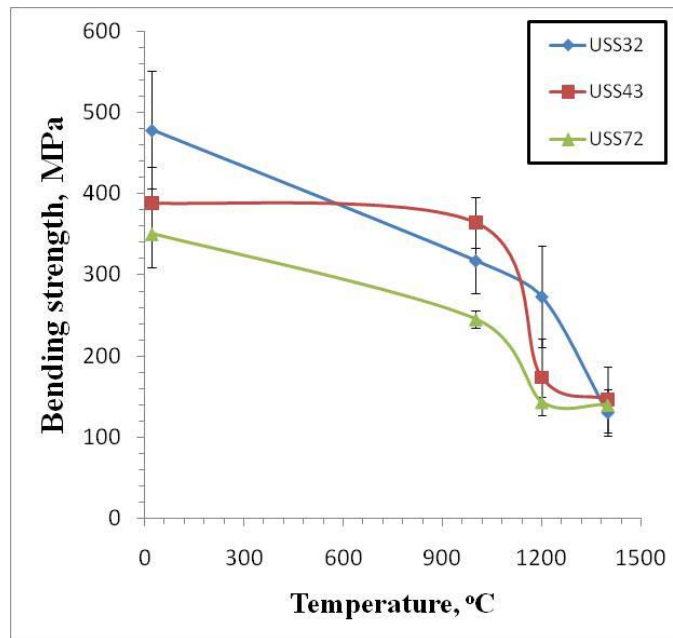
Fig. 3.48. Bending strength of ZrB_2-SiC-$ZrSi_2$ composites in dependence on testing temperature.

ZrB_2–20 vol.% $MoSi_2$ ceramics.

High-temperature measurements of ZrB_2–20 vol.% $MoSi_2$ strengths showed that beginning from the temperature of 1000 °C practically full strengths degradation took place (Fig. 3.49). These results are in a good correlation with the data of other researchers and are mainly caused by the heightened plasticity of molybdenum silicide.
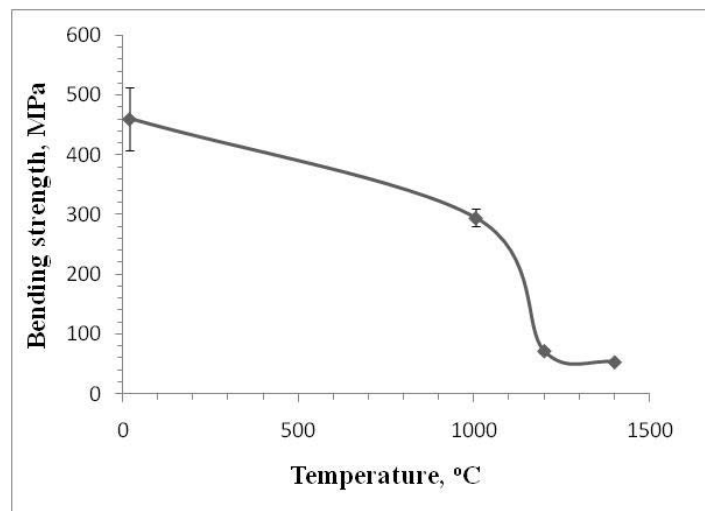
Fig. 3.49. Strength of ZrB_2 -20 vol.% $MoSi_2$ composite in dependence on testing temperature.

As one can see from the figures, incorporation of $ZrSi_2$ into the composite along with the substitution of silicon carbide for $MoSi_2$ leads to an essential softening of the ceramics above 1000 °C. The softening of the composites with $ZrSi_2$ additives due to formation of an amorphous grain-boundary phase with insufficient viscosity at high temperatures is connected with a grain-boundary amorphous phase with a deficit of viscosity at high temperatures, the latter being connected with its formation on the account of interaction of zirconium silicide melt with zirconium boride and silicon carbide. The softening of the ZrB_2-$MoSi_2$ ceramics above 1000 °C was also reported by Barton. The strength lossof the ceramics of ZrB_2-$MoSi_2$ system might be a consequence of interaction between oxidation products as well as enhanced high-temperature ductility of $MoSi_2$.

The results of strength measurements for USS-22+ 2 vol.% TaB_2 and USS-22+ 2 vol.% YB_6 systems at the temperature of 1400 °C (Fig. 3.50) showed that the introductionof TaB_2 and YB_6 additives to the ceramics composition (in order to improve their high-temperature characteristics) had little effect. However, such result may be caused by high residual porosity of the samples (Table 2.8).
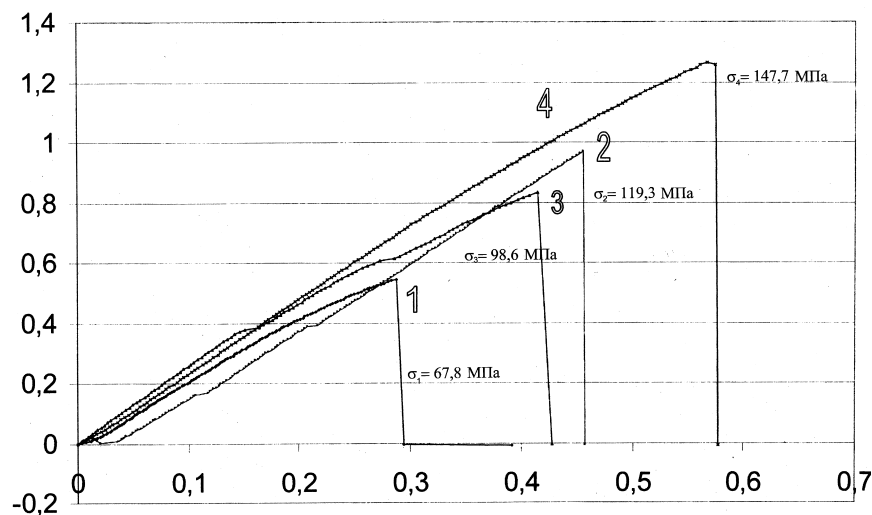
Fig. 3.50. Diagram of USS-22+ 2 vol.% TaB_2 (3,4) and USS-22+ 2 vol.% YB_6 (1,2) samples deformation at 1400 °C.

SiC - ZrB_2 - B_4C System.

For the investigations of mechanical properties in a wide temperature range the samples with zirconium diboride content 5-20 vol.%, and boron carbide ~10 vol.% were selected. SiC - ZrB_2 - B_4C ceramics did not show strength degradation in the range of testing temperatures (Fig.

3.51). Perhaps, it can be associated with higher oxidation resistance of these ceramics and differences in the composition of grain boundary phases.
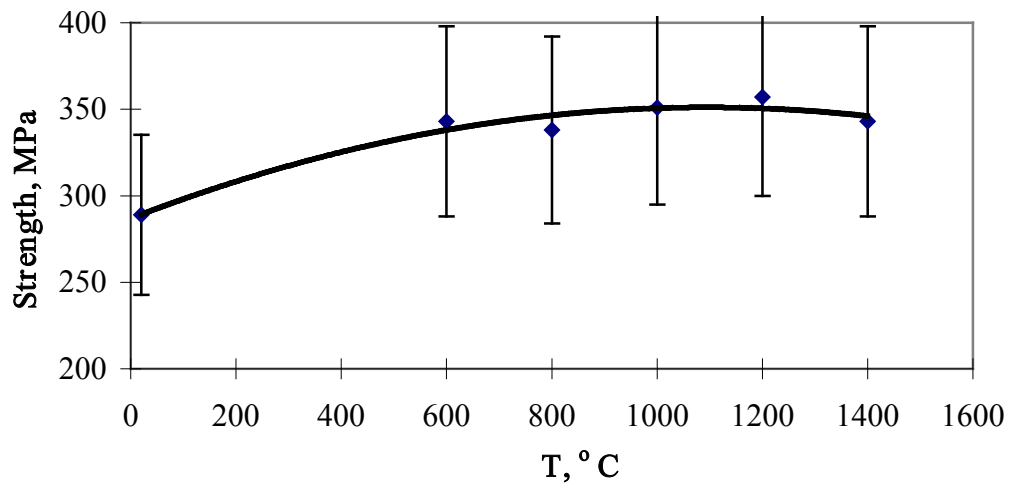
Fig.3.51. Temperature dependence of bending strength
for SiC - 10 vol. % ZrB_2 (10 vol. % B_4C) ceramics.

3.4. Characteristics of oxidation processes in ceramic systems under study.

Our preliminary investigations showed essentially higher oxidation resistance of SiC-ZrB_2 ceramics compared with SiC-TiB_2 ones (Fig. 3.52).
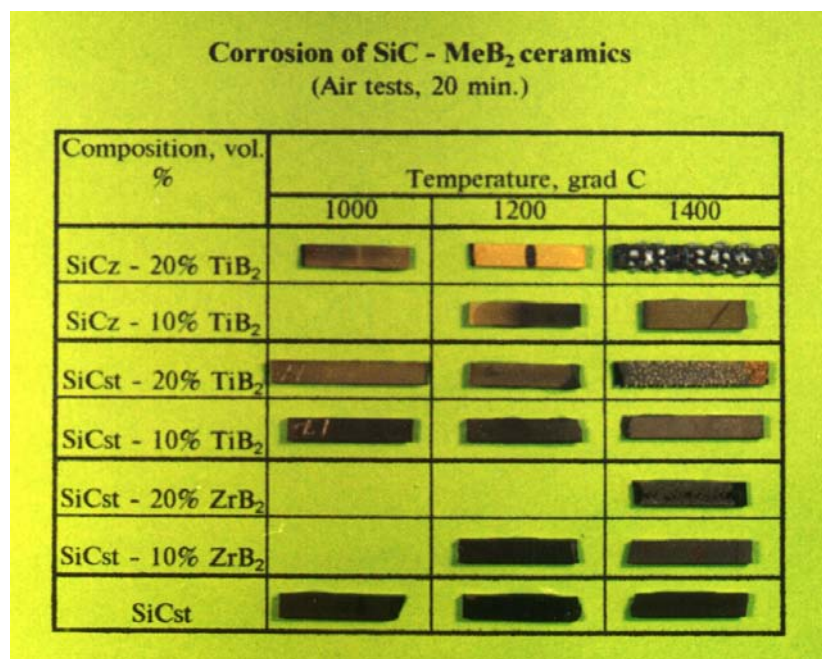
Fig. 3.52. Samples of ceramics after oxidation, SiCz and SiCst – silicon carbide from different
manufacturers.

For the research and description of high temperature oxidation processes of composite ceramic materials of ZrB_2 - SiC and ZrB_2-SiC-Zr(Mo)Si_2 systems up to high (~1300 °C) and

ultrahigh (~1650 °C) temperatures, the analysis of these processes was carried out within the framework of the well known Wagner's theory, which is widely used and leads to a parabolic dependence of the sample mass gain on time at fixed temperature. Also, an experimental modeling of the process of their preliminary moderate electrochemical (anode) oxidation with formation of protective oxide nanofilm within the framework of Mott-Cabrera theory is conducted on the example of one of the components of the triple ceramic system, namely, $MoSi_2$, which is as individual phase the most resistant to high-temperature oxidation. The ultimate goal of this approach is a design of models for ceramic corrosion-resistant structures.

Considering the literature data and our own previous information on oxidation kinetics and mechanism for individual phases of ZrB_2-SiC-$Zr(Mo)Si_2$ ceramics, first of all, it has been found out that all the phases of this ultrahigh-temperature ceramics are characterized by relatively high oxidation resistance.

High corrosion resistance inherent to the silicon carbide is determined by the formation of protective SiO_2 film that is capable of self-healing in the case if any defects form in it (pores, cracks and others like that). Up to 1200 °C the rate of SiC interaction with oxygen in air is extremely low, while at 1400 °C SiO_2 formation intensifies to a great extent (T_m = 1500 - 1600 °C). Melting at this temperature, silicon dioxide as an amorphous silica or α − cristobalite covers the carbide particles which to a great extent prevents it from subsequent oxidation, especially due to formation of cristobalite. The character of oxidation isotherms for SiC transformation to SiO_2 fits parabolic dependence on time which coincides with the conclusions of Wagner's theory in relation to oxide layer formation of moderate thickness or thick enough scale layers.

The zirconium diboride oxidation up to1200 °C results in formation of two-phase oxide film which contains monoclinic ZrO_2 and B_2O_3. Low melting temperature, high pressure of the saturated vapor and ability of B_2O_3 to form glassy phases with relatively high viscosity provide high enough heat-tolerance at moderate temperatures only then when B_2O_3 evaporation rate is low. Consequently, in order to increase the corrosion resistance it is necessary to introduce to the composition other components, mainly, SiC and d-metals disilicides. Being near to some of them in a structural type, zirconium diboride must form with them solid solutions. Above all, it applies to $MoSi_2$, $ZrSi_2$, and WSi_2.

The oxidation mechanism of individual d-metals disilicides was established up to 1800 °C. In the case of $ZrSi_2$, two oxides appear on the sample surface - ZrO_2 and glassy SiO_2; the latter (amorphous) phase having low conductivity and high adhesion to the substrate.

Process of $MoSi_2$ high-temperature oxidation takes place in two stages: the first one is formation of MoO_3 and cristobalite (SiO_2) at temperatures lower than the evaporation temperature of MoO_3 (791 °C); the second one being formation of lower Mo_5Si_3 silicide and SiO_2 amorphous film at higher temperatures. The limiting stage of interaction is diffusion of oxygen atoms towards the scale/silicide interface.

If the oxidation of $ZrSi_2$ is concerned, then according to literature information, up to 1300 °C main oxidation products are monoclinic ZrO_2 and SiO_2 while above 1300 °C - cubic ZrO_2 as well as (at ~ 1400 °C) $ZrSiO_4$ (zircon) zirconium orthosilicate that functions as protective barrier against a subsequent material oxidation up to the temperature of 1700 °C.

At elevated temperature one may expect formation on these ceramics of corrosion resistant (SiO_2-B_2O_3) glassy film with fine grains of ZrO_2 and $ZrSiO_4$ sprinkled in it. Obviously, it will be able to provide protection from high-temperature corrosion also for more complex materials, in particular, ceramics of the ZrB_2-SiC-$ZrSi_2$ system being studied by us. It is possible to hope that the glassy borosilicate film (SiO_2-B_2O_3) on a boride-silicide composite material undergoes recrystallization as well as self-healing. As a result of it the film should become continuous and dense (it is the research subject within the framework of our Project). We also hope that amorphous character of phases which will appear in the composition of the scale at high and ultrahigh temperatures will be able to provide protective properties of the more complex ceramic composites.

It should be noted that introduction of silicon carbide into the composition of ZrB_2 - SiC material (to 30% at.) improves to a great extent not only mechanical properties but also increases resistance to high-temperature oxidation. This process is characterized by two stages. The first one – at 1200 °C when zirconium diboride oxidation follows with formation of ZrO_2 and liquid boria, and at higher temperatures (to 1600 °°C) when the active silicon carbide oxidation begins with formation of SiO_2 which hinders B_2O_3 evaporation binding it in boron-silicate glass. The similar picture is observed also in the HfB_2-SiC system. Thus, the protective oxide film in the ZrB_2 - SiC system consists of boron-silicate glass, mainly, in the higher layers of the scale whereas ZrO_2 and $ZrSiO_4$ impregnations are located in boron-silicate glass in the layer nearer to intact substrate.

Thus, it is possible to hope that, using more complex composite ceramics of the ZrB_2-SiC-$Zr(Mo)Si_2$ system in the corresponding branches of industry, one can provide the substantial improvement of not only its mechanical properties, but also corrosion resistance in air at ultrahigh temperatures.

Since zirconium boride is used as a refractory material with high mechanical properties and it is introduced into the composition of composite ceramics working at high temperatures in oxidizing media, the necessity to increase its oxidation resistance becomes critical. As the second component zirconium disilicide $ZrSi_2$ is proposed, it can form with ZrB_2 solid solutions.

The preliminary study was performed on sintered materials. The manufacturing regimes of ZrB_2 - based materials with $(1 – 50$ mass.% $)$ $ZrSi_2$ were developed. These materials were sintered in vacuum at 1650-1750 °C; their porosity was in the range of 8-10 %. The composites of ZrB_2 - $ZrSi_2$ system were studied with the aid of XRD method. At high $ZrSi_2$ content the heterogeneous structure is observed: ZrB_2, zirconium silicide $ZrSi$, and, obviously, ZrB phase.

Under conditions of $ZrB_2 – 1\%$ $ZrSi_2$ oxidation at 700 -800 °C and oxygen pressure of 10.13 kPa the significant mass gain is observed (approximately 10.10^{-2} kg/m^2); the oxidation rate obeys the parabolic rate law.

The petrographic analysis of the formed oxide film shows the presence in it of hydrated B_2O_3 and single small (less than 1 μm) anisotropic grains of ZrO_2. Boric anhydride promotes partial healing of a scale and further oxidation of the material. However, at the increase of temperature up to 1200 °C material is subjected to intensive oxidation – mass gain considerably increases (up to 15.10^{-2} kg/m^2). In this case the oxidation rate obeys a linear law. According to the data of petrographic and XRD analyses, the oxide film, mainly, contains zirconium dioxide ZrO_2 with the refraction indexes of $n_p = 2.12$ and $n_q = 2.15$ that corresponds to monoclinic modification of this oxide.

In the process of oxidation of ZrB_2-5 % $ZrSi_2$ at 700 °C for 3 hours, the mass gain of 5.10^{-2} kg/m^2 is observed, at 800 °C – $2.5.10^{-2}$ kg/m^2; oxide film contains boric anhydride and small ZrO_2 grains. At the temperatures of 1000-1200 °C mass gain due to oxidation diminishes even more and becomes equal to $(1.5 – 2).10^{-2}$ kg/m^2; the rate law in this case remains parabolic one. In a scale the phases of SiO_2 and ZrO_2 oxides are detected as well as zirconium silicate $ZrSiO_4$.

Consequently, at the temperatures higher than 1000-1100 °C, B_2O_3 oxide is removed into gaseous phase, while ZrO_2 and SiO_2 oxides as a result of interaction form $ZrSiO_4$ silicate phase with very tight cohesion to the substrate. It is this phase that determines protective properties of the oxide scale.

If initial sample contains 15 % $ZrSi_2$, it is characterized by yet higher resistance to oxidation. In this case at oxidation at 1200 °C for 3 hours, the mass gain of sample is equal to $2.2.10^{-2}$ kg/m^2; protective film appears on its surface, which is very tightly bonded to the substrate. By means of petrographic and XRD analyses the $ZrSiO_4$ zirconium orthosilicate was identified in

the scale formed; this phase, similar to the previous case, also protects ceramic sample from subsequent oxidation.

Oxidation of ZrB_2-50 % $ZrSi_2$ in the oxygen atmosphere at 700-900 °C is insignificant; the mass gain is less than 1. 10^{-2} kg/m^2. With the aid of petrographic analysis it was established that in the very thin layer of the scale there are the ultrafine (less than 1μm) ZrO_2 grains, sprinkled in a glassy (SiO_2 - B_2O_3) film. At 1000 °C the change of sample mass during 3 hours oxidation becomes less than 1.6. 10^{-2} kg/m^2. The scale, that is formed, consists of $ZrSiO_4$ fine-grained phase (sizes of grain are less than 1 μm) with the insignificant inclusions of B_2O_3. With the increase of temperature up to 1200 °C the character of ceramics oxidation for this composition also remains parabolic one, and almost dense film, firmly cohesively bonded to the substrate, mainly contains $ZrSiO_4$ phase. Its reflection coefficients are equal to n_p = 1. 911, n_q = 1.950; the sizes of film grains are in the range from 1-2 to 5-7 μm.

The corresponding oxidation kinetics data are presented in Fig. 3.53.
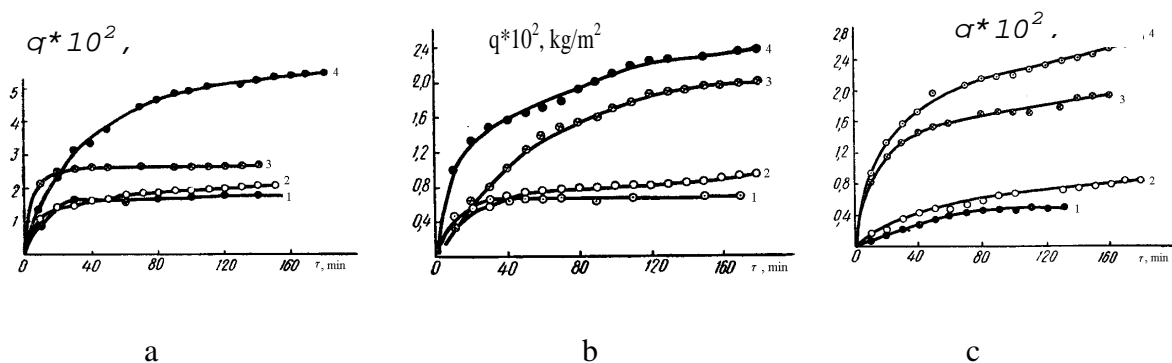
a   b   c

Fig.3.53. Oxidation kinetics of ZrB_2-5% $ZrZi_2$ (a), ZrB_2-15% $ZrSi_2$ (b) and ZrB_2-50% $ZrSi_2$ (c) ceramics in oxygen; T, °C: a) 1-1000, 2-1100, 3-800; b) 1-700, 2-900, 3-1100, 4-1200; c)1-600, 2-850, 3-1000, 4-1200.

With the increase of temperature up to 1200 °C and higher, the thin glassy film on the 50%ZrB_2-50%$ZrSi_2$ samples is recrystallized, it becomes dense and continuous. Such oxide film can serve as a reliable protective barrier in relation to the further oxidation of composite material at higher temperatures. It is possible to hope that the double 50% ZrB_2-50 % $ZrSi_2$ composition resistance to oxidation in both oxygen and air environment may be promising in the row of advanced high-temperature materials, at least for short-term using.

The experiments on kinetics of high-temperature oxidation in pure oxygen of ZrB_2-SiC and ZrB_2-SiC-$ZrSi_2$ composites were carried out in the Laboratory of Prof. Klaus Nickel in Tuebingen

University, Germany. On the basis of weighing data obtained we built the oxidation isotherms for ZrB_2-SiC and ZrB_2-SiC-$ZrSi_2$ samples (Fig. 3.54). On the whole, these oxidation isotherms were characterized by almost parabolic rate law (especially for the second system) due to the process of diffusion control in the dense oxide film formed.
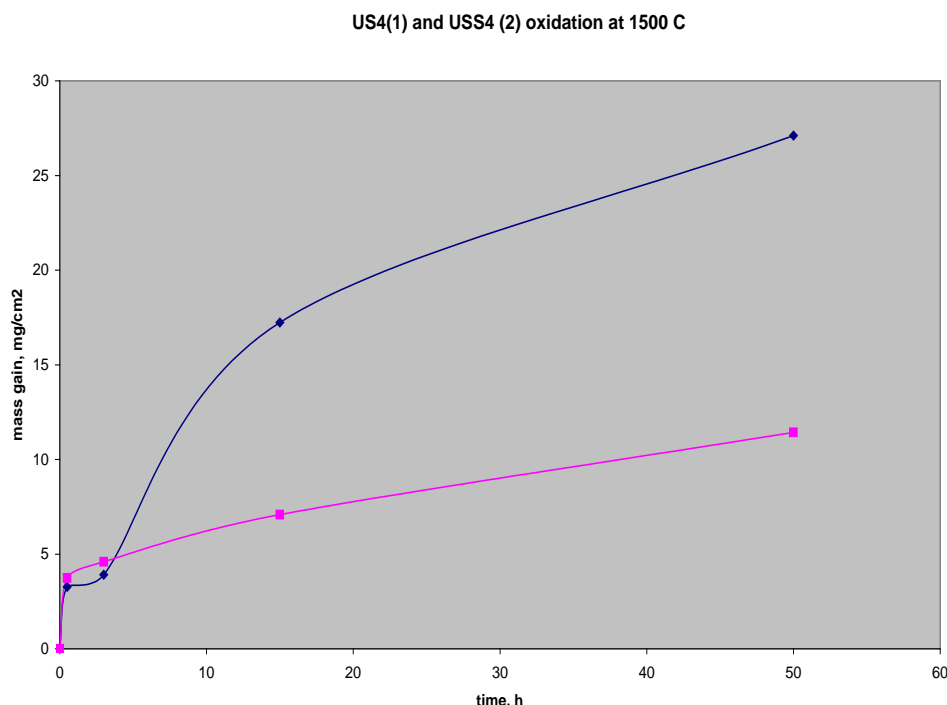
US4(1) and USS4 (2) oxidation at 1500 C

Fig.3.54. Curves of isothermal oxidation of US4 (dark blue curve) and USS4 (magenta curve) samples at 1500 °C.

It is completely obvious that the addition of $ZrSi_2$ to the composition of $ZrSi_2$-SiC ceramics leads to the significant rise of their corrosion resistance. One can see a sharp difference between two experimental curves in Fig.3.54. In the case of US4 sample, the mass gain curve consists of two different regions. We may suppose that in the first period of time the SiO_2 – containing film is formed, which is at this stage (up to 3 h) characterized by protective properties. However, further scale loses its protective properties, and in the second oxidation stage the significant mass gain of sample takes place. Then, at this stage the quasi-parabolic kinetics establishes.

As a result of oxidation on the surfaces of all samples the two-three layer oxide film was formed. In the outer layer there is a borosilicate glass, below which there is the inner layer, which

contains glass with fine grains of zirconium oxide (Fig. 3.55). Because ZrO_2 has a relatively large coefficient of thermal expansion, tangential cracks are formed around its grains, but they are healed by glass during the consequent thermal cycle.
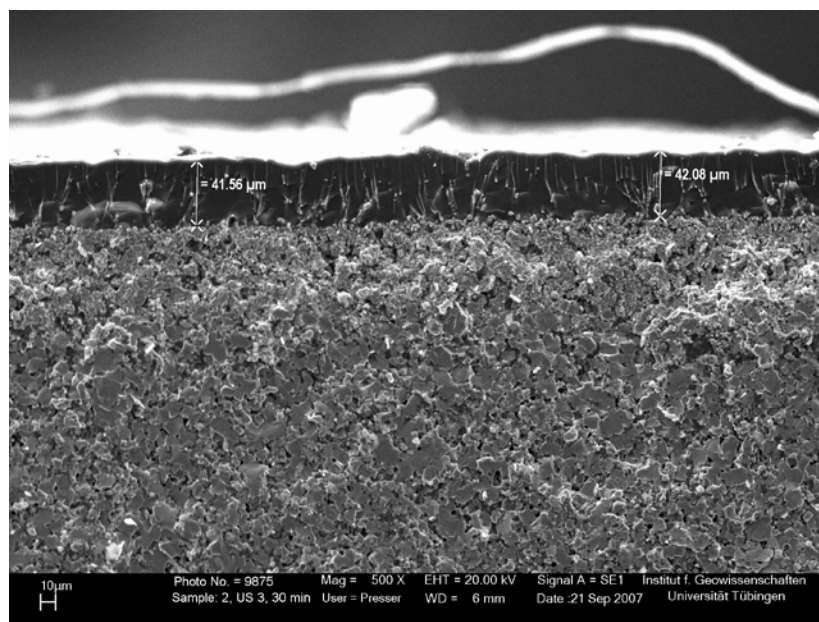
Fig. 3.55. SEM microphoto of cross section of oxidized US3 sample surface after 30 min oxidation at 1500 °C. Oxide film has two-layers.

In the case of ZrB_2-SiC-$ZrSi_2$ ceramics oxidation (magenta curve) one can see, obviously, one type of oxidation behavior, but for the first 3 h an abnormal high oxidation rate occurs. Later, during formation of stable dense oxide layers, oxidation rate became significantly lesser than in the case of two-component system. In our opinion, it may be partially explained by formation in the scale of not only ZrO_2 and borosilicate glass but also $ZrSiO_4$, which was confirmed by XRD analysis.

The XRD study of US- and USS- samples after their oxidation did not show the qualitative differences of their phases compositions (Fig. 3.56; 3.57). For both ZrB_2-SiC-$ZrSi_2$ and ZrB_2-SiC systems in the oxidized surface layer of all samples were found the following components: amorphous phase (borosilicate glass) as well as the crystal phases of boron and silicon oxides, zirconium oxide (baddeleyte structure) as well as $ZrSiO_4$ zircon. Thus, beside usually mentioned phases in the structure of oxidized layers – borosilicate glass and zirconium oxide, also zircon, crystal boron, and silicon oxides were observed additionally. Therefore, the differences in the

oxidation kinetics of various ceramic systems of the studied type we have to seek in the quantitative differences of phase compositions and the structure of surface scale layers.
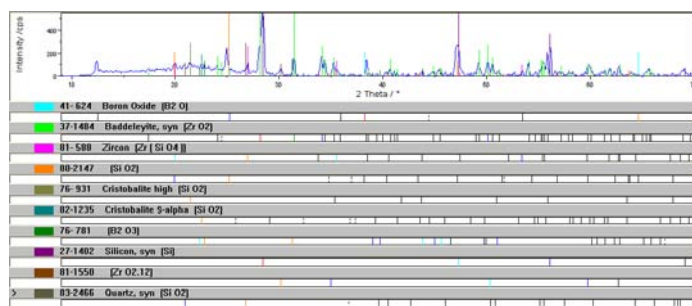
PDF-No	In Range	Matched	FOM	SOM	Name Min.	Formula
81- 588	20	20	0.509	4.231	Zircon	$Zr(SiO_4)$
83-2466	18	17	0.572	4.654	Quartz, syn	SiO_2
37-1484	45	44	0.684	3.003	Baddeleyite, syn	ZrO_2
27-1402	4	4	0.732	8.761	Silicon, syn	Si
82-1235	29	25	0.773	4.345	Cristobalite $-alpha	SiO_2
76- 931	8	8	1.121	6.195	Cristobalite high	SiO_2
76- 781	21	20	1.356	4.006		B_2O_3
41- 624	7	6	1.459	6.622	Boron Oxide	B_2O
80-2147	18	15	1.855	5.127		SiO_2

Fig.3.56. XRD pattern of US4 ceramics after oxidation at 1500 °C, 50 h.
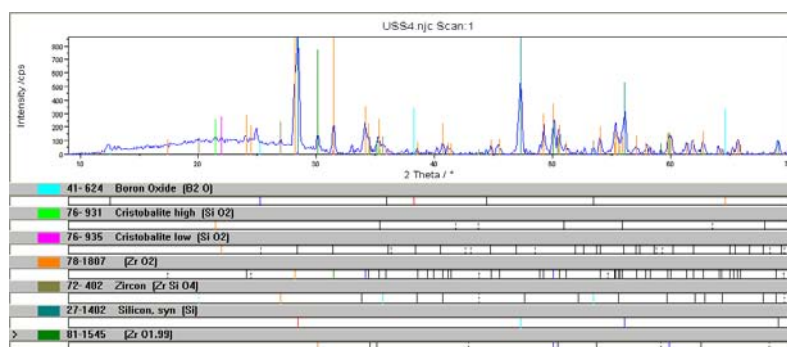
PDF-No	In Range	Matched	FOM	SOM	Name Min.	Formula
78-1807	46	41	0.375	2.353		ZrO_2
27-1402	4	4	0.413	6.124	Silicon, syn	Si
72- 402	18	15	0.509	3.636	Zircon	$ZrSiO_4$
76- 931	8	5	0.591	5.290	Cristobalite high	SiO_2
76- 935	32	23	0.611	2.939	Cristobalite low	SiO_2
41- 624	7	7	2.651	4.629	Boron Oxide	B_2O

Fig.3.57. XRD pattern of USS4 ceramics after oxidation at 1500 °C, 50 h.

Thus, the investigations carried out indicated that during long-time (50 h) oxidation of ZrB_2-SiC and ZrB_2-SiC-$ZrSi_2$ ceramics in the medium of pure oxygen the triple ZrB_2-SiC-$ZrSi_2$ ceramics (in particular, USS4 sample) showed by 2.7 times higher resistance to corrosion compared with the ZrB_2-SiC ones.

In all the cases after oxidation in oxygen we observed the following pattern of cross-section pictures (Fig. 3.58). Here the small upper layer 1 contained SiO_2 phase, while layer 2 – SiO_2 and Zr-rich phase; layer 3 was SiC depleted, and inner layer 4 contained unaltered ZrB_2-SiC material.
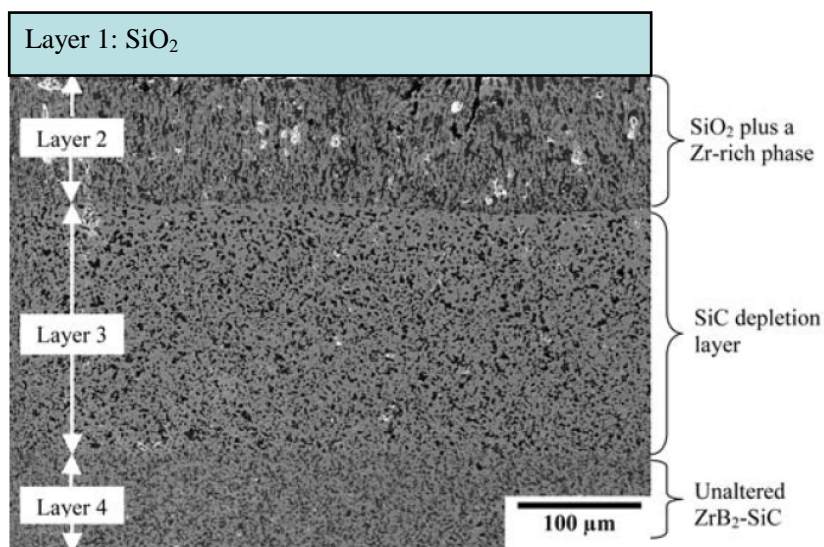
Fig. 3.58. Structure of oxidation scale according to Chamberlain (2005).

The typical structure of oxidized ZrB_2-SiC-$ZrSi_2$ samples is presented in Fig. 3.59-3.60, the mapping of O, Si, Zr and B elements distribution is shown in Fig. 3.60. Fig. 3.59 shows the typical pattern of 4-layers scale formed on the surface of sample oxidized in oxygen for 50 h: layer 1 – $SiO_2 \pm B_2O_3$; layer 2 - dense zirconia-zircon-silica; layer 3 – silica depleted, zirconia zone with graded increase of ZrB_2-grains; layer 4 is the unaltered ZrB_2-SiC matrix below.
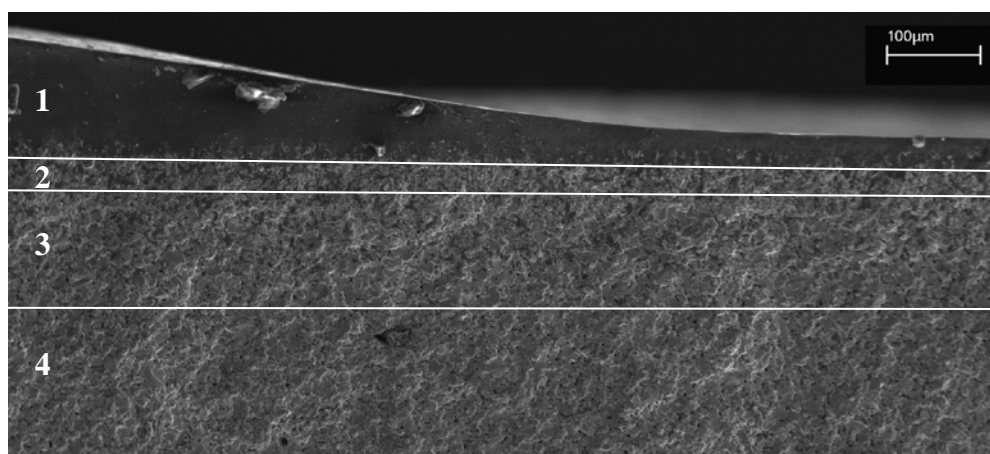
Layer 1: $SiO_2 \pm B_2O_3$

Layer 2: Dense zirconia-silica layer

Layer 3: Silica depleted, Zirconia zone with graded increase of ZrB_2 – grains

Layer 4: Unaltered ZrB_2-SiC matrix below

Fig. 3.59. Phase relations in the layers of oxide scale.
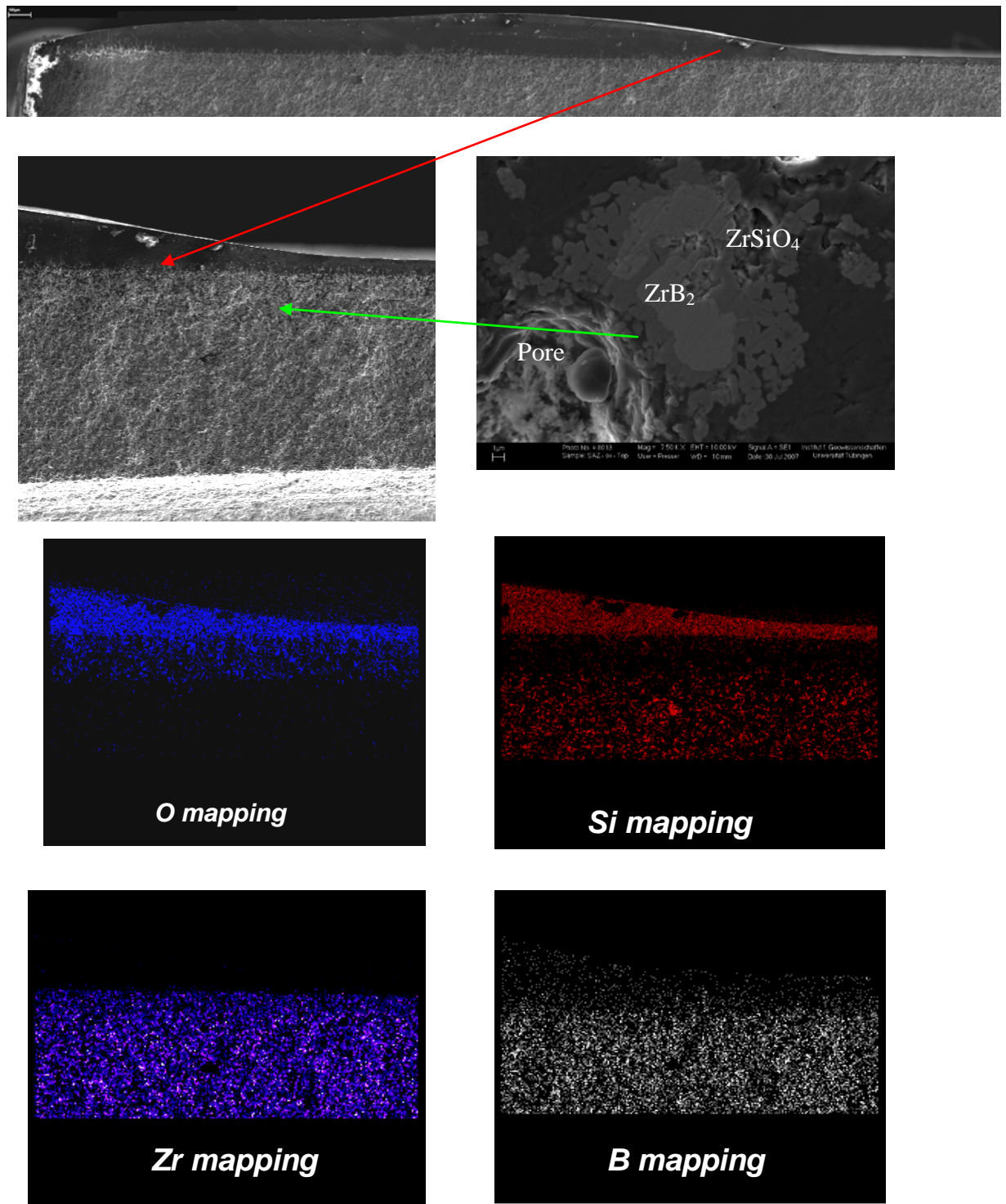
Fig. 3.60. Microphoto of typical oxidation scale and chemical elements mapping.

Oxidation resistance of samples oxidized in pure oxygen at 1500 °C was found to increase in the row USS46~USS43→USS41, i.e. comparable small co ntent of $ZrSi_2$ in the sample composition promoted the improvement of its corrosion properties. It is also visually shown in

Fig. 3.61. For example, for the USS41 sample the mass gain value for up to 24 h oxidation was equal to 9.7 mg/cm^2 whereas for USS46 – already 30.4 mg/cm^2.

USS41	USS43	USS46

Fig. 3.61. Top surface view of ZrB_2-SiC-$ZrSi_2$ ceramics after oxidation at 1500 °C for 35 h in pure oxygen.

The high-temperature oxidation resistance results were obtained for of SiC-ZrB_2 and SiC-ZrB_2-$ZrSi_2$ ceramics of different composition. In Fig. 3.62 we separately present the para-linear oxidation curves of long-term (~ 40 h) oxidation in oxygen at 1500 °C for triple ceramics samples with relatively small $ZrSi_2$ content (~ 2…7.6 wt.%) as well as linear dependence curve for such ceramics with its larger content (namely, 16.6 wt. %).
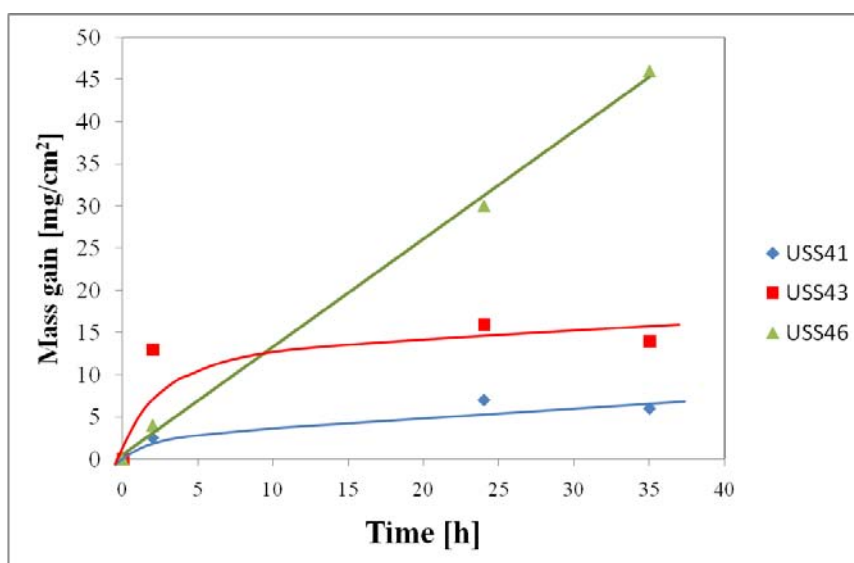
Fig. 3.62. Kinetic dependences of sample mass gain on oxidation time for SiC-ZrB_2-$ZrSi_2$ composites of different composition.

Thus, the increase of $ZrSi_2$ content led to the reduction of triple ceramics corrosion resistance. That is why for an optimal oxidation resistance we have to introduce into the double

ceramics only small amounts of third (silicide) component (Fig. 3.63). It is very important result, but it needs also an additional explanation.
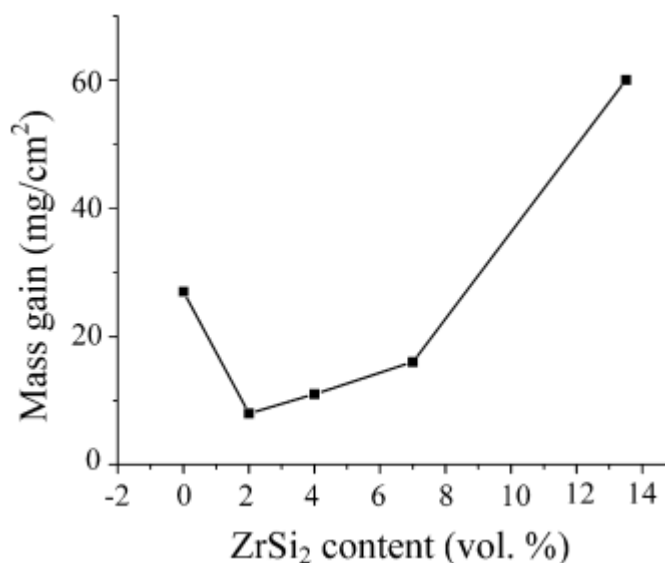
Fig. 3.63. Dependence of mass gain on $ZrSi_2$ content (vol.%) in charge for
oxidation at 1500 °C for 50 h in oxygen.

The US4 and USS41 samples have approximately the same grain size of components but slightly different porosity (5% and <1%, respectively). Therefore, the differences in oxidation rate could possibly be connected with differences of porosity and, in the final analysis, with the sintering activation effect on the account of the zirconium silicide additions. Besides, the Zr(Hf)C(B) phase is present in ZrB_2–SiC–$ZrSi_2$ ceramics (up to 3 vol.%) as solitary inclusions and does not form a continuous network. Thus, its presence alone should not influence oxidation rate significantly. It may be supposed that the reduction of oxidation rate of the triple system with small content of $ZrSi_2$ may be also (along with porosity effect) be connected with the inclusions and grain-boundary layers of residual amorphous Zr–Si–B phase that might form during $ZrSi_2$ decomposition under the scale of borosilicate glass. The interaction of oxygen with small amounts of amorphous phases may lead to the formation of additional protective SiO_2 and zircon phases. All these lead to the increase of ceramics oxidation resistance. With the increase of $ZrSi_2$ content to more than 8 vol.% larger amounts of an unstable amorphous phase are present along with porosity at the grain boundaries. These factors are likely responsible for a sharp rise in oxidation rate at a higher $ZrSi_2$ contents.

We showed the pictures of surfaces of SiC-ZrB_2-$ZrSi_2$ ceramics for the USS41, USS43 and USS46 samples after their oxidation at 1500 °C in pure oxygen during 50 h (Fig. 3.61). Now we carried out the investigation of top surface view for the USS41 ceramics which have been

oxidized for 3, 24, and 35 h with the measurements of corresponding mass gain values in mg/cm^2 (see Fig. 3.64).

One can see in Fig. 3.64 that in the first 3 h the sample surface is covered by thin oxide film, uniformly distributed, however, in the course of further oxidation for 20…30 h the surface already has separate pits, obviously, because of vaporization of some components in the oxide film.

Fig. 3.65 and, especially, Fig. 3.66 show that the increase of ZrSi$_2$ content in the initial triple ceramics leads to more intensive sample oxidation (under the same conditions).

However, even in this case one can also speak about comparatively acceptable corrosion resistance of optimum composition ceramics developed - in pure oxygen at high temperatures (~1500 °C). In fact, even admissible damage of sample (see Fig. 3.66) relates only to the surface part and not to deeper layers of these ceramics. The confirmation for such conclusion (concerning high corrosion resistance), especially, for the best compositions, may be the data obtained which demonstrate low mass gains of samples subjected to long-term (24 - 35 h and more) aggressive corrosion action. However, we must repeat that this conclusion relates only to the triple SiC-ZrB$_2$-ZrSi$_2$ ceramics of established optimum compositions (with a small amount of ZrSi$_2$ additive.

As a rule, after oxidation at 1500 °C we observed a plane, smooth laminated surface structures, the outer oxide layer being the most clean (see Fig. 3.67, and also Fig. 3.68).
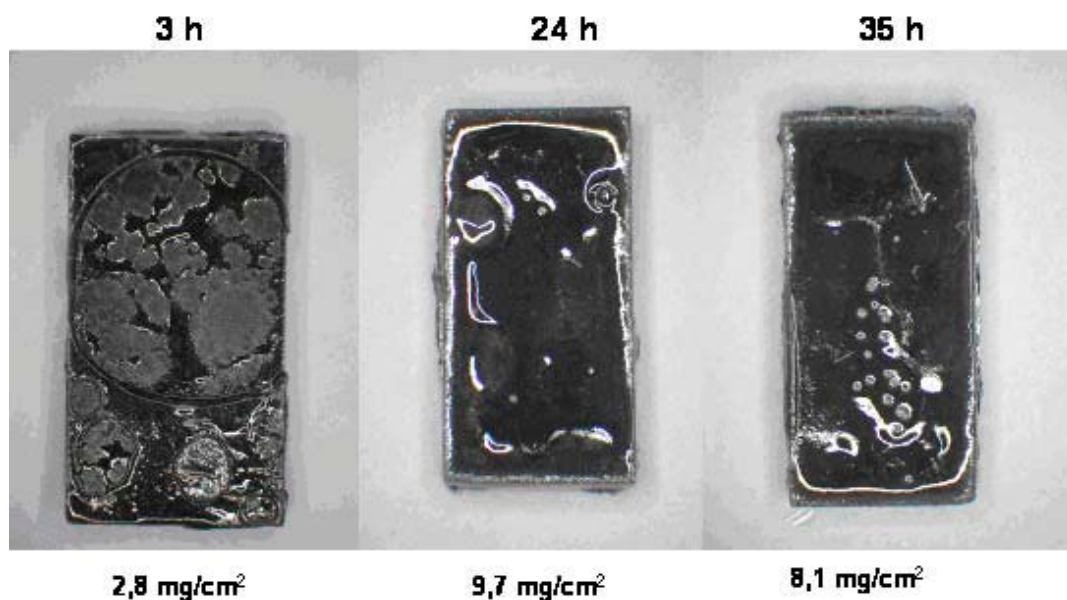
Fig. 3.64. Top surface view for USS 41 composite samples after oxidation.

Fig. 3.65. Top surface view for USS 43 composite samples after oxidation.
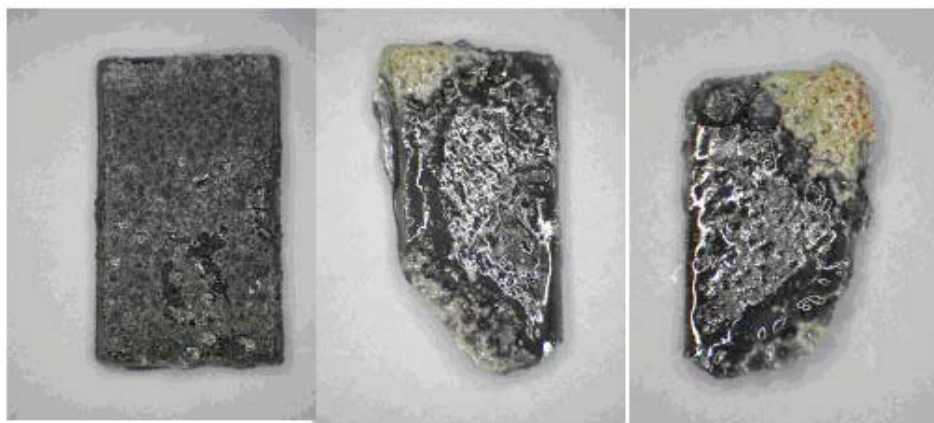
Fig. 3.66. Top surface view for USS 46 composite samples after oxidation.
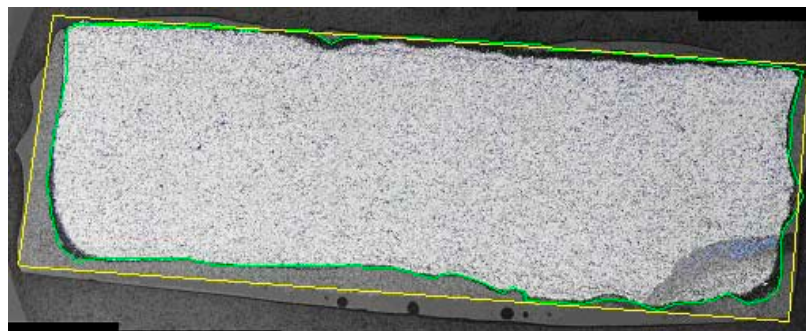
Fig. 3.67. The view of USS 43 ceramics sample after its oxidation in oxygen at 1500 °C for 24 h (from top to below): 1) pure SiO_2 scale, extremely variable; 2) zone, outlining original sample geometry with a mush of ZrO_2 in silica; 3) SiC-depleted porous zone with a high morphology; 4) unaltered material.

a)   b)
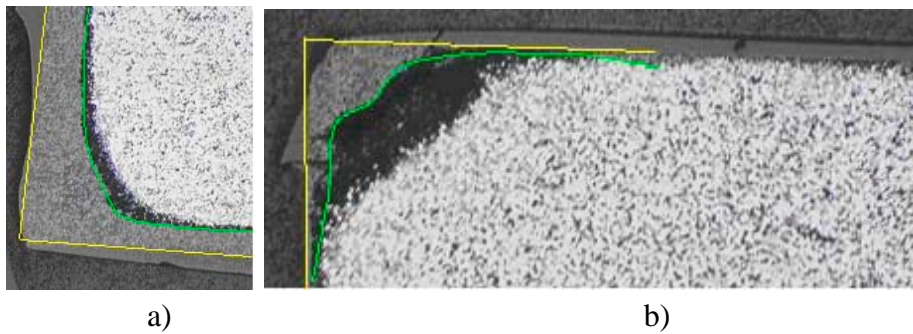
Fig. 3.68. The view of USS 43 (a) and USS 41 (b) ceramics sample, oxidized in oxygen at 1500 °C for 24 h.

The following reactions may be assumed to take place:

$$Zr(B,C) + n\ O_2 = n\ ZrO_2 + x\ B_2O_3 + y\ CO$$
$$ZrB_2 + 2.5\ O_2 = ZrO_2 + B_2O_3$$
$$SiC + 1.5\ O_2 = SiO_2 + CO.$$
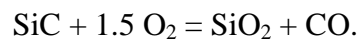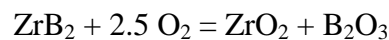
Borosilicate glass forms low viscosity melt, and oxygen penetrates to the sample surface. Low oxygen pressure and the comparatively high B_2O_3 and CO pressures promote the bubbles formation and some discontinuity of the scale.

The study of oxidation resistance – the effect of some oxides and salts.

We have studied the influence of some metal oxides and salt additives which can be present on the surface of ceramic samples under their high-temperature oxidation in oxygen at 1500 °C. These may be the components of fuel combustion products, small parts of engine as a result of its partial wear, namely Fe_2O_3, NiO oxide particles as well as the technological impurities which may be present at the surface on the account of ceramics manufacturing.

In these model tests we have put the appropriate amounts of Fe_2O_3, NiO, Al_2O_3 oxides and Na_2CO_3 on the ceramic sample surface (see Fig.3.69).
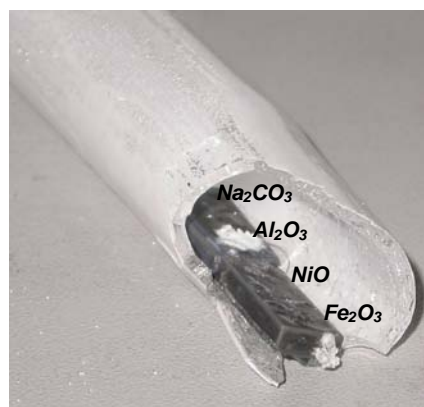
Fig.3.69. Impurity check (on USS41, 24 h., 1500 °C, O_2)

Fig. 3.70 and 3.71 show the respective picture of separate film formation (in particular, Al_2O_3), some spots and pitting (Fe_2O_3, NiO) after the long-term (24 h) oxidation of USS41 ceramics in oxygen at 1500 °C.
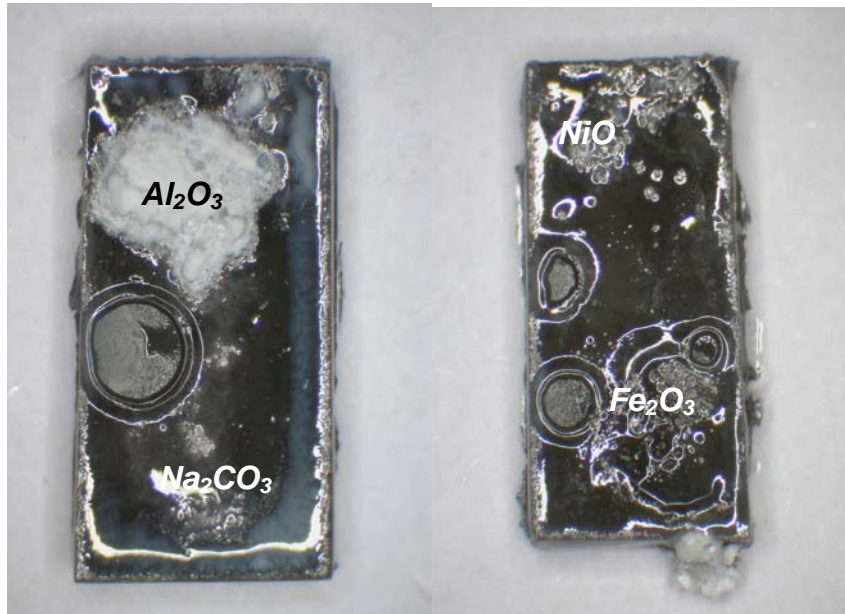
Fig. 3.70. The view of ceramics surface after oxidation in the oxygen flow in the presence of Fe_2O_3, NiO, Al_2O_3 oxides and Na_2CO_3.

Nevetheless, the Na_2CO_3 and NiO additives, in fact, have not practically affected the oxidation process of USS41 sample while the Al_2O_3 and Fe_2O_3 ones have had significant influence on the scale formation (Fig.3.71)

Fig.3.71. Effect of Fe_2O_3, NiO, Al_2O_3 and Na_2CO_3 additives on the high-temperature oxidation of USS41 ceramics (O_2, 1500 °C, 24 h.)

TG- and DTA-research of oxidation of ZrB$_2$-SiC and ZrB$_2$-SiC-ZrSi$_2$ ceramics in air at temperature up to 1600 °C.

In this study the kinetic peculiarities of high-temperature oxidation in air of 35 mas.% ZrB$_2$-65 mas.% SiC; 36.8 mas.% ZrB$_2$-60 mas.% SiC - 3.2 mas.% ZrSi$_2$ and 67.3 mas.% ZrB$_2$-26 mas.% SiC – 6.7 mas.% ZrSi$_2$ UHTCs have been studied.

The samples of high-temperature ceramics pointed out did not practically contain pores (the porosity was $\leq$ 1%). The experimental oxidation curves of a stage-by-stage sample specific mass gain (TG) and heat evolution (DTA) are presented in Fig.3.72 and 3.73 for the samples of different composition, respectively. The mechanisms of high-temperature oxidation of these samples in all the cases is discussed on the basis of kinetic data obtained, the literature information concerning the equilibrium in appropriate high-temperature oxide systems as well as results of XRD analysis of samples, oxidized in corresponding temperature ranges. In some cases for the identification of phase composition and morphology of the particles of interacting components, shaved out of upper surface layer of the formed scale, the petrographic analysis was applied using MIN-7 mineralogical microscope and a set of standard immersion liquids with the known values of refraction coefficients.

Oxidization of 35 mas.% ZrB$_2$ - 65 mas.% SiC ceramics.

For this sample (Fig. 3.72) at the first heating stage (from 100 to 560 °C) the relative mass loss $\Delta m/m_o$= - 0.24 % was recorded with the endothermal peak (458 °C) of earlier adsorbed oxygen desorption. It was established that the real oxidation begins at 560 °C and up to 900 °C is characterized by zirconium boride interaction with air oxygen according to the reaction

$$2\,ZrB_2 + 5\,O_2 = 2\,ZrO_2 \text{ (monocline.)} + 2\,B_2O_3 \qquad (3.1)$$
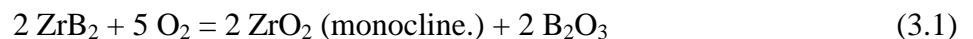
The temperature of exothermic peak of this stage is 685 °C while the value of relative mass gain is $\Delta m/m_o$ = 1.53 % at 817 °C.

For the second oxidation stage of these ceramics, at first, in the temperature range from 900 to 1180 °C, the interaction of SiC with oxygen takes place up to ~ 980 °C with the formation of α-SiO$_2$ crystobalite phase

$$2\,SiC + 3\,O_2 = 2\,SiO_2 + 2\,CO\uparrow, \qquad (3.2\ a)$$

and then the formation of two solid-phase interaction products was established: the same α-SiO$_2$ (crystobalite) and also ZrSiO$_4$ (zircon):

$$2\,SiC + ZrO_2 \text{ (monoclin.)} + 4\,O_2 = SiO_2 + ZrSiO_4 + 2\,CO_2 \qquad (3.2\ b)$$

In the common boride-carbide ceramics, at the thick enough glass film, the reaction

$$SiC + O_2 = SiO\uparrow + CO\uparrow \tag{3.2c}$$

is also observed. Below the glass a porous layer without silicon carbide is formed, the latter decreasing the ceramics oxidation resistance. However, in our case, without the gaseous SiO, this layer becames denser that, on the whole, increases the oxidation resistance.

The exothermic peak of reaction (3.2b) is observed at 950 °C; the mass gain value is 2.63 % at 1144 °C.

The following interaction stage on DTA-curve (Fig. 3.72) at the heating of sample from 1200 to 1480 °C fits to the formation of amorphous SiO_2 on its surface:

$$\alpha\text{-}SiO_2 \text{ cryst.} \rightarrow SiO_2 \text{ glass-like}, \tag{3.3}$$
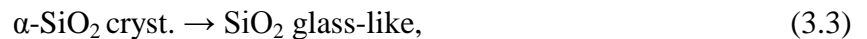
which is thermodynamically more stable phase at the temperatures ~ 1400 °C. In particular, in our case the exothermal peak of transition pointed out is found at 1356 °C.

And finally, as a result of heating of these ceramics up to 1700 °C the upper scale layer is formed on the sample surface. It is a film of borosilicate glass, i.e. solid solution of B_2O_3 in SiO_2, on the account of dissolution of boron oxide in amorphous SiO_2, which was formed according to reaction (3.1) and has not yet evaporated.
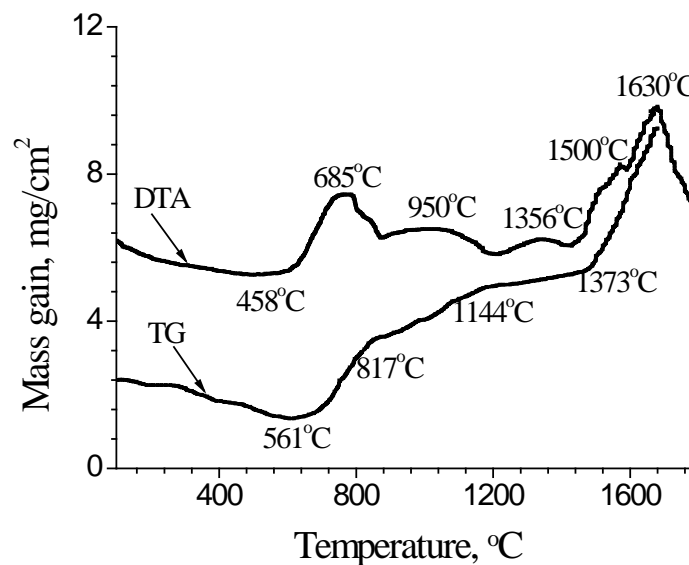
Fig. 3.72. DTA curves of high -temperature oxidation of 35 mas.% ZrB_2 - 65 mas.% SiC ceramics.

However, in this case, the film of borosilicate glass with ZrO_2 and $ZrSiO_4$ additive does not entirely fulfil its protective function. During the experiment at temperatures above 1373 °C, according to TG – curve of Fig. 3.72, the transition to oxidation of these ceramics to linear law is

observed. For this last stage of sample high-temperature oxidation the summary relative mass gain $\Delta m/m_o = 9.23\%$; the exothermal peak of heat evolution takes place at 1630 °C.

Oxidation of 36.8 mas.% ZrB$_2$ - 60 mas.% SiC- 3.2 mas.% ZrSi$_2$ ceramics.

In this case, according to Fig. 3.73, the first kinetic stage of interaction is determined as chemisorption of oxygen with exothermal peak at 120 °C. After that, the appropriate adsorption-desorption equilibrium is established. Finally the oxygen desorption ceases at the temperature range of 370-470 °C. First oxidation stage of this sample – in the temperature range of 517–915 °C – is realized according to equation (1) with the maximum heat evolution rate at 740 °C. The second stage, with α-SiO$_2$ (crystabalite) and ZrSiO$_4$ formation according to equation (3.2), is characterized by the exothermal peak at 1080 °C. Later on, at the temperature rise, the silicate glass is formed with the maximum transformation rate at 1340 °C. Thus, a rather considerable amount of this phase is observed on the sample surface.

The last stage of high-temperature oxidation of this sample up to 1700 °C, according to Fig. 3.73, is characterized by the maximum interaction rate at 1660 °C. It is connected with the formation of borosilicate glass surface film containing ZrSiO$_4$, as an additive in the tight fusion with the glass-like phase. However, this film, as usual, is not entirely protective. The last, high-temperature region of TG-curve of Fig. 3.73 (up to 1700 °C) is also linear one.
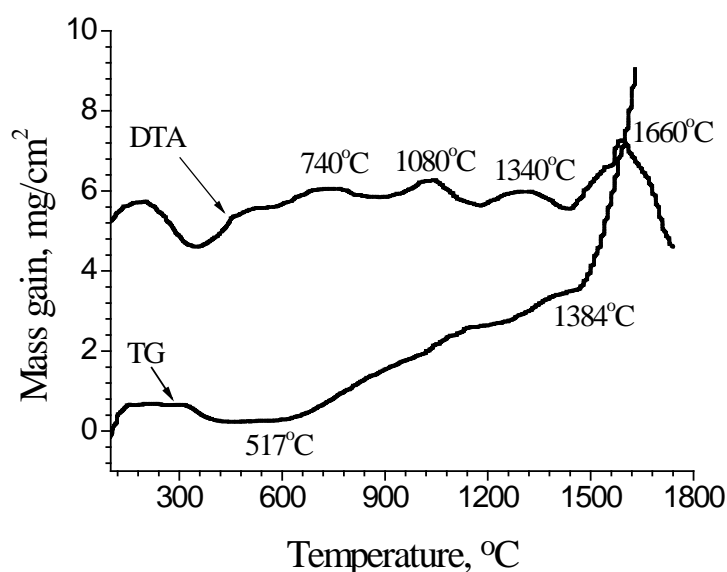
Fig. 3.73. DTA curves of high-temperature oxidation of 36.8 mas.% ZrB$_2$ - 60 mas.% SiC- 3.2 mas.% ZrSi$_2$ ceramics.

For the composition of Fig. 3.72 and Fig. 3.73 attention should be paid to the differences between first two oxidation stages for the double ceramics without $ZrSi_2$ additive and the triple ones with 3.2 mas. % $ZrSi_2$.

On can see that the behavior of these ceramics at the first oxidation stages is sharply differed. In the case of double ceramics, reaction (3.1) of ZrB_2 oxidation begins at 458 °C while in the case of ceramics with the small $ZrSi_2$ additive – at 650 °C. Accordingly, the maximum rate of reaction (3.2) of SiC oxidation for the double ceramics is observed at 950 °C whereas for the triple one – at 1080 °C.

So, in our cases, the small additives of third ($ZrSi_2$) phase, in particular 2-8 mas.%, is capable to slow down the oxidation reaction of ZrB_2, on the whole.

It may be explained by some difficulties of diffusion processes proceeding for zirconium and boron atoms. This, finally, can diminish the rate of these atoms interaction with oxygen.

Beside, the presence of $ZrSi_2$ additives in the ZrB_2-SiC ceramics can lead, in the end, to the some deflection from linearity of the last (the most high-temperature) region of TG-curve, i.e. to reduce the ceramics oxidation rate at very high-temperatures.

Oxidation of 67.3 mas.% ZrB_2 - 26 mas.% SiC- 6.7 mas.% $ZrSi_2$ ceramics.

The TG- and DTA- curves of these ceramics oxidation in the temperature range from room temperature up to 1700 °C (Fig. 3.74) can indicate to about five different oxidation stages of this sample oxidation. At the initial process stage, up to 446 °C, the oxygen adsorption-desorption equilibrium takes place on the sample surface. The exothermal peak of this stage is fitted to the temperature of 80 °C. The first oxidation stage with formation of ZrO_2 (monoclinic.) and B_2O_3 - characterizes more long-term, than in previous cases, period of ZrB_2 oxidation because the initial content of this component in these ceramics is almost than two times higher than in two other samples. Thus, the maximum rate of zirconium boride oxidation to ZrO_2 (monoclinic.) corresponds to 800 °C.
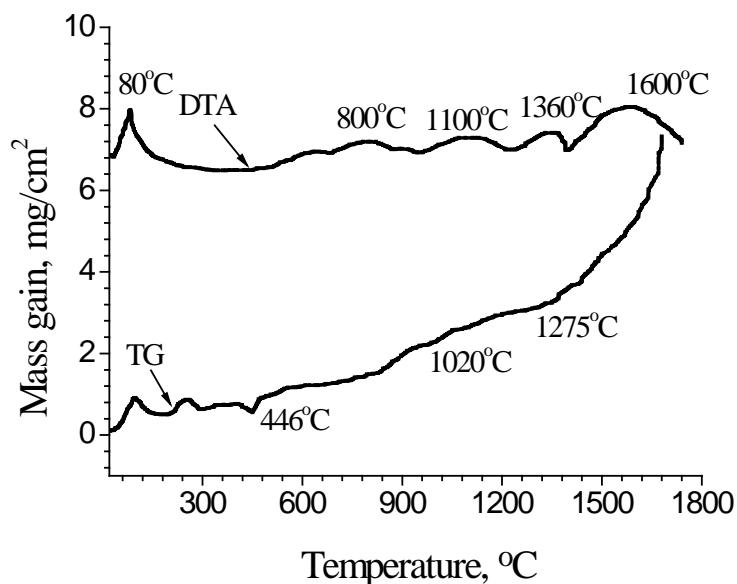
Fig. 3.74. DTA curves of high -temperature oxidation of 67.3 mas.% ZrB_2 - 26 mas.% SiC- 6.7 mas.% $ZrSi_2$ ceramics.

The third exothermal stage of heat evolution on the DTA-curve of oxidation of sample with a higher ZrB_2 content (with the peak at 1100 °C on the account of SiC oxidation to α-crystobalite) at 1280 °C changes to the fourth stage with the peak at 1360 °C. It corresponds to formation of silicate glass in the scale. However, unlike the oxidation of two previous samples, the final region of TG-curve of mass gain of sample with a comparatively great initial content of ZrB_2 in the temperature range of 1320–1700 °C is not characterized by a linear dependence, and it has a shape of inverse parabola. Thus, at the temperature ~ 1350 °C and more, up to 1700 °C, the oxidation, compared with other ceramics, sharply decreases. If for the first ceramics sample the summary mass gain was equal to 9.23, and for second one – 10.64 mg/cm^2, then for this (third) ceramics it is equal to 6.42 mg/cm^2.

The reason of such result, in the case of 67.3 mas.% ZrB_2 - 26 mas.% SiC- 6.7 mas.% $ZrSi_2$ ceramics is, undoubtedly, a stabilization on their surface of upper borosilicate (B_2O_3-SiO_2) layer at very high temperatures on the account of uniform distribution in it of not only $ZrSiO_4$ but also ZrO_2 oxide of tetragonal structure, according to ZrO_2-SiO_2 phase diagram (Fig. 3.75). At the optimum B_2O_3 content in a borosilicate glass (~12 mas. %), namely ZrO_2 proved to be the best stabilizer of this glass. The presence in the borosilicate film of zircon inclusions is identified using petrographic method according to refraction index n(ω) = 1.925-1.961 and n(ε) = 1.980-2.015 (as well as of ZrO_2 inclusions with refraction index n = 2.15).
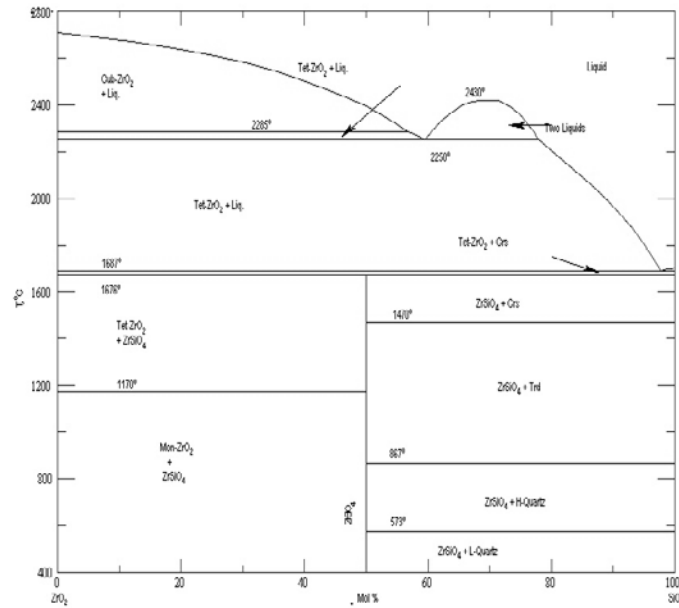
Fig. 3.75. Phase diagram of ZrO_2-SiO_2 system [33].

TG- and DTA-research of oxidation of ZrB_2-$MoSi_2$ ceramics in air up to 1600 °C

Fig. 3.76 and 3.82 show the corresponding curves of mass gain per a surface area value ($\Delta m/S$ mg/cm^2) – TG curves – and heat evolution – DTA-curves – for both kinds of materials studied.
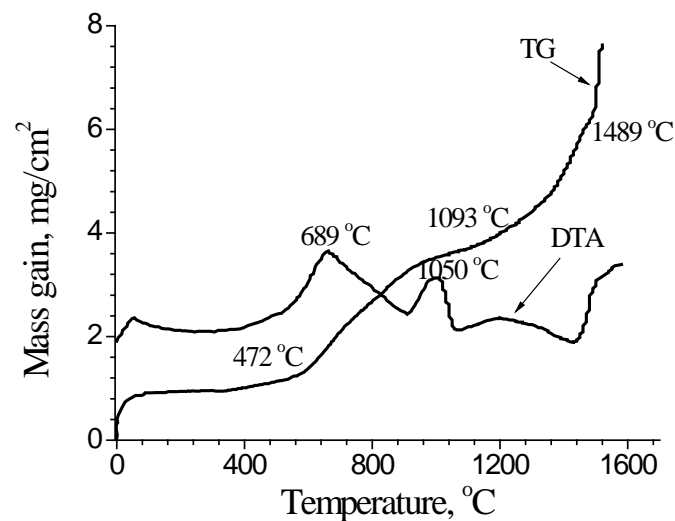
Fig. 3.76. DTA and TG curves of high-temperature oxidation of 56 mas.% ZrB_2-44 mas.% $MoSi_2$ ceramics.

Sample 1 (44 mas. % MoSi$_2$).

According to Fig. 3.76 for the sample (1) at the first oxidation stage there is a comparatively small oxygen adsorption up to 470 °C; the adsorption saturation with oxygen of this sample entirely ends at 100 °C, whereas the sample mass gain on the account of oxidation itself begins only at 470 °C.

The second DTA-peak on the oxidation curve for this sample corresponds to zirconium boride oxidation reaction:

$$2 \, ZrB_2 + 5 \, O_2 = 2 \, ZrO_2 \text{ (monoclin.)} + 2 \, B_2O_3. \tag{3.4}$$
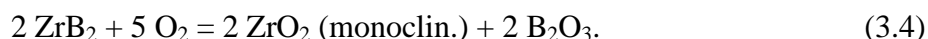
The maximum rate of this reaction corresponds to 690 °C.

Approximately at 950 °C the oxidation of second composite component (MoSi$_2$) begins according to the reaction

$$5 \, MoSi_2 + 7 \, O_2 = Mo_5Si_3 + 7 \, SiO_2, \tag{3.5}$$
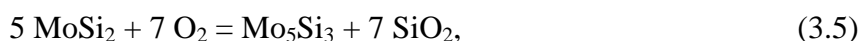
with the formation of the most thermally stable molybdenum silicide Mo$_5$Si$_3$. The DTA peak of this reaction is observed at 1050 °C, its duration – in the temperature range of 950-1100 °C.

The following oxidation stage for sample (1) is the formation on its surface of SiO$_2$ amorphous film stabilized with ZrO$_2$ crystalline phase as well Mo$_5$Si$_3$ crystals, the latter being introduced into SiO$_2$ amorphous film and ensure its stability up to temperature of 1500 °C (see later parts of the report). The temperature of DTA-peak for this oxidation stage, according to Fig. 3.76, proved to be 1260 °C. At the temperatures ~1600 °C there is some loss of protective properties of a scale accompanied with a growth of sample mass gain from 5.0 to 7.6 mg/cm^2 at the temperature increase up to 1600-1650 °C.

It has been shown that in the highest layer of oxide film on the sample with 44 mas.% MoSi$_2$ the absence of ZrO$_2$ and Mo$_5$Si$_3$ crystal inclusions has been established using Auger electron spectroscopy (AES) method. In this layer only silicon dioxide is present.

According to the quantitative AES data, the initial sample of 56 mas.%ZrB$_2$-44 mas.%MoSi$_2$ ceramics for every 18 ZrB$_2$ moles contains 11.5 MoSi$_2$ moles; the Zr:B:Mo:Si ratio is equal to 18.7:42.0:11.5:27.6 at. %.

One can see in Fig. 3.16 the microscopy image of 56 mas.%ZrB$_2$-44 mas.%MoSi$_2$ initial sample surface and in Fig. 3.77 – the results of X-ray spectral analysis of this sample. According to the data of Fig. 3.78 and Fig. 3.79 in the lower layer of oxide film formed at the sample

oxidation for 29 SiO_2 moles there are 0.8 ZrO_2 and 0.14 Mo_5Si_3 moles; the thickness of lower scale layer is equal to 45 μm. Thus, according to the data of AES analysis, the ratio of elements in the lower layer correspond to Si K_α:O K_α = 27.7:63.3 ~ 1:2; Zr L_β:O K_α = 0.9:1.9 ~1:2; Mo L_β:Si K_α = 0.70:0.42 ~ 5:3.
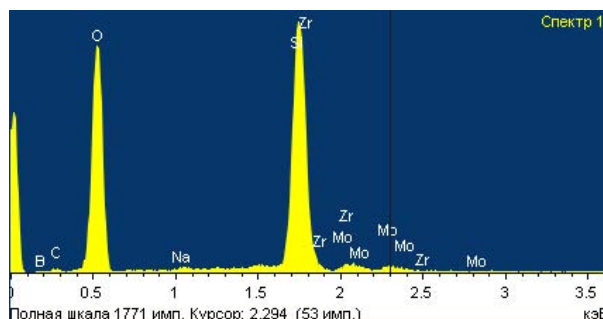
Fig. 3.77. Composition of as-received sample ZrB_2-44 w. % $MoSi_2$ (EDX data).
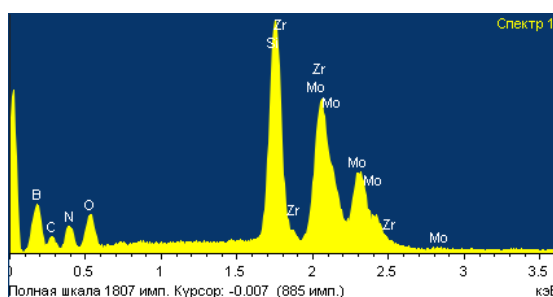
Fig. 78. Composition of lower oxide layer on the (1) ceramics sample (EDX data).

This scale layer does not contain boron (in B_2O_3 composition) because of the intensive B_2O_3 evaporation under reaction (3.4) whereas the molybdenum content in it was essentially decreased on the account of evaporation of MoO_3 which was formed at the first stage of $MoSi_2$ oxidation according to

$$2\ MoSi_2 + 7\ O_2 = 2\ MoO_3\uparrow + 4\ SiO_2 \tag{3.5}$$

reaction.

According to EDX data (Fig. 3.79), the upper oxide layer on the sample (1) consists only of amorphous SiO_2; its thickness is equal to 10-15 μm.
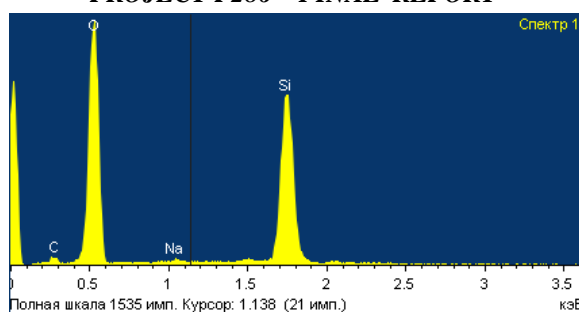
Fig. 3.79. Element composition of upper oxide layer on the ZrB_2-44 w. % $MoSi_2$ ceramics sample.

The SEM picture of this oxide layer formed at the oxidation of sample (1) testifies to its relative heterogeneity (Fig. 3.80 and 3.81). This heterogeneity is connected with the lower adherent sub-layer containing ZrO_2 and Mo_5Si_3 inclusions as well as puff-up due to the gas-components evolution.
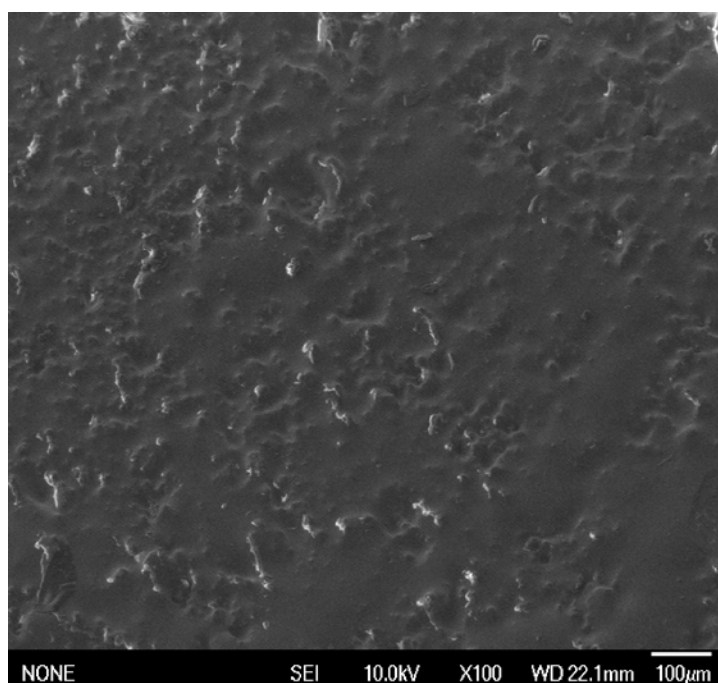
Fig. 3.80. SEM image of upper scale layer surface on the ZrB_2-44 w. % $MoSi_2$ ceramics sample after their oxidation at 1520 °C.
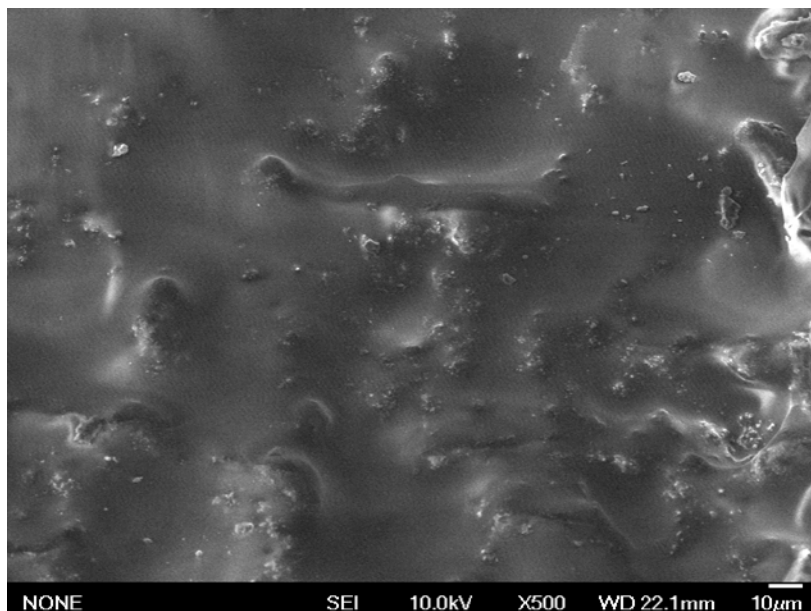
Fig. 3.81. Buildups of amorphous SiO_2 on the surface of sample (2) oxidized up to 1600 °C.

Sample 2 (14 mas. % $MoSi_2$).

At high-temperature oxidation in air of sample 2 (Fig. 3.82) with 86 mas.%ZrB_2-14 mas.%$MoSi_2$, first of all, the adsorption of oxygen on its surface is observed. It is continued till 160 °C, after that the adsorption-desorption equilibrium is achieved. Beginning with the temperature of 470 °C reaction (1) takes place and this process continues up to 745 °C. In the case of sample (2) the oxidation of $MoSi_2$ begins at 740 °C according to reaction (3.5) but proceeds further up to 1150 °C according to reaction (3.4).
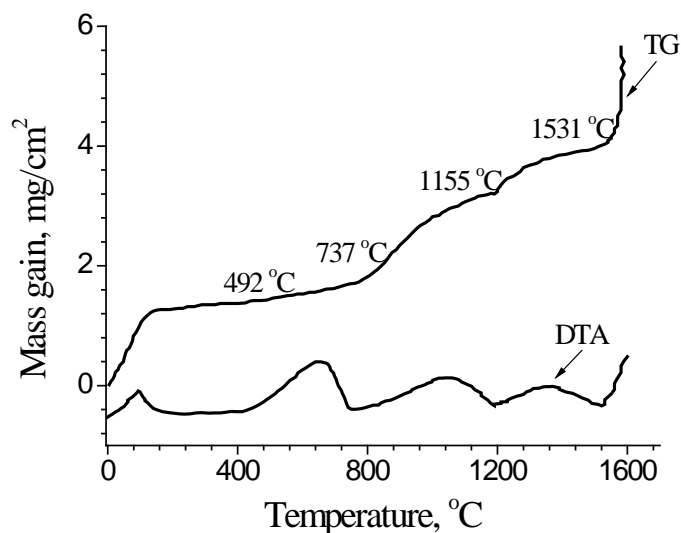
Fig.3.82. DTA and TG curves of high-temperature oxidation of 86 mas.% ZrB_2-14 mas.% $MoSi_2$ ceramics.

The fourth stage of this sample interaction with air oxygen is observed in the temperature range of 1155-1530 °C. Here, the formation of the stable enough SiO_2 amorphous film with the appropriate inclusions of ZrO_2 and Mo_5Si_3 crystallites takes place on the sample (2) surface. As in the case of sample (1), during the last oxidation stage of sample (2) in the temperature range of 1540-1600 °C the more essential increase of sample mass gain is observed (up to 5.8 mg/cm^2).

In the accordance with the data of EDX analysis as well as AES and SEM analyses of the sample (2) oxidized up to 1650-1700 °C one can come to the conclusion that the oxide layer formed on the sample (2) surface contains two sublayers: 1) upper sublayer of amorphous SiO_2 (with the inclusions of ZrO_2), which may have discontinuities at highest temperatures; 2) lower one, with the needle-shaped lamellar structure of ZrO_2 crystallites (Fig. 3.83-3.85)

In the separate experiments the sample (2) ceramics were oxidized up to temperatures of 1650 and 1700 °C. In these cases the surface excrescences on the upper part of a scale cross section of ~ 7-8 μm thickness (Fig. 3.83) consist of only amorphous SiO_2 whereas the deeper scale layer of 15 – 20 μm thickness consists of the significant amounts of ZrO_2 with amorphous SiO_2

One can see in the upper part of Fig. 3.84 the sub-surface scale layer formed on the sample (2) at 1700 °C with a lot of needle-shaped lamellar crystallites, whereas in the lower part of Fig. 3.85 where the upper scale layer formed at 1700 °C is presented, the latter only consists of glass-like SiO_2.
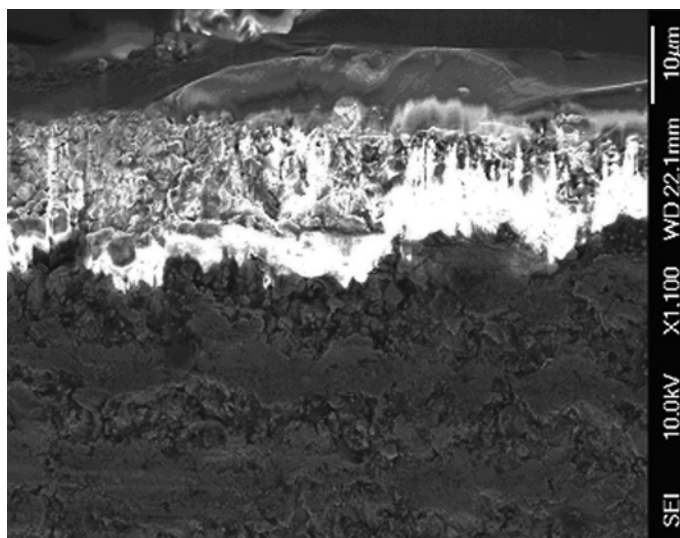
Fig. 3.83. Different oxide layers on the ceramics with 14 w.% $MoSi_2$, oxidized up to 1650 °C (cross section).
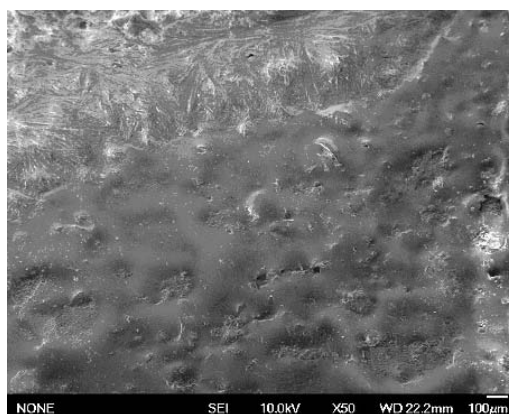
Fig. 3.84. SEM picture of the surface of ceramics (2) oxidized at 1700 °C.
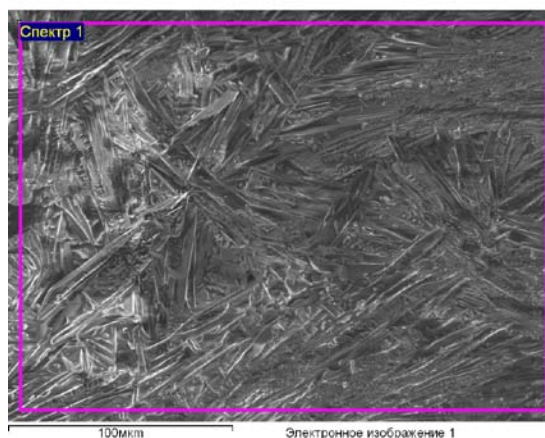
Fig. 3.85. SEM image of lower oxide sublayer on sample (2) after Ar^+ etching.

Thus, the studies have shown that in ceramics ZrB_2-14 mas. % $MoSi_2$ a double layer scale is formed during the oxidation. As in the ZrB_2-SiC ceramics the upper is amorphous sublayer of silica. However, the second sublayer is a dense scale of needle-shaped ZrO_2 crystals, which reinforce the surface and provide additional protection against oxidation. Therefore, under the same conditions of DTA studies the rate of oxidation of ZrB_2-14 mas. % $MoSi_2$ ceramics is lower in the first ceramic system.

3.5. Development of analytic models of high-temperature oxidation of ceramic matrix composites.

Analysis of existing models and development of new ones for characterization of oxidation in investigated ceramic systems.

A review and an analysis of literature sources devoted to high-temperature oxidation of ceramic matrix composites close in its composition to ceramics SiC-Zr_2-Mo (Zr) Si_2 is carried out. This analysis, and own research experience[34,35] and modeling of kinetics of growth of oxide layers on ceramics at high temperatures, enable to draw a conclusion that the main process of formation multilayered oxide films on ceramics SiC-Zr_2-Mo (Zr) Si_2 which control the kinetic of their growth are chemical reactions (transformation) and diffusion processes of oxygen or gaseous products of chemical reactions. The composition (components) of initial ceramics and these processes govern the phase structure, thickness and properties of formed layers. An order of chemical reactions and quantitative ratio of substances involved define an order of formation of oxide layers and their thicknesses.

Therefore in this project modeling of growth kinetics of layers thicknesses in isothermal conditions is carried out on the basis of Evans additive principle according to which time dt, required for a gain of layer thickness dL is a sum of time for chemical transformations dt_c on layer boundaries and time of oxygen (or other gaseous phases) diffusion dt_d to a place of chemical reaction (during the growth of layer there are two consecutive processes: diffusion and chemical transformations).

On the basis of this principle the Cauchy problem is formulated for a system of nonlinear ordinary differential equations (the number of equations is equal to the number of oxide layers); with the solution defining layers thicknesses in a present moment of time i.e. their kinetic. The main constants entering into this system are physical (diffusion) and chemical constants for each layer. These constants are supposed to be found from the experimental kinetic curves of oxide layers growth under isothermal conditions.

This problem is complemented by the equations of quasi-stationary diffusion the solutions of which define distributions of concentration of substances that diffuse in each layer at the present moment of time.

Basic model hypotheses and equations

The main problem:

In isothermal conditions to simulate only growth kinetic of multilayered flat films with given phase structure of layers and their order.

Basic model hypotheses:

1) Kinetic of films growth is defined by chemical reactions and diffusion of substances to layers boundaries where chemical reactions and layers growth occur;

2) Process of film growth is stable i.e. changes of concentration of diffusing substances in layers occur with negligibly low local speed $\dfrac{\partial c}{\partial t} \approx 0$;

3) Chemical reactions at layers boundaries occur with constant velocity $h = const$;

4) Layers are homogeneous, owing to this diffusion coefficients are constant values (probably, the effective characteristics) and distributions of concentration of substances diffusing in layers are linear.

5) Modeling of kinetics of growth of layers thicknesses is carried out on the basis of Evans additivity principle[36,37]:

time dt required for a gain of layer thickness dL, is a sum of time dt_c spent for chemical transformations on layer boundaries and time of oxygen or other substances diffusion dt_d to the place of chemical reactions:

$$dt = dt_c + dt_d. \qquad (3.6)$$

In other words, during growth of a layer two consecutive processes occur: diffusion and chemical transformations.

On the basis of (3.6) the Cauchy problem is formulated for the system of ordinary nonlinear differential equations (the number of equations is equal to the number of layers of a film). A solution of this system defines layers thickness $L_i(t)$ at the current moment of time t i.e. their kinetics.

6) Since growth of a separate layer of a film occurs on its boundaries it is natural to assume that each equation of the Cauchy problem depends only on layer thickness L_i (to which this equation is referring to) and growth rate of thicknesses $\dot{L}_{i-1} = \dfrac{dL_{i-1}}{dt}, \dot{L}_{i+1} = \dfrac{dL_{i+1}}{dt}$ of adjacent layers (i - the number of a layer). Therefore we obtain

$$\begin{cases} \dfrac{dL_i}{dt} = f_i\left(\dot{L}_{i-1}, L_i, \dot{L}_{i+1}\right), \quad i = 1, 2, ..., N, \\ L_i(0) = 0, \quad t \geq 0 \end{cases}, \qquad (3.7)$$

where system (3.7) is supposed to be independent.

On the basis of generalizing analysis of the existing investigations[36,37] one may write down a few types of the Cauchy problems (3.7). These types depend on the order of chemical reactions and quantitative ratios of substances involved, which in its turn define the order of oxide layers formation and their thicknesses.

The main constants entering into (3.7) are physical (diffusion, which are further designated as K_i) and chemical ones (which further are designated as h_i) for each layer as well as constants which follow from the laws of substances conservation (which are defined by chemical reactions and diffusion).

These constants are supposed to be defined from the experimental kinetic curves of growth of separate layers and total thickness of multilayered film in isothermal conditions.

The characteristic feature of the model (3.7) is that the phase composition of layers and their order are defined by chemical reactions and their order at initial moment of time.

In other words, model (3.7) describes the kinetics of growth of multilayered film of a given structure (which is defined by experiment or other methods based on the analysis of chemical reactions and their order in time), and not the formation of the structure itself.

Thus, model (3.7) is very abstract and an essentially depends on structure of multilayered film formed at initial moment of time. Thus, various cases are quite possible. Let's consider some of those, starting from the simplest.

Growth of separate layer occurs at one of its boundaries.

A case when the growth of layer thickness occurs at one of layer boundaries to which diffusing substance involved in chemical reaction which form material of a layer migrates.

In that case Cauchy problem (3.7) for two-layer film (see Fig. 3.86) can be written as

$$
\begin{cases}
\dfrac{dL_1}{dt} = \dfrac{1}{\dfrac{1}{h_1} + \dfrac{L_1}{K_1}}, \\[4mm]
\dfrac{dL}{dt} = \dfrac{1}{\dfrac{1}{h_2} + \dfrac{L_2}{K_2}} + \dfrac{dL_1}{dt}, \\[4mm]
L_1(0) = L_2(0) = 0, \quad t \geq 0
\end{cases}
\tag{3.8}
$$

where L is the full thickness of the film, L_1 is the thickness of the external layer, $h_1 > 0$, $h_2 > 0$ are the chemical constants, $K_1 \geq 0$, $K_2 \geq 0$ are the physical constants.

Physical constants look like:

$$
K_1 = \frac{D_1(c_{1r} - c_{1l})}{c_{1l}}; \quad K_2 = \frac{D_2(c_{2r} - c_{2l})}{c_{2l}},
$$

where D_1, D_2 are the diffusion coefficients of external and internal layers accordingly; c_{1r}, c_{2r} are the concentration of diffusing substances on the right boundaries of external and internal layers, respectively; c_{1l}, c_{2l} are the concentration of diffusing substances on the left boundaries of external and internal layers, respectively; $J_i = D_i grad\ c_i = D_i \dfrac{c_{ir} - c_{il}}{L_i}, i = 1,2$ — flows of diffusing substances in i-th layer. The assumption of uniformity of each layer 4 is important.

If $L_2 = L - L_1$ is taken into account (see Fig. 3.86) system (3.8) degenerates into two independent equations

$$
\begin{cases}
\dfrac{dL_1}{dt} = \left(\dfrac{1}{h_1} + \dfrac{1}{L_1} \right)^{-1}, & L_1(0) = 0, \\[4mm]
\dfrac{dL_2}{dt} = \left(\dfrac{1}{h_2} + \dfrac{1}{L_2} \right)^{-1}, & L_2(0) = 0
\end{cases}
\tag{3.9}
$$

which are integrated in quadratures

$$
t = \frac{L_1}{h_1} + \frac{L_1^2}{2K_1}; \quad t = \frac{L_2}{h_2} + \frac{L_2^2}{2K_2},
\tag{3.10}
$$

and

$$
L_1(t) = -\frac{K_1}{h_1} + \sqrt{\left(\frac{K_1}{h_1} \right)^2 + 2K_1 t}, \quad L_2(t) = -\frac{K_2}{h_2} + \sqrt{\left(\frac{K_2}{h_2} \right)^2 + 2K_2 t}, \quad t \geq 0. \tag{3.11}
$$
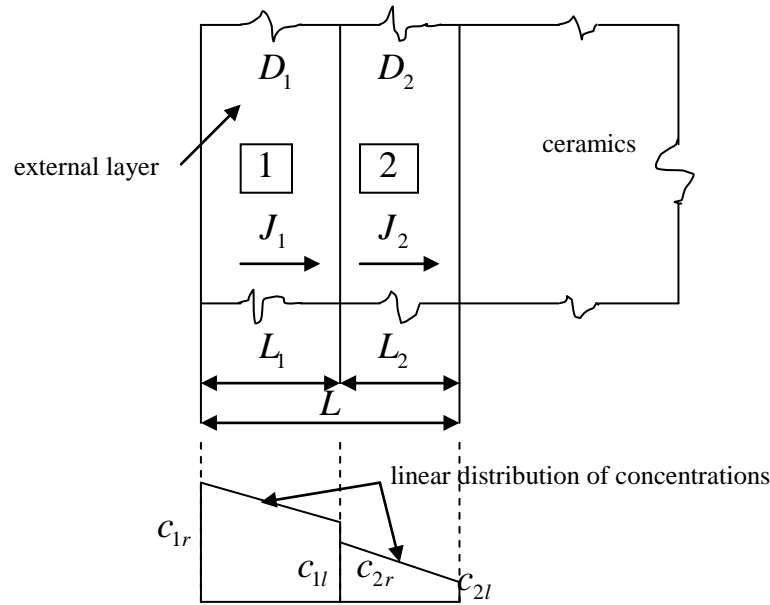
Fig. 3.86. Scheme of homogeneous layers and distributions of concentrations.

From this for total thickness of a film $L(t)$ we obtain

$$L(t) = L_1(t) + L_2(t). \tag{3.12}$$

Equalities (3.10) — (3.12) mean that each homogeneous layer of two-layer film has a parabolic kinetics of growth, however, kinetics of growth of total thickness of a layer $L(t)$ (see (3.12)) is not parabolic.

If a layer is non-uniform then the growth of this layer is not parabolic and distribution of concentrations of diffusing substances in it is not linear.

Problem (3.9) allows generalization for a case of *N*-layer film from homogeneous layers. Thus, the simplest case of the model (3.7) is the case when its equations are independent, i.e.

$$\frac{dL_i}{dt} = \left(\frac{1}{h_i} + \frac{L_i}{K_i} \right)^{-1}, \quad t \geq 0, \quad L_i(0) = 0, \quad i = 1, 2, ..., N, \tag{3.13}$$

where t is the time, h_i, K_i are the chemical and physical constants of i-th layer, N — total number of layers.

An important feature of multilayered film, which kinetic is described by (3.13), is that each layer of this film has parabolic kinetics of growth:

$$t = \frac{L_i}{h_i} + \frac{L_i^2}{2K_i}, \; L_i(t) = -\frac{K_i}{h_i} + \sqrt{\left(\frac{K_i}{h_i}\right)^2 + 2K_i t}, \; t \geq 0, \; i = 1, 2, ..., N, \tag{3.14}$$

however, kinetics of growth of the whole thickness of a film

$$L(t) = \sum_{i=1}^{N} L_i(t), \quad t \geq 0, \tag{3.15}$$

is not parabolic.

It is obvious, that in the considered model (3.13) — (3.15) the structure of constants $h_i > 0$, $K_i > 0$ which are supposed to be defined from the experimental kinetic curves is not that important. This structure gets importance if a nature of formation of constants $h_i > 0$, $K_i > 0$ is investigated, i.e. if not the kinetic of layers growth is investigated but the formation of phase composition of layers and the order of their formation in time.

Thus, model (3.13) — (3.15) describes the growth kinetics of multilayered film of given structure (which is determined in experiment or by other methods), instead of the nature of formation of structure itself.

Growth of separate layer occurs on its two boundaries.

In this case the growth kinetics of i-th layer is described by the following Cauchy problem (see for example[36,37])

$$\frac{dL_i}{dt} = \left(\frac{1}{h_{1i}} + \frac{L_i}{K_{1i}}\right)^{-1} + \left(\frac{1}{h_{2i}} + \frac{L_i}{K_{2i}}\right)^{-1}, \quad L_i(0) = 0, \quad t \geq 0, \quad i = 1, 2, ..., N, \tag{3.16}$$

where $h_{ji} > 0$, $K_{ji} > 0$, $j = 1, 2$ are the chemical and physical constants respectively; $j = 1$ corresponds to the left boundary, $j = 2$ — to the right one.

Solution of the problem (3.16) is a function

$$t = R_1 L_i^2 + R_2 L_i - R_3 \ln(1 + R_4 L_i), \tag{3.17}$$

where

$$R_1 = \frac{1}{2(K_{1i} + K_{2i})}; \; R_2 = \frac{K_{1i}^2 h_{2i} + K_{2i}^2 h_{1i}}{h_{1i} h_{2i} (K_{1i} + K_{2i})^2}; \tag{3.18}$$

$$R_3 = \frac{K_{1i} K_{2i} (h_{1i} K_{2i} - h_{2i} K_{1i})^2}{h_{1i}^2 h_{2i}^2 (K_{1i} + K_{2i})^3}; \; R_4 = \frac{h_{1i} h_{2i} (K_{1i} + K_{2i})}{K_{1i} K_{2i} (h_{1i} + h_{2i})},$$

and growth of layer thickness is not parabolic.

The solution of (3.17), (3.18) generalizes the solution of (3.14): when $K_{2i} \to 0$ solution of (3.17) tends towards the solution (3.14), i.e. when $K_{2i} = 0$ with (3.17) we obtain: $t = \dfrac{L_i}{h_{1i}} + \dfrac{L_i^2}{2K_{1i}}$.

It is obvious, that possible combined cases, i.e. when some layers grow according to (3.13), and others — (3.16).

The literature review shows that one may write out other, more complicated, types of equations of kinetics of formed layers.

Kinetics of growth of two-layer film when an external layer grows due to internal one.

In this case Cauchy problem, which describes growth kinetics of a film, has the form:

$$\begin{cases} \dfrac{dL_1}{dt} = \left(\dfrac{1}{h_1} + \dfrac{L_1}{K_1} \right)^{-1} \\[4mm] \dfrac{dL_2}{dt} = \left(\dfrac{1}{h_2} + \dfrac{L_2}{K_2} \right)^{-1} - \dfrac{dL_1}{dt} \end{cases} . \; L_1(0) = L_2(0) = 0 \qquad (3.19)$$

The problem (3.19) can be also written down as

$$\begin{cases} \dfrac{dL_1}{dt} = \left(\dfrac{1}{h_1} + \dfrac{L_1}{K_1} \right)^{-1} \\[4mm] \dfrac{dL_2}{dt} = \left(\dfrac{1}{h_2} + \dfrac{L_2}{K_2} \right)^{-1} - \dfrac{d}{dt}\left(\sqrt{\left(\dfrac{K_1}{h_1} \right)^2 + 2K_1 t} \right) \end{cases} L_1(0) = L_2(0) = 0 \; ,$$

since $L_1 = -\dfrac{K_1}{h_1} + \sqrt{\left(\dfrac{K_1}{h_1} \right)^2 + 2K_1 t}$ is a solution of the first equation (3.19) for external layer 1

which has a parabolic growth. From here for definition of thickness of internal layer $L_2(t)$ we have the Cauchy problem

$$\dfrac{dL_2}{dt} = \left(\dfrac{1}{h_2} + \dfrac{L_2}{K_2} \right)^{-1} - K_1\left(\left(\dfrac{K_1}{h_1} \right)^2 + 2K_1 t \right)^{-1/2} . \; L_2(0) = 0 \qquad (3.20)$$

Equation (3.20) most likely is not integrated in quadratures. Therefore, its approximated solution can be obtained by numerical methods and growth of internal layer 2 is not parabolic.

From (3.20) follows the following asymptotic form of a growth $L_2(t)$ at $t \to \infty$

$$L_2 = -\frac{K_2}{h_2} + \sqrt{\left(\frac{K_2}{h_2}\right)^2 + 2K_2 t} \approx -\frac{K_2}{h_2} + \sqrt{2K_2 t} \sim \sqrt{2K_2 t} \quad \text{at} \quad t \to \infty \qquad (3.21)$$

i.e. when $t \to \infty$ the law of growth $L_2(t)$ tends to a parabolic law.

Similarly, from (3.20) for asymptotic form of growth $L_2(t)$ when $t \to 0$ we obtain

$$L_2(t) \approx (h_2 - h_1)t \quad at \quad t \to 0, \qquad (3.22)$$

whence follows natural necessary condition of growth of two-layer film:

$$h_2 > h_1, \qquad (3.23)$$

which shows that the layer 1 (external) appears after the layer 2, i.e. it is formed from a material of the layer 2. In other words the velocity of chemical reactions that form layer 2 should be higher than the velocity of chemical reactions that form layer 1. Asymptotic form (3.22) means that diffusion processes do not influence the initial phase of growth of layer L_2, the main influence is caused by chemical reactions.

For the layer L_1 the corresponding asymptotic forms can be written as:

$$L_1(t) \approx h_1 t \quad \text{at} \quad t \to 0. \ L_1 \approx -\frac{K_1}{h_1} + \sqrt{2K_1 t} \ \sim \sqrt{2K_1 t} \quad \text{at} \quad t \to \infty. \qquad (3.24)$$

Asymptotic forms for the whole thickness of the film $L = L_1 + L_2$:

$$L \approx \left(\sqrt{2K_1} + \sqrt{2K_2}\right)\sqrt{t} \quad \text{at} \quad t \to \infty. \ L \approx h_2 t \quad \text{at} \quad t \to 0. \qquad (3.25)$$

Ratios (3.21) – (3.25) can be used for definition of chemical and physical constants h_1, h_2, K_1, K_2 from the experimental kinetic curves of growth of oxide layers. Their use may facilitate the search of these constants.

Kinetic of growth of oxide films in terms of gain of mass

Notations: L_s is the thickness of a part of sample from which a film of total thickness L is formed; ρ_s is the sample density; ρ_i is the density of i-th layer of a film; g is the gain of sample mass per unit of its surface; $\Delta\rho_i = \rho_i - \rho_s$.

The gain of sample mass is

$$g = \sum_{i=1}^{N} \rho_i L_i - \rho_s L_s. \qquad (3.26)$$

Assuming that $L_s \approx \sum\limits_{i=1}^{N} L_i$, i.e. if formation of a film goes without changes of volume or these changes can be neglected, the gain of sample mass may be presented as:

$$g = \sum_{i=1}^{N} \Delta\rho_i L_i = \sum_{i=1}^{N} g_i , \qquad (3.27)$$

where $g_i = \Delta\rho_i L_i$ is the mass gain of i-th layer per one square unit of its surface. This equality is approximated as $L_s \neq \sum\limits_{i=1}^{N} L_i = L$.

Accepting to (3.27), equations (3.13), (3.16), (3.19) may be re-written in terms of a gain of mass. For example, equation (3.19) will assume the form

$$\begin{cases} \dfrac{dg_1}{dt} = \left(\dfrac{1}{h_1} + \dfrac{g_1}{K_1} \right)^{-1} , \\[4mm] \dfrac{dg_2}{dt} = \left(\dfrac{1}{h_2} + \dfrac{g_2}{K_2} \right)^{-1} - \dfrac{dg_1}{dt}, \quad t \geq 0, \, g_1(0) = g_2(0) = 0 \end{cases} , \qquad (3.28)$$

where constants h_i, K_i, $i = 1, 2$, differ from corresponding constants of (3.19) and have another dimension.

More correct would be to assume in (3.27)

$$g_i = \Delta\rho_{is} L_i, \quad \Delta\rho_{is} = \rho_i - \rho_s \frac{L_s}{L}. \qquad (3.29)$$

In this case (see (3.26))

$$g = \sum_{i=1}^{N} g_i = \sum_{i=1}^{N} \rho_i L_i - \rho_s L_s .$$

Let's remind that g_i is the mass gain per unit of surface of i-th layer, g — gain of mass of the whole sample per unit of its surface.

Formula (3.29) accounts for a change of sample's volume at oxidation. When $L = L_s$ we obtain: $\Delta\rho_i = \Delta\rho_{is}$.

It is obvious, that in the considered model the structure of constants $h_i > 0, \quad K_i > 0$ which are supposed to be determined in experiment, is not that important. This structure gains an importance when the nature of formation of constants $h_i > 0, \quad K_i > 0$ is investigated, i.e. when not growth kinetics of layers is investigated but the formation of phase composition of layers and the order of their formation.

In other words, the suggested model investigates the kinetics of growth of a multilayered film of given structure (determined in experiment or by other methods), instead of formation of structure.

Analysis of experimental results of oxidation of systems ZrB_2-SiC **and** ZrB_2-SiC-$ZrSi_2$ **at the temperature 1500 °C**

The case of three-layer scale growth is considered for ceramic systems ZrB_2-SiC and ZrB_2-SiC-$ZrSi_2$ (see Fig. 3.87).
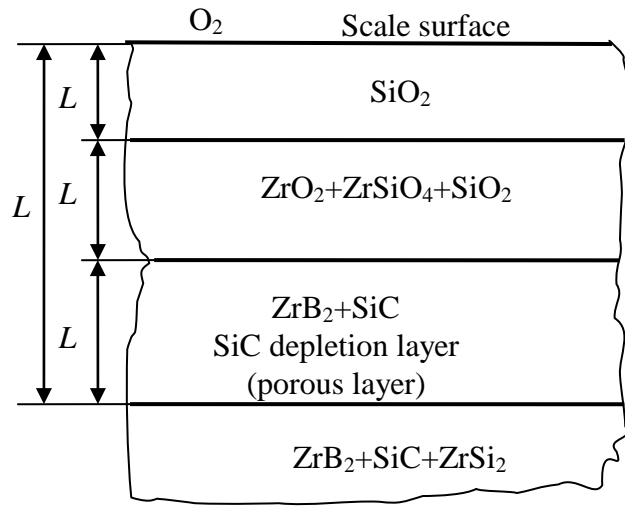
Fig. 3.87. The scheme of the oxide scale structure on the UHTC surface formed after oxidation in pure oxygen at 1500 °C.

If each layer of the scale is growing because of O_2 chemical transformations at the boundary with the next layer (more remote from the scale surface) and reduced because of similar transformations at the boundary with the previous layer (more close to the scale surface), then Cauchy problem, which describes growth kinetics of the scale and takes into account the uncertainties of initial oxidation period, has a form:

$$\begin{cases} \dfrac{dL_1}{dt} = \left(\dfrac{1}{h_1} + \dfrac{L_1}{K_1} \right)^{-1} - \gamma_1 \alpha \exp(-\beta t), \\[2mm] \dfrac{dL_2}{dt} = \left(\dfrac{1}{h_2} + \dfrac{L_2}{K_2} \right)^{-1} - \dfrac{dL_1}{dt} - \gamma_2 \alpha \exp(-\beta t), \\[2mm] \dfrac{dL_3}{dt} = \left(\dfrac{1}{h_3} + \dfrac{L_3}{K_3} \right)^{-1} - \dfrac{dL_1}{dt} - \dfrac{dL_2}{dt} - \gamma_3 \alpha \exp(-\beta t) \end{cases} \qquad \begin{array}{l} L_1(0) = L_2(0) = L_3(0) = 0; \\ t \geq 0 \end{array} \qquad (3.30)$$

where t - time; L_i ($i = 1, 2, 3$) is the layer thickness; $K_i > 0$, $h_i > 0$ are the physical and chemical constants, respectively; $\gamma_i \leq 1$, $i = 1,2,3$ are the weight factors; constants $\alpha \geq 0$, $\beta \geq 0$ take into account the uncertainty of the initial stage of oxidation. Parameter α can be considered as the random peak amplitude of deviation from average speed of scale growth and parameter β - as the parameter determining the effective duration of initial stage of oxidation. Values α, β probably depend on addition $ZrSi_2$, as well.

Cauchy problem (3.30) describes the growth kinetics of the scale with a given structure (which is defined by experiment or other methods based on the analysis of chemical reactions and their order in time), and not the formation of the structure itself.

Since scale growth begins from the 3-rd layer then for a simplification we further assume $\gamma_1 = \gamma_2 = 0$, $\gamma_3 = 1$.

For given $h_i > 0$, $K_i > 0$, α, β the solution of system (3.30) defines layers thickness $L_i(t)$ at the current moment of time t i.e. their kinetics.

Thus, the main problem is to determine key parameters from the experimental kinetic curves: chemical and physical constants $h_i > 0$, $K_i > 0$ as well as parameters α, β that are coefficients in the differential equations of the Cauchy problems (3.30) and define growth kinetics of oxide scale.

The asymptotic analysis of model equations.

Analysis at $t \rightarrow 0$. If condition $h_3 - \alpha > 0$ is assumed to be true then from the system (3.30) follows that its solution at $t \rightarrow 0$ has the following asymptotics

$$L_1(t) \approx h_1 t, \ L_2(t) \approx (h_2 - h_1)t, \ L_3(t) \approx (h_3 - h_2 - \alpha)t,$$
$$L(t) = L_1(t) + L_2(t) + L_3(t) \approx (h_3 - \alpha)t. \tag{3.31}$$

It can be seen from the latter relations (3.31) that condition $h_3 - \alpha > 0$ defines initial nonzero velocity of scale thickness $L(t)$ growth. Besides, conditions

$$h_1 > 0, \ \ h_2 - h_1 > 0, \ \ h_3 - h_2 - \alpha > 0 \tag{3.32}$$

are conditions of formation of three-layer scale at the starting time moment $t = 0$, and left-hand parts of these inequalities define initial velocity of layers formation. The third condition depends on a random factor α and can be true only when $h_3 - h_2 > 0$. From this and from (3.32) follow inequalities: $h_3 > h_2 > h_1 > 0$, which have clear physical sense and determine three-layer structure of the scale: at the initial stage of growth dominate chemical reactions and their velocities $h_i, i = 1,2,3$; the velocity of the 3-rd layer growth h_3 should be higher than velocity of the 2-nd layer formation h_2, which, in its turn, should be higher than velocity h_1 of formation of the 1-st

layer. This is because the 1-st layer is formed from the 2-nd layer, the 2-nd layer is formed from the 3-rd, and the 3-rd layer is formed from initial material. Parameter α can be seen as random amplitude of variation of layer growth velocity and, if inequalities (3.32) are true, then at sufficiently small values of α (i.e. at small random effects and lesser uncertainty) conditions (3.32) will be satisfied.

Analysis at $t \to \infty$. As a result of investigation of the system (3.30) the following estimates for scale layers thicknesses are obtained

$$\underline{L}_i(t) \le L_i(t) \le \overline{L}_i(t), \quad t \ge 0, \tag{3.33}$$

where functions $\underline{L}_i(t), \overline{L}_i(t), i = 1, 2, 3$ are determined by equalities

$$\overline{L}_i(t) = -\frac{K_i}{h_i} + \sqrt{\left(\frac{K_i}{h_i}\right)^2 + 2K_i t}, \quad t \ge 0, \quad \underline{L}_1(t) = \overline{L}_1(t) + \frac{\alpha}{\beta}\left(\exp(-\beta t) - 1\right), \tag{3.34}$$

$$\underline{L}_2(t) = \overline{L}_2(t) - \overline{L}_1(t), \quad \underline{L}_3(t) = \overline{L}_3(t) - \overline{L}_2(t).$$

From (3.33), (3.34) we have the following relations useful for kinetics analysis

$$\overline{L}_1(t) - \underline{L}_1(t) = \frac{\alpha}{\beta}\left(1 - \exp(-\beta t)\right) \ge 0, \quad \overline{L}_2(t) - \underline{L}_2(t) = \overline{L}_1(t) \ge 0, \quad \overline{L}_3(t) - \underline{L}_3(t) = \overline{L}_2(t) \ge 0, \quad t \ge 0,$$

and asymptotic at $t \to \infty$ equalities

$$\lim_{t \to \infty} \frac{\underline{L}_1(t)}{\overline{L}_1(t)} = 1, \quad \lim_{t \to \infty} \frac{\underline{L}_2(t)}{\overline{L}_2(t)} = 1 - \sqrt{\frac{K_1}{K_2}}, \quad \lim_{t \to \infty} \frac{\underline{L}_3(t)}{\overline{L}_3(t)} = 1 - \sqrt{\frac{K_2}{K_3}}. \tag{3.35}$$

Since from the physical point of view only positive boundaries should be considered in equalities (3.35) then from (3.35) follow inequalities

$$K_1 \le K_2 \le K_3. \tag{3.36}$$

For the thickness of the whole scale $L(t)$ at $t \ge 0$ from equalities (3.34) we have estimates

$$\underline{L}(t) \le L(t) \le \overline{L}(t), \tag{3.37}$$

where

$$\overline{L}(t) = \sum_{i=1}^{3} \overline{L}_i(t), \quad \underline{L}(t) = \overline{L}_3(t) + \frac{\alpha}{\beta}\left(\exp(-\beta t) - 1\right), \quad \text{and} \quad \lim_{t \to \infty} \frac{\overline{L}(t)}{\underline{L}(t)} = 1 + \sqrt{\frac{K_1}{K_3}} + \sqrt{\frac{K_2}{K_3}}.$$

The performed analysis shows that at $t \to \infty$ dominating process in layer formation is oxygen diffusion (in relations (3.34), (3.35) leading role are playing physical constants $K_i, i = 1, 2, 3$).

From (3.33), (3.34) at sufficiently large values of t the following inequalities are obtained

$$L_i(t) \le \sqrt{2K_i t}, \quad L(t) \le \sqrt{2Kt},$$

where $L = L_1 + L_2 + L_3$, $K = \left(\sqrt{K_1} + \sqrt{K_2} + \sqrt{K_3}\right)^2$. These inequalities mean that the growth of separate layers and the whole scale can not be above the parabolic growth, i.e. kinetic growth curves of layers and scales are below of the certain conventional parabolic kinetic curves which is determined by the constants h_i, K_i, K.

Thus, obtained relations (3.31)-(3.37) can be used for determination of physical and chemical constants $K_i, h_i, i = 1, 2, 3$, as well as parameters α, β from experimental kinetic curves of growth of oxide scale layers. The use of these relations facilitate their search by numerical methods.

The numerical determination of parameters governing the scale growth kinetics

If formation of a scale goes without volume changes or these changes can be neglected, then equations (3.30) may be re-written in terms of mass gain:

$$\begin{cases} \dfrac{dg_1}{dt} = \left(\dfrac{1}{h_1} + \dfrac{g_1}{K_1}\right)^{-1}, \\[2mm] \dfrac{dg_2}{dt} = \left(\dfrac{1}{h_2} + \dfrac{g_2}{K_2}\right)^{-1} - \dfrac{dg_1}{dt}, \\[2mm] \dfrac{dg_3}{dt} = \left(\dfrac{1}{h_2} + \dfrac{g_3}{K_3}\right)^{-1} - \dfrac{dg_1}{dt} - \dfrac{dg_2}{dt} - \alpha \exp(-\beta t) \end{cases} \quad t \geq 0, \; g_1(0) = g_2(0) = g_3(0) = 0, \quad (3.38)$$

where constants $\alpha, \beta, h_i, K_i, i = 1, 2, 3$ differ from corresponding constants of (3.30) and have other dimensions; g_i, $i = 1, 2, 3$ are the mass gain per unit of surface of i-th layer, $g = g_1 + g_2 + g_3$ are the mass gain of the whole sample per unit of its surface.

Here we determine parameters $K_i, h_i, i = 1, 2, 3$, α, β (see (3.38)) from experimental kinetic curves of oxide scale growth. However, in reality we have a limited set of experimental data which is presented in Fig. 3.54 and these are separate points belonging to kinetics curves $g(t)$ of the total scale growth, not to growth curves of individual layers. Structure of scale is determined at some moments of time also. Therefore, a simple problem is considered in which the first two layers are presented by some effective single layer with effective characteristics K_1, h_1 and equations (3.38) are reduced to the following Cauchy problem

$$\begin{cases} \dfrac{dg_1}{dt} = \left(\dfrac{1}{h_1} + \dfrac{g_1}{K_1}\right)^{-1} \\[2mm] \dfrac{dg_2}{dt} = \left(\dfrac{1}{h_2} + \dfrac{g_2}{K_2}\right)^{-1} - \dfrac{dg_1}{dt} - \alpha \exp(-\beta t) \end{cases} , \quad g_1(0) = g_2(0) = 0 \quad (3.39)$$

Recall that in (3.39) function g_1, K_1 and h_1 correspond to effective external layer and g_2, K_2 and h_2 are referred to 3-rd layer (see Fig. 3.87).

Function $g_1 = -\dfrac{K_1}{h_1} + \sqrt{\left(\dfrac{K_1}{h_1}\right)^2 + 2K_1 t}$ is a solution of the first equation (3.39) for external effective layer which has a parabolic growth. From this for definition of mass gain of internal layer $g_2(t)$ we have the Cauchy problem

$$\frac{dg_2}{dt} = \left(\frac{1}{h_2} + \frac{g_2}{K_2}\right)^{-1} - K_1 \left(\left(\frac{K_1}{h_1}\right)^2 + 2K_1 t\right)^{-1/2} - \alpha \exp(-\beta t) , \quad g_2(0) = 0. \qquad (3.40)$$

Similar to the asymptotic analysis of solutions for equations (3.39) and (3.40) can be done.

Equation (3.40) most likely is not integrated in quadratures. Its approximated solution can be obtained by numerical methods, and growth of internal layer is not parabolic.

A number of calculations using this model has been done with the aim to determine model parameters and validate functional dependencies of the model. Data fitting procedure was carried out with the least squares method. Objective function — a sum of squares of deviations of mass gain from experimental one. Initial data for the calculation of parameters of kinetic curves were taken from the experimental measurements of isothermal oxidation for 50 h at 1500 °C:

Parameters – diffusion and reaction constants: K_1, h_1, K_2, h_2 and constants taking into account uncertainties of initial oxidation period α, β, were found for ZrB_2-SiC and for ZrB_2-SiC-$ZrSi_2$ ceramics. Calculated kinetic curves are shown in Fig. 3.88 ($g = g_1 + g_2$).
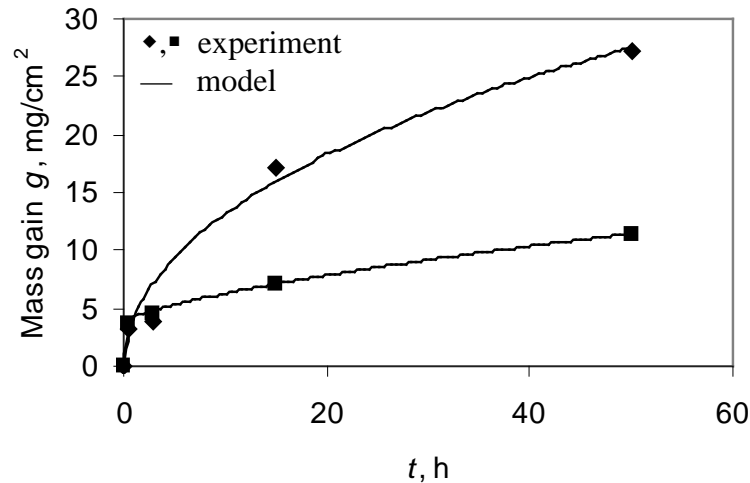

Fig. 3.88. The curves of isothermal oxidation of US4 (diamonds) and USS4 (squares) samples in pure oxygen at 1500 °C.

The analysis shows that at $t \to \infty$ the dominant process in layer formation is oxygen diffusion (in relations (3.34) and (3.35) leading role are playing physical constants K_i, $i = 1, 2, 3$). From the model calculations follows that the outer layers (in our approximation SiO_2 and $ZrO_2 + ZrSiO_4 + SiO_2$) are rate-limiting step since diffusion constant K_1 in these layers is significantly lower than K_2 for layer $ZrB_2 + SiC$ (SiC depletion layer), see also (3.36) and Table 3.1.

Table 3.1. Calculated model parameters.

Ceramics	K_1, mg^2/cm^4 h	h_1, mg/cm^2 h	K_2, mg^2/cm^4 h	h_2, mg/cm^2 h	α, mg/cm^2 h	β, 1/h
ZrB_2–SiC	0.82	0.26	47.2	289.5	10.9	0.0036
ZrB_2–SiC–$ZrSi_2$	1.75	0.93	8.16	125.9	0.29	0.0011

From (3.33) and (3.34) at sufficiently large t the following inequalities are obtained $L_i(t) \leq \sqrt{2K_i t}$, $L(t) \leq \sqrt{2Kt}$, where $L = L_1 + L_2 + L_3$, $K = (\sqrt{K_1} + \sqrt{K_2} + \sqrt{K_3})^2$. These inequalities mean that the growth of separate layers and the whole scale cannot be above parabolic growth, i.e. kinetic growth curves of layers and scales are below certain conventional parabolic kinetic curves which are determined by the constants h_i, K_i, K. Thus, relations (3.31)–(3.37) can be used for determination of physical and chemical constants K_i, h_i, $i = 1, 2, 3$, as well as parameters α and β from experimental kinetic curves of growth of oxide scale layers. The use of these relations facilitates their search by numerical methods.

The analysis shows that the addition of $ZrSi_2$ leads to the reduction of chemical reaction rate (h_2) by 2.3 and effective diffusion constant (K_2) by 5.8 times, the latter points to sharp decrease of oxygen diffusion in layer 2. These results correspond to the analysis of Figs. 3.54 and 3.63 in Section 3.4.

3.6. Electrochemical oxidation of ZrB_2-$MoSi_2$ ceramics

Electrochemical (anodic) oxidation of ceramic materials.

The investigation of process of preliminary formation of protective oxide coatings on the surface of samples of ZrB_2-SiC and ZrB_2-SiC-$ZrSi_2$ UHTC at the electrochemical (anodic) polarization has been carried out. The formation of such films on the ceramic samples can promote to an increase of corrosion resistance of these materials at high temperatures in the air and pure oxygen media.

Since the mechanisms of high-temperature and electrochemical oxidation of metals, alloys and ceramic materials have similar peculiarities, the multi-stage character of oxide films

formation as well as a sequence of formation on the samples of different oxide phases in both cases may coincide.

Concerning the peculiarities of oxides formation kinetics, in the many cases at the gas corrosion one can expect the same correlation of oxidation reactions rates as it happens during corrosion in the electrolyte, namely, in the 3% NaCl solution as an analog of sea water.

In order to compare the rates of electrochemical oxidation of double ZrB_2-SiC ceramics of different composition in 3% NaCl solution the two kinds of such ceramics have been used, namely, US4 (49.5 vol.% SiC – 50.5 vol.% ZrB_2) and US3 (23 vol.% SiC – 77 vol.% ZrB_2) samples while for the triple ceramics – USS4 sample of the following composition: 46 vol.% ZrB_2 - 4 vol.% $ZrSi_2$ – 50 vol. % SiC.

ZrB_2 is a ceramic compound belonging to the group of the borides of IV transition metals. It has a compact hexagonal structure similar to that of titanium diboride. It is characterized by high melting point (3040 °C), high hardness (9-22 GPa) and wear resistance, relatively low density and high electrical conductivity. It has high modulus, good flexural strength and low coefficient of thermal expansion. However, its poor fracture toughness limits its reliability for many applications[38]. That is why it is necessary to study corrosion behavior of double and triple ZrB_2-based ceramics of different composition.

In order to obtain the comparable picture of corrosion resistance in the same conditions we have also investigated rates and mechanisms of electrochemical corrosion of ZrB_2 samples in three different states: crystal sample, amorphous phase, nanocrystal coating of ZrB_2 on SiC substrate obtained using magnetron scattering. For a comparison of electrochemical corrosion of boride and corresponding metal (ZrB_2 and iodide Zr) we have studied also kinetics of oxide film formation on the surfaces of both zirconium boride and metallic zirconium.

The kinetics of anodic oxidation of all the samples have been studied using the potential-dynamic method of polarization curves (P 5848 device) at the potential change rate of 0.5 mV/s in the electrochemical cell with Pt cathode (electrolyte – 3% NaCl solution). As a comparison electrode the Ag/AgCl/KCl standard electrode was used. In this study all the potentials have been given in the relation to this electrode.

The results of polarization measurements of the anode current density (i_a, A/cm^2), i.e. oxidation rate of appropriate sample, in dependence on anode potential (E, V) are presented in Fig. 3.89 for Zr, crystal ZrB_2, amorphous ZrB_2 and nanocrystal ZrB_2 coating on SiC whereas in Fig. 3.90 for the two samples of double ceramics of different composition (US4 and US3) and the sample of triple ceramics USS4. The composition of oxide films obtained at the anodic oxidation

has been preliminarily studied by the method of Auger electron spectroscopy using a LAS-2000 device, Riber, France.

For the qualitative determination of Zt^{3+} and ZrO^{2+} ions in the electrolyte solution as a result of anodic oxidation of corresponding samples, the methods of zirconium analytic chemistry have been selectively used.

First of all, on the basis of investigation carried out one can conclude that both amorphous ZrB_2 and nanocrystal ZrB_2 coating on SiC have the highest corrosion resistance in the 3% NaCl solution (Fig. 3.89) even compared with the composite ceramics studied (Fig. 3.90). So, at the comparably large anodic potentials $E_a \sim 1.5…2.0$ V their corrosion rate is negligibly small and corresponds to the current density of $i_a \sim 10^{-5.5} … 10^{-6}$ A/cm^2. For these two samples the stationary potential is equal to –0.25 V and during the polarization till the potential $E_a = 1.0$ V for coating and 0.5 V for amorphous ZrB_2 one can observe only desorption of early chemically adsorbed oxygen.

Further, in the potential range of 0.5…1.1 V, formation of very thin ZrO_2 film takes place, on the amorphous ZrB_2, stable at room temperature. However with the increase of anodic potential higher than 1.7 V, this film becomes unstable because its conductivity becomes "electrolytic" one[39]. For such film the conductivity is exceptionally small, probably, even less than that for quartz. Only in the potential range more than 1.7 V (up to 2.0 V) ZrO_2 film becomes extraordinarily stable again.

During oxidation of ZrB_2 coating on SiC, the formation of stable ZrO_2 oxide layer begun on it already at 1.15 V, and up to the potential E = 2.0 V one can observe only thickening of oxide layer if it is possible to say so about exceptionally thin oxide film on this coating. At the beginning of this sample oxidation (E = 1.0…1.1 V) the partial dissolution of coating with almost negligible rate occurs according to the reaction

$$ZrB_2 + 7\,H_2O = ZrO^{2+} + 2\,BO_3^{3-} + 14\,H^+ + 10\,e^- \qquad (3.41)$$

It should be noted here that the rate of electrochemical oxidation of both samples is by 100 times less than oxidation rate of compact crystal ZrB_2 sample, and by $\sim$ 100000 times less than rate of metallic zirconium oxidation.

E, B

Lg(i), (A/cm²)

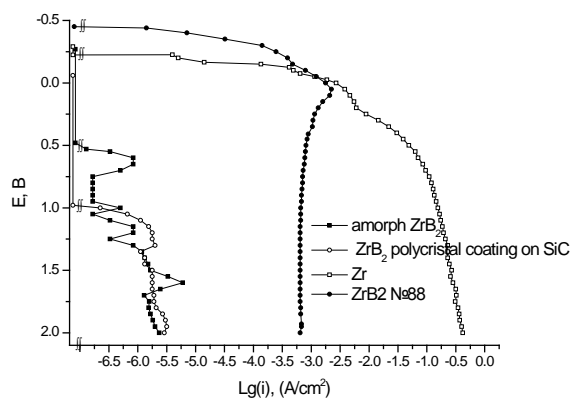- ■ amorph ZrB₂
- ○ ZrB₂ polycristal coating on SiC
- □ Zr
- ● ZrB2 №88

Fig. 3.89. Polarization curves of anodic oxidation of Zr, polycrystal ZrB₂, amorphous ZrB₂ and nanocrystal ZrB₂ coating on SiC substrate.

E, B

- ○ US-4 49,5%iC+50,5%rB₂
- ◆ USS-4 50%% (ZrB₂+8%rSi₂)+50%iC
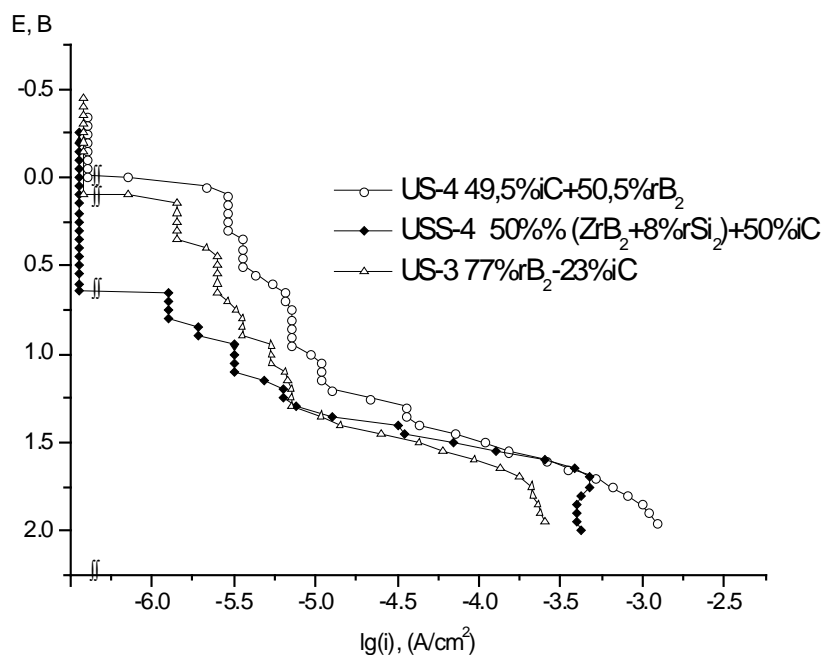- △ US-3 77%rB₂-23%iC

lg(i), (A/cm²)

Fig. 3.90. Polarization curves of anodic oxidation of samples of binary and triple ceramics.

One can see in Fig. 3.89 in appropriate polarization curve that the oxidation of zirconium is goes on in two stages. The first one, from E = –0.25 to E = –0.12 V, corresponds to metal dissolution with the formation in the solution of ZrO^{2+} ions:

$$Zr + H_2O = ZrO^{2+} + 2 H^+ + 4 e \qquad (3.42)$$

The second stage (from –0.12 to +2.0 V) corresponds to the simultaneous formation of ZrO_2 zirconium dioxide of monoclinic modification and $Zr(OH)_4$ zirconium hydroxide which is deposited on the bottom of electrolytic cell:

$$2\,Zr + 6\,H_2O = ZrO_2 + Zr(OH)_4 + 8\,H^+ + 8\,e \qquad (3.43)$$
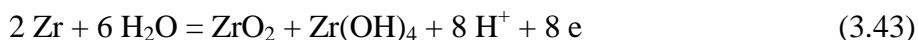
It may be noted that among all the studied samples metallic zirconium proved to be the least resistant to the anodic oxidation.

The primary electrochemical dissolution of ZrB_2 sample is carried out in two stages: at first – according to the reaction (3.41), and then, at the sharper slope of polarization curve, – in the accordance with the equation

$$ZrB_2 + 6\,H_2O = Zr^{3+} + 2\,BO_3^{3-} + 12\,H^+ + 9\,e \qquad (3.44)$$
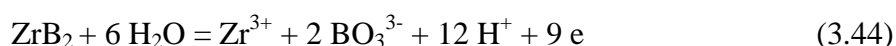
Beginning from the potential –0.01 V the oxidation process for ZrB_2 becomes relatively stable and obeys the following equation:

$$ZrB_2 + 8\,H_2O = ZrO_2 + 2\,BO_3^{3-} + 16\,H^+ + 10\,e \qquad (3.45)$$
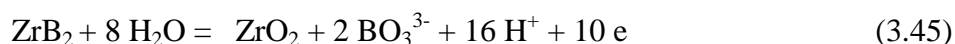
At the potentials from +0.25 to 2.0 V the region of limiting current is observed on the polarization curve, $i_a = 10^{-3.25}$ A/cm^2, which corresponds to the formation on the sample surface of ZrO_2 protective film.

Compared with ZrB_2 sample both ZrB_2-SiC ceramics studied proved to be more corrosion-resistant in the sea water, especially in the anodic potential range up to 1.0 V. This can be explained in the following way. The initial samples of these ceramics are a priori characterized by essential chemical adsorption of oxygen: the field of oxygen desorption on the corresponding polarization curves corresponds to the values of anodic potential from –0.5 almost to 0.2 V. As a result of anodic polarization up to potential 1.2 V and for ceramics containing 23 vol.% SiC even up to 1.35 V formation of protective ZrO_2 oxide film on their surfaces is observed. However, with the increase of polarization this film grows on the samples as four separate layers in accordance with four separate regions of the limited current on the polarization curves.

This is connected with the following. The ZrO_2 formed on such samples during oxidation is in the form of oxihydrate. As a rule, oxihydrates form depositions which are similar to colloid solutions. They are so fine-dispersed that at the XRD investigation were identified as amorphous ones. Due to very developed surface they hold water by adsorption forces and partially, probably, capillary forces. Obviously, the water is connected with ZrO_2 molecules in such manner and also chemically. However, later on the oxihydrate film is transformed to the deposits with crystal

properties which may be confirmed by XRD method. In our case atoms are in the ZrO_2 lattice but not in $Zr(OH)_4$.

One can see in Fig. 3.90 that the developed triple (46 vol. % ZrB_2 - 4 vol.% $ZrSi_2$ - 50 vol. % SiC) ceramic has a very high corrosion resistance in the sea water: at the potential of 1.35 V i_a = 10^{-5} A/cm^2. At the anodic potentials up to 1.7 V on the samples of these ceramics only protective ZrO_2 film has been formed. The peculiarity of these ceramics behavior also consists of full passivation of their surface at potentials of 1.8…2.0 V. It is connected with a final formation of zirconium silicate $ZrSiO_4$ phase on their surfaces.

In Fig. 3.91 one can see the anodic potential-dynamic polarization curves of electrochemical oxidation in 3 % NaCl solution of hot-pressed ZrB_2 (1), 56 vol.% ZrB_2 – 44 vol.% $MoSi_2$ (2) and 93 vol.% ZrB_2 – 7 vol.% $MoSi_2$ (3) ceramics, and $MoSi_2$ (4) samples as well as in Fig. 3.92 – of fused ZrB_2 samples.

According to Fig. 3.91 and data of quantitative Auger–electron spectroscopy (AES), the anodic dissolution of hot-pressed ZrB_2 sample during first stage of electrochemical oxidation is accompanied by its dissolution in the electrolyte with the transition of ZrO^{2+}-, BO_3^{3-}- and H^+- ions into solution:

$$ZrB_2 + 7 \, H_2O = ZrO^{2+} + 2BO_3^{3-} + 14 \, H^+ + 10e^- \qquad (3.46)$$
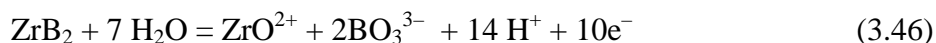
The second stage of electrochemical oxidation of hot-pressed ZrB_2 sample in the range of anodic potentials from –0.35 to –0.01 V may be presented by the equation

$$ZrB_2 + 6H_2O = Zr^{3+} + 2BO_3^{3-} + 12H^+ + 12e^- \qquad (3.47)$$

Further, at the potentials more than –0.01 V, up to 1.65 V, the passivation of sample surface is observed as a result of formation of outer ZrO_2 oxide layer that is confirmed by AES data:

$$ZrB_2 + 8 \, H_2O = ZrO_2 + 2BO_3^{3-} + 16 \, H^+ + 10 \, e^- \qquad (3.48)$$
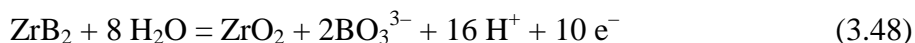
Unlike the polarization curves of Fig. 3.91, the polarization curve of Fig. 3.92 for the fused ZrB_2 sample, which does not contain pores and has more uniform structure, in the range of anodic potentials from the stationary potential (–0.7 V) up to 1.75 V has only two oxidation stages – in accordance with (3.46) and (3.47) equations. Besides, the extreme current of ZrO_2 oxide film

formation in this case is approximately by 50 times less, while the oxide film proved to be more compact and, practically, does not contain the expressed structure defects.

Molybdenum disilicide finds various applications at elevated temperatures due to its exceptional high temperature oxidation resistance along with its high thermal conductivity and thermodynamic stability. However, $MoSi_2$ proves extremely unstable at lower temperatures oxidizing rapidly according to the linear kinetics. This phenomenon, well known as the $MoSi_2$ pest, occurs in the temperature range 600-700 ℃ because oxidation products (mostly the lower silicide Mo_5Si_3 along with the evaporating MoO_3) are unable to form protective film[12-14]. The effective oxide coating forms only at higher temperatures where silica appears among the other oxide film components. Therefore it is advisable to create on the $MoSi_2$ surface a thick protective silica-based film in advance by quickly reaching high temperatures.
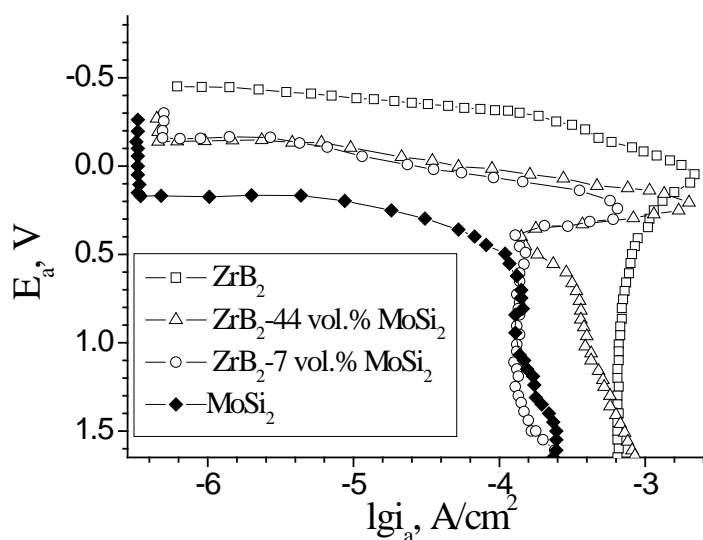

Fig. 3.91. Anodic polarization curves of ZrB_2, $MoSi_2$ and $ZrB_2 – MoSi_2$ ceramics oxidation.

On the other hand, molybdenum disilicide having metallic conductivity may also be subjected to electrochemical treatment in order to form an oxide film of adjustable thickness. All previous papers on electrochemical behavior of $MoSi_2$ – as well as other silicides neither reveal the oxidation mechanism[40-41] nor go deep enough into detailed kinetics of the process[42]. In this study we discuss experimental kinetics of $MoSi_2$ anodic oxidation with a SiO_2 film formation as well as interpret data obtained via known oxidation models.
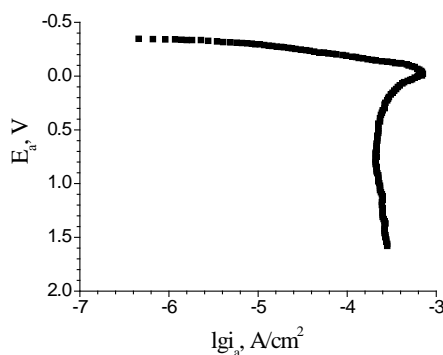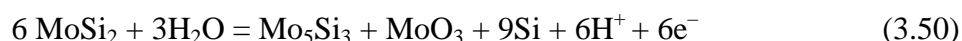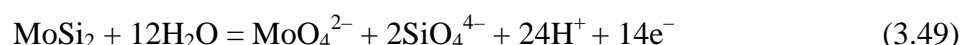
Fig. 3.92. Anodic polarization curves for fused ZrB_2 in 3% NaCl solution.

The anodic oxidation process for the hot-pressed $MoSi_2$, unlike ZrB_2 and ZrB_2–$MoSi_2$ oxidation, first of all, is characterized by vertical region of polarization curve from the stationary potential (–0.25 V) up to –0.15 V, which fits to the oxygen electrochemical desorption, the latter being a priori chemisorbed on the surface of this sample (Fig. 3.91).

According to this curve, further, the oxidation rate of this sample is increased almost up to potential of 0.8 V. After that the region of the extreme current begins, that may testify to formation on this sample surface of intermediate $MoSi_2$ oxidation products – Mo_5Si_3 and MoO_3 – and, later, comparatively thick layer of nanocrystal SiO_2.

Now we shall discuss in detail the last stage of $MoSi_2$ sample anodic polarization, i.e. the growth of silicon dioxide film on its surface. For this the anodic polarization curve for this sample has to be more favourably presented in Fig. 3.93.

The anodic polarization curve for $MoSi_2$ in 3% NaCl solution is shown in Fig. 3.91. Current density grows rapidly along with the potential until the former reaches the maximum point at E = +0.8 V. Further follows current density decay down to the plateau beginning from E = +0.85 V. Thus, three different electrochemical processes are to be distinguished: electrochemical dissolution (0.15 – 0.8 V), formation of intermediate oxidation products such as Mo_5Si_3, MoO_3, and silicon (0.8 V – 1.4 V) according to the equations (3.49) and (3.50)

$$MoSi_2 + 12H_2O = MoO_4^{2-} + 2SiO_4^{4-} + 24H^+ + 14e^- \qquad (3.49)$$

$$6\,MoSi_2 + 3H_2O = Mo_5Si_3 + MoO_3 + 9Si + 6H^+ + 6e^- \qquad (3.50)$$

as well as growth of thick SiO_2 nanofilm (1.4 – 2.0 V)[18]. We are going to discuss the last stage of anodic polarization, i.e. the growth of silicon oxide film on the surface.

The AES data of the oxidized $MoSi_2$ surface are given in Table 3.2.

Table 3.2. Thickness and element content (at. %) of the oxide film formed on the MoSi$_2$

surface under anodic polarization in 3% NaCl solution; Si$_{ox}$ is silicon combined with oxygen.

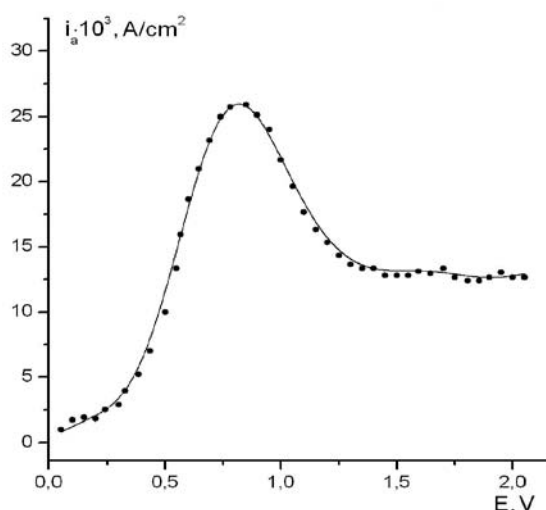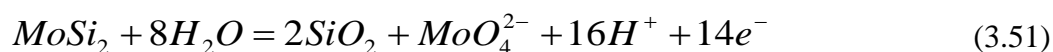| ξ, nm	O	Mo	Si$_{ox}$	Si
0	73.4	3.5	22.6	0.2
2	63.4	4.5	30.9	0.2
5	50.7	10.5	22.6	14.6

Fig. 3.93. Anodic polarization curves of MoSi$_2$ in 3% NaCl solution.

It is obvious from the element molar ratio Si$_{ox}$:O ~ 1:2 that only silica forms on the surface according to the equation

$$MoSi_2 + 8H_2O = 2SiO_2 + MoO_4^{2-} + 16H^+ + 14e^-$$ (3.51)

Minor Mo traces in the oxide nanolayers do not belong to any products of electrochemical reaction because there is not enough molybdenum to form any substance (MoO$_3$) in equivalent relations to silicon and oxygen present in the film. Hence molybdenum oxide, having formed on the previous oxidation stage, should accumulate on the grain boundaries, whereas the silica nanofilm grows on the grain surface. This may be illustrated by the SEM image of the MoSi$_2$ oxidized surface (Fig. 3.94).

All mentioned above allows us to imagine the oxidation process as depicted in Fig. 3.95. On the surface of MoSi$_2$ grain grows the silica layer through which oxygen ions O^{2-} diffuse towards the interface accelerated by the electric field of the anode. These ions originate from water

molecules nearby the electrode surface. The electric field strips the oxygen atom off and draws it into the oxide film; the protons are repulsed to combine with a water molecule and diffuse into bulk of the solution. The silicon atoms must obviously move in the opposite direction. Meanwhile, molybdenum atoms diffuse laterally along the grain surface towards a grain boundary where MoO_3 already exits and through which the oxygen ions might also diffuse.
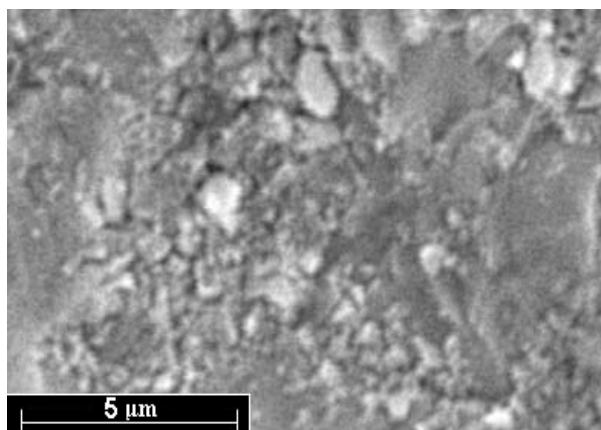

Fig. 3.94. SEM image of the oxidized $MoSi_2$ surface after anodic treatment.
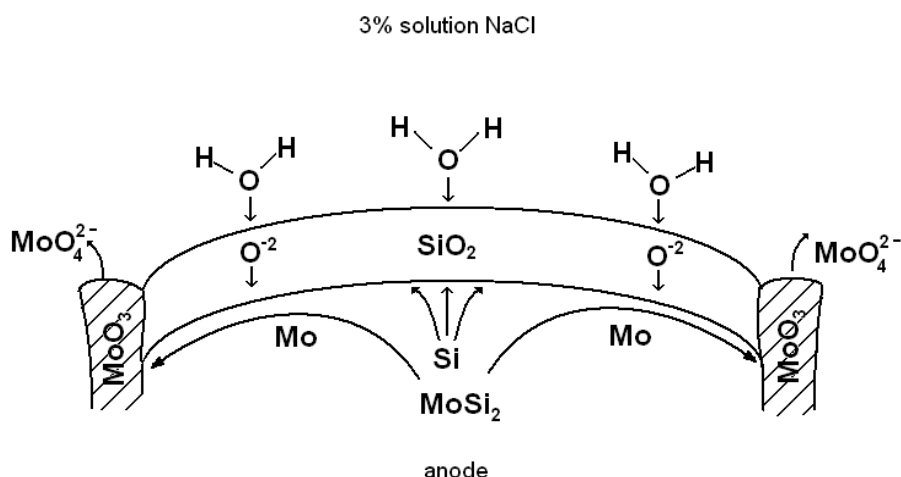

Fig. 3.95. The scheme of SiO_2 film growth on the surface of $MoSi_2$ under anodic polarization.

When a molybdenum atom enters the MoO_3 isle, a molybdate-ion MoO_4^- dissolves from the other side into the electrolyte. Thus the SiO_2 film grows covering almost the whole surface except grain boundaries.

In order to obtain kinetic parameters of the process above the chronamperometric curves (Fig. 3.96.) have been recorded at different potentials on the plateau (1.5 – 2.0 V). Each curve of

current density decay consists of two stages: the first one with current density (reaction rate) falling rapidly during the first few minutes of the process and the second one (10 - 90 min.) which rate decreases slowly implying that diffusion through the film formed on the surface limits the process rate. If any of these current density curves is integrated, one obtains a parabola which takes its conventional shape through recalculation of the charge into SiO_2 mass gain according to equation (3.51).

The corresponding process of $MoSi_2$ high-temperature oxidation at the highest stage (~ 1500 ºC) can be described by the following equation[44]:

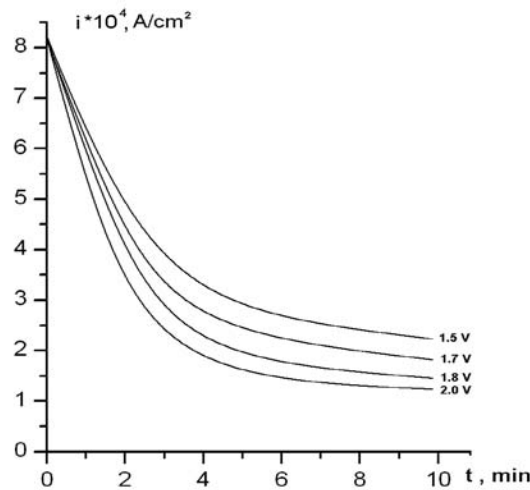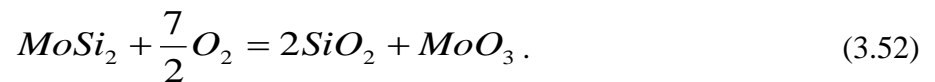$$MoSi_2 + \frac{7}{2}O_2 = 2SiO_2 + MoO_3 . \tag{3.52}$$

Fig. 3.96. Chronamperometric curves of $MoSi_2$ oxidation in 3% NaCl solution in the potential range 1.5 – 2.0 V.

Since molybdenum trioxide evaporates readily at 1500 ºC, the experimental isothermal TG-curves would show mass loss. In order to obtain a conventional parabolic mass gain curve one should subtract the mass loss due to MoO_3 evaporation. The charge (an area under a chronamperometric curve) can be recalculated into the SiO_2 film thickness using the Faraday's law. Taking into consideration only silica film formation, one obtains parabolic curves as shown in Fig. 3.97.

$$\xi = \frac{i\tau}{nF} \cdot V_{SiO_2} \ . \tag{3.53}$$

Here ξ is the film thickness, i is the current density, n is the number of electrons in equation (3.46), F is the Faraday's constant, V_{SiO_2} is the molar volume of silicon dioxide.

    The integrated kinetic curves can be linearized (Fig. 3.98) in appropriate coordinates for the parabolic law which allows to calculate parabolic constants from them. The parabolic constants obtained at different potentials prove to depend linearly on the electrode potential that is shown in Fig. 3.99. It is absolutely obvious that the diffusion of oxygen ions through the oxide film should be directly accelerated by the potential difference arising in it.
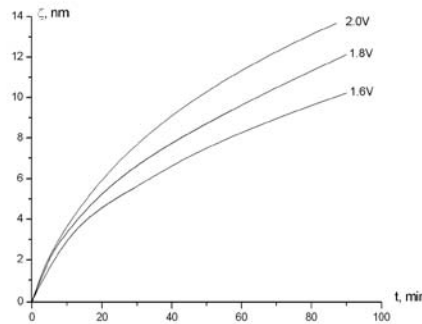

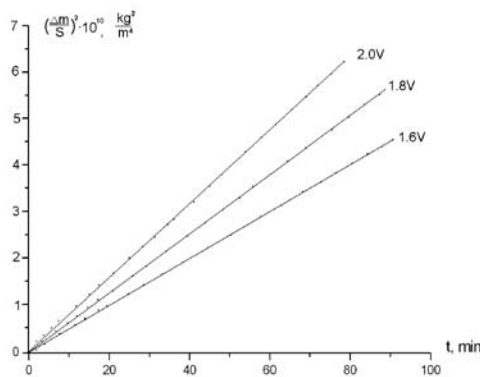Fig. 3.97. Parabolic growth of SiO_2 nanofilm on $MoSi_2$.

Fig. 3.98. Integrated and linearized parabolic curves of the $MoSi_2$ anodic oxidation in 3% NaCl solution.
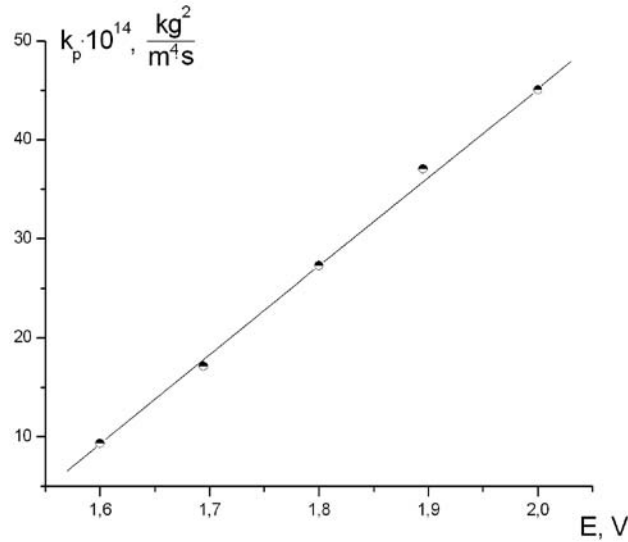
Fig. 3.99. Dependence of the parabolic constant of MoSi$_2$ anodic oxidation on the polarization potential.

The experimental data above may be discussed in terms of Mott-Cabrera theory for thin oxide films formed as a result of oxidation in air. This theory is applicable for the growth of thin oxide films both under high-temperature[45] and electrochemical treatment[46-47]. According to the Mott-Cabrera theory, electrons in metal due to the tunnel effect penetrate through a very thin film (a few nm) to the gas/metal interface where they combine with adsorbed oxygen atoms leaving behind the equivalent amount of metal ions. The established charge distribution in a double electric layer with oxygen concentration falling exponentially generates a strong electric field (~ 10^9 V/m) across the film. This field accelerates diffusion of ions towards the interface. For the films of medium thickness (up to 100 nm), the Mott-Cabrera theory offers the equation which accounts for the parabolic kinetics as well as the linear dependence of the reaction rate constant on the polarization potential:

$$\frac{d\xi}{dt} = \frac{1}{\xi}\left(n_i D_i v \frac{eV}{kT}\right) = \frac{k' \cdot V}{\xi} \,. \tag{3.54}$$

Here ξ is the film thickness, n_i is the concentration of diffusing ions, D_i is the diffusion coefficient, v is the molar volume of oxide, V is the voltage drop in the oxide film, and k' is the effective parabolic constant. In the case of electrochemical polarization the voltage drop in the film should be proportional to the polarization potential which is observed experimentally.

However, it should be noted that the original theory was designed for high-temperature oxidation and its employment from the electro-chemical standpoint is an inverse problem. While the electric field arises in the film spontaneously during the oxidation and can be calculated from the system parameters, it is being established manually in the case of an electrochemical experiment.

Thus, it was established that only SiO_2 formed on the surface as an oxidation product during oxidation in the potential range + 1.5–2.0 V whereas molybdenum tended to transfer into the electrolyte. The physical model offered implies that, by growing on the grain surface, the silica nanofilm covers almost all the sample surface. Molybdenum oxides being located at the grain boundaries serve as medium through which Mo diffuses to the disilicide/elecrtolyte interface leaving it in form of molybdate ion. The silica growth kinetics in the potential range of +1.5–2.0 V measured using the chronamperometric method proved to be parabolic, i.e. oxygen diffusion through SiO_2 film limited the process rate. The parabolic constants calculated from the integrated chronamperometric curves prove to be linear dependent on the electrochemical potential applied which fits into the Mott-Cabrera model for the formation of thin oxide films.

The first oxidation stages of ZrB_2-$MoSi_2$ composites as well as $MoSi_2$ sample (Fig. 3.91) are characterized by electrochemical desorption from their surfaces of a priori chemisorbed oxygen (from the stationary potentials up to – 0.1 V).

After that for both ceramic samples - 56 vol.% ZrB_2 – 44 vol.% $MoSi_2$ and 93 vol.% ZrB_2 – 7 vol.% $MoSi_2$ (see Fig. 3.91) – up to the potentials of 0.14 – 0.20 V at first the reaction (3.46) takes place with a very small rate ($i_a \sim 10^{-5}$A/cm^2), and then – according to reaction (3.49). Hereby the rate of reaction (3.49) for the sample with a greater $MoSi_2$ content significantly outdoes such one for the sample with its lesser content.

It must be noted that the $MoSi_2$ additive to ZrB_2, undoubtedly, promotes to sample surface passivation, compared with each of individual components (ZrB_2 and $MoSi_2$).

So, as a result of a deep surface passivation of ceramics sample with 44 vol.% $MoSi_2$ the rate of its interaction with the electrolyte at the potential of E = 0.35 V is decreased more than by 10 times. Herewith in the anodic potential region from 0.65 V to 1.15 V the rate of corrosion of ZrB_2 sample with 7 vol.% $MoSi_2$, according to reaction (3.51), is equal to individual $MoSi_2$ corrosion rate.

It may be assumed that comparatively great additives of $MoSi_2$ to ZrB_2 promote the formation of outer oxide layer on the ZrB_2 – $MoSi_2$ ceramics according to (3.49) and (3.50)

reactions whereas at the anodic potential range from 0.65 to 1.17 V on the ceramics with 7 vol.% $MoSi_2$ the SiO_2 outer protective layer is already formed according to reaction (3.51).

It allows to come to the conclusion that the $MoSi_2$ additives to ZrB_2 (both great and comparatively small amounts) promote the rise of its corrosion resistance in 3% NaCl solution. Thus, the 5-10 vol.% $MoSi_2$ additives have especially beneficial effect. Namely they ensure the highest increase of corrosion resistance for these ceramics in the electrolyte studied.

Conclusions

1. The introduction of $ZrSi_2$ (all other factors being the same) assists in activating sintering and therefore reduces porosity in ZrB_2-SiC based ceramics and widens the range of silicon carbide concentrations where formation of pore-free materials have been observed. The structure of these materials is heterogeneous. The final phase composition depends on the amount of $ZrSi_2$ introduced. If the zirconium silicide content is lower than 8 vol.% the phase composition is ZrB_2-SiC-Zr(Hf)C(B), otherwise the phase composition is ZrB_2-SiC-Zr(Hf)C(B)-$ZrSi_{2(modified)}$.

   For the raw materials and hot pressing conditions used in this study, the content of zirconium silicide is optimal at about 2 vol.%. At higher zirconium silicide contents (above 8 vol.%) degradation of the additional liquid phase in the resulting ceramics, during longer isothermal exposures at elevated temperatures, was discovered. Further, degradation of the grain boundary amorphous phase resulted in the appearance of porosity at the grain-boundaries and a decrease in bending strength.

2. The mechanical properties of ZrB_2-SiC and ZrB_2-SiC-$ZrSi_2$ hot pressed ceramics (with grain sizes 10–15 µm) in the composition range 0–60 and 0–14 vol. % of SiC and $ZrSi_2$ respectively were studied. The introduction of SiC improves mechanical properties (hardness of 18–20 GPa, bend strengths of 400–500 MPa, contact strength in tension of 400–650 MPa) and the maximum of strength characteristics is formed at high SiC content. The dependences of mechanical properties of ceramics on silicon carbide content are in a good accordance with conclusions of a thermo-mechanical model based on the mechanical properties of heterogeneous ceramics. The addition of $ZrSi_2$ (up to 4 vol. %) slightly affects bending strength of ceramics but essentially improves the contact strength and homogeneity characteristic (Weibull modulus from 7 to 24) at low temperature. However, the high-temperature (1400 °C) strength decreases (from ~430 MPa to ~320 MPa for double and triple (ZrB_2-SiC-$ZrSi_2$)) ceramics.

3. The investigations indicated that ZrB_2–SiC–$ZrSi_2$ ceramics with the optimal composition (2 wt% of $ZrSi_2$), had the best oxidation resistance for long-duration (50 h) exposure to pure oxygen at 1500 °C. The ZrB_2–SiC–$ZrSi_2$ ceramic had 3.4 times higher resistance to oxidation compared to the ZrB_2–SiC based on mass gain. In comparison with other non-oxide ceramics, such oxidation resistance is exceptionally high (the mass gain is <10 mg/cm^2 at 1500 °C after 50 h oxidation in pure oxygen).The oxidation process had kinetics that showed nearly ideal parabolic behavior for long times. The model of growth kinetics for a multilayered scale was

proposed. The model predictions showed good agreement of calculated and experimental oxidation kinetic curves. It was shown that increase of oxidation resistance of triple ceramics (ZrB_2–SiC–$ZrSi_2$) is due to decreased oxygen diffusion rate in subsurface layer. The role of the subsurface layer is enhanced by the fact that this layer is more uniform in thickness compared with the outer layer of glass which is varied in thickness up to discontinuity. Comparison with experimental data shows that calculated model parameters fully correspond to physical meaning of the oxidation process. At high-temperature oxidation the Na_2CO_3 and NiO additives on the ceramic surfaces have no practical effect on the oxidation process of UHTCs while the Al_2O_3 and Fe_2O_3 ones have had significant influence on the scale formed.

With the aid of DTA- and TG-methods as well a XRD and petrographic analyses of scale compositions the kinetics and mechanism of high-temperature oxidation in air up to 1700 °C of ZrB_2-SiC-$ZrSi_2$ ceramics have been studied. The five-stage oxidation mechanism has been established at the consecutive increase of samples heating with the rate 20 °/min. The succession of the processes proved to be the such one: 1) oxygen desorption-adsorption; 2) formation of ZrO_2 and B_2O_3 oxides; 3) formation of α-SiO_2 crystobalite and $ZrSiO_4$ zircon; 4) formation of SiO_2 amorphous phase; 5) formation of upper borosilicate protective film with ZrO_2 and $ZrSiO_4$ inclusions at the SiC content in the interval sample < 40 mas.%. It has been shown that the small additives of $ZrSi_2$ (< 4 mas.%) in interval samples significantly lower the oxidation rate at the first oxidation stages.

The thickness, composition, morphology and structure of different oxide layers formed on the ZrB_2-$MoSi_2$ ceramics samples of different composition oxidized in air at high temperatures (up to 1600-1700 °C) may significantly differ from each other. In ceramics ZrB_2-14 mas. % $MoSi_2$ a double layer scale formed during the oxidation: the upper is amorphous sublayer of silica; the second sublayer is a dense scale of needle-shaped ZrO_2 crystals, which reinforce surface and provide additional protection against oxidation.

4. The electrochemical (anodic) oxidation in 3% NaCl solution of hot-pressed ZrB_2, $MoSi_2$, 93 vol.% ZrB_2 – 7 vol.% $MoSi_2$, 56 vol.% ZrB_2 – 44 vol.% $MoSi_2$ ceramics and fused ZrB_2 samples have been studied using potential-dynamic polarization curve method. It has been shown that the all of ceramics studied are characterized by high corrosion resistance in the 3% NaCl solution, i.e. also in the sea water. The electrochemical oxidation data obtained, on the whole, proved to be in the agreement with the high-temperature oxidation data for the studied ceramics. For the $MoSi_2$ oxidation the kinetic data obtained can be explained in the terms of Mott-Cabrera theory for thin oxide films formation.

References

1. Tripp W.C., Davis H.H., Graham H.C. Effect of a SiC addition on the oxidation of ZrB_2. Am. Ceram. Soc. Bul., 1973, **52**, 612-616.

2. Grigoriev O.N., Gogotsi Yu. G., Subbotin V.I. Structure and properties of $SiC-MeB_2$ ceramics. Mat. Res. Soc. Symp. Proc., 1998, **481**, 249-254.

3. Chamberlain A.L., Fahrenholtz W. G., Hilmas G.E. and Ellerby D.T. High-strength zirconium diboride-based ceramics. J. Am. Ceram. Soc., 2004, **87**(6), 1170-1172.

4. Monteverde F. Beneficial effects of an ultra-fine α-SiC incorporation on the sinterability and mechanical properties of ZrB_2. Appl. Phys. A, 2006, **82,** 329-337.

5. Zhu S., Fahrengoltz W. G., Hilmas G.E. Influence of silicon carbide particle size on the microstructure and mechanical properties of zirconium diboride – silicon carbide ceramics. J. Euro.Ceram. Soc. 2007, **27**, 2077-2083.

6. Monteverde F. and Bellosi A. Effect of the addition of silicon nitride on sintering behavior and microstructure of zirconium diboride. Scripta Mater., 2002, **46**, 223-228.

7. Monteverde F. and Bellosi A. Beneficial effects of AlN as sintering aid on microstructure and mechanical properties of hot-pressed ZrB_2. Adv. Eng. Mater., 2003, **5**(7), 508-512.

8. Guo S.Q., Nishimura T., Mizuguchi T. and Kagawa Y. Mechanical properties of hot pressed ZrB_2-MoSi_2-SiC composites. J. Euro. Ceram. Soc., 2008, **28**(9), 1891-1898.

9. Guo S.Q., Kagawa Y., Nishimura T. and Tanaka Y. Pressureless sintering and physical properties of ZrB_2-based composites with $ZrSi_2$. J. Euro. Ceram. Soc., 2009, **29**(4), 787-794.

10. Chamberlain A. L., Fahrenholtz W. G., Hilmas G.E. Pressureless Sintering of Zirconium Diboride. J. Am. Ceram. Soc., 2006, **89** (2), 450–456.

11. Grigoriev O.N., Gogotsi Yu. G., Brodnikovsky N.P., Subbotin V.I. Structural state and strength of ceramics $SiC-B_4C-MeB_2$ system. in Electron Microscopy and strength of materials, IPMS Publ., Kiev, 1999, p. 129-142, (in Russian).

12. Grigoriev O.N., Gogotsi Yu. G., Brodnikovsky N.P., Subbotin V.I. Development and properties of $SiC-B_4C-MeB_2$ ceramics. Powder Metallurgy, 2000, 5/6, 29-42 (Transl. from Russian).

13. Ordanyan S.S., Unrod V.I. Eutectics in the systems of refractory compounds and they models – sintering composites. New Refractories, 2005, 7, 42-48 (in Russian).

14. Lavrenko V.A., Panasyuk A.D., Protsenko T.G. et al. High-temperature reactions of materials of ZrB_2 -$ZrSi_2$ system with oxygen. J. Powder Metallurgy and Metal Ceramics, 1982, 21(6), 471-473.

15. Lavrenko V.A., Dayatel V.D., Lugovskaya E.S. Interaction of materials ZrB_2-$ZrSi_2$ system with oxygen at high temperature. Powder metallurgy, 1982, 6, 56-58, (Transl. from Russian).

16. Talmy I.G., Zaykovski J.A., Opeka M.M. High-Temperature Chemistry and Oxidation of ZrB_2 ceramics Containing SiC, Si_3N_4, Ta_5Si_3, and $TaSi_2$. J. Amer. Ceram. Soc. 2008, 91(7), 2250-2257.

17. Peng F., Speyer R.F. Oxidation Resistance of fully Dense ZrB_2 with SiC, TaB_2, and $TaSi_2$ additives. J. Amer. Ceram. Soc. 2008, **91**(5)**,** 1489-1494

18. Talmy I.G., Zaykovski J.A.,Opeka M.M., and Smith A.H. Properties of Ceramics in the System ZrB_2 - Ta_5Si_3. J. Mater. Res., 2006, **21**(10), 2593-2599.

19. Silvestroni L., Sciti D. Effects of $MoSi_2$ additions on the properties of Hf- and $Zr – B_2$ composites produced by pressureless sintering. Scripta Mater., 2007, **57**, 165-168.

20. Guo S.Q., Kagawa Y., Nishimura T. and Tanaka Y. Pressureless sintering and physical properties of ZrB_2-based composites with $ZrSi_2$. J. Euro. Ceram. Soc., 2009, **29**(4), 787-794.

21. Opila E., Levine S., Lorincz J. Oxidation of ZrB_2- and HfB_2-based ultra-high temperature ceramics : effect of Ta additions. J. Mater. Sci., 2004, **39**, 5969-5977.

22. Talmy I.G, Zaykovski J.A., Opeka M.M., Dallek S. Oxidation of ZrB_2 ceramics modified with SiC and Group IV-VI transition metal borides. In: McNallan M, Opila E, editors. High temperature corrosion and material chemistry III. Pennington, NJ: The Electrochemical Society, Inc.; 2001. p. 144.

23. Guo S-Q., Kavagava Y., Nishimura T. Mechanical behaviour of two-step hot-pressed ZrB_2-based composites with $ZrSi_2$. J. Europ. Ceram Soc., 2009, **29,** 787-794.

24. Opeka M. M., Talmy I. G., Wuchina E. J., Zaykoski J. A. and Causey S. J. Mechanical, thermal and oxidation properties of refractory hafnium and zirconium compounds. J. Europ. Ceram. Soc., 1999, **19**, 2405–2414.

25. Galanov B.A., Grigoriev O.N. Analytic indentation model of brittle solids. In. Electron microscopy and strength of materials, IPMS Publ., Kiev, 2006, p.4-42 (in Russian).

26. Bogachyov I.N., Weinstein A.A., Volkov S.D. Introduction in statistical metallurgical science. M.: Metallurgy. - 1972. – 216 pp (in Russian).

27.   Niihara K., Morena R., Hasselman D.P.H. Evaluation of K_{1c} of brittle solids by the indentation method with low crack-to-indent ratios . J. Mat. Sci. Let. - 1982.-1, No 1. - P. 13-16.

28.   Rudy E. Part V. Compendium of phase diagram data, Ternary phase equilibria in transition metal-boron-carbon-silicon systems, Tech. Rep. No. AFML-TR-65-2, Contract Nos. USAF 33(615)-1249 and 33(615)-67-C-1513, Air Force Materials Laboratory; Wright-Patterson Air Force Base, Ohio, 689 pp. (1969).

29.   Grigoriev O.N., Trefilov V.I., Khoroshun L.P. Residual stresses in two-phase ceramic composites. In Proc. of III All-Union Conf. ”Technological Residual Stresses”, Acad. Sciences of USSR, Moscow, 1988, p. 129-133 (in Russian).

30.   Galanov B.A., Grigoriev O.N. Fracture Criterion of Composites with a Ceramic Matrix. Problemy Prochnosti, 1993, 10, p.30-40 (Transl. from Russian).

31.   Andrievsky A.R., Spivac I.I. Strength of refractory compounds and materials on its base. M.: Metallurgy. - 1989. – 368 pp (in Russian).

32.   Lanin A.G., Fedik I.I. Thermal stress resistance of materials. Podolsk. Scientific Institute of Association "LUCH", 2005, 312 pp (in Russian).

33.   Berezhnoy A.S. Multicomponent systems of oxides. Kiev: Naukova dumka. - 1970. - 216 pp (in Russian).

34.   Galanov B.A., Ivanov S.M., Kartuzov E.V., Kartuzov V.V., Nickel K.G., Gogotsi Y.G. Model of oxide scale growth on Si_3N_4 ceramics: nitrogen diffusion through oxide scale and pore formation. Computational Materials Science, 2179-85.

35.   Galanov B.A., Ivanov S.M., Kartuzov E.V., Kartuzov V.V., Gogotsi Y.G., Schumacher C., Nickel K.G. Computer modeling of oxide scale growth on Si-based ceramics. Proc. Per Kofstad Memorial Symposium on High Temperature Corrosion and Materials Chemistry, Honolulu, Hawaii, 1999, ed. By M.McNallan, E. Opila, T.Maruyama, and T. Narita, The Elecrtochemical Society, PV-99-38, pp. 380-389 (2000).

36.   Dybkov V.I. Reaction diffusion and solid state chemical kinetics. Kyiv: IPMS Publ., 2002.

37.   Galanov B.A., Ivanov S.M., Kartuzov E.V., Kartuzov V.V., Nickel K.G., Gogotsi Y.G., Model of oxide scale growth on Si_3N_4 ceramics: nitrogen diffusion through oxide scale and pore formation. Computational Materials Science. – 2001. – Vol. 21/1. – P.79-85.

38.   Monticelli C., Zucchi F., Pagnons A., Dal Colle M. Corrosion of zirconium diboride/silicon carbide composite in aqueous solutions // Electrochimica Acta, v. 50, 2005, p. 3461 – 3469

39. Remy H., Lehrbuch der Anorganischen Chemie, Band II, Leipzig, 1961, s.775

40. Jang G., Kieffer R., Kogler H. Korrosions-prüfungen an Siliziden der Übergangsmetalle. Werkstoffe und Korrosion. **21**, No. 9 (1970), 699 – 703.

41. Armstrong R.D., Douglas A.F. The anodic oxidation of the binary compounds of the transition elements in sulphuric acid. J. Appl. Electrochem. **2** (1972), 143–149.

42. Herranen M., Bauer A.D., Carlsson J.-O., et al. Corrosion properties of thin molybdenum silicide films. Surf. Coat. Tech. **96**, No. 2-3 (1997), 245 – 254.

43. Chyrkin A.D., Lavrenko V.A., Panasyuk A.D., et al. Oxide nanofilms formation on the surface of titanium, molybdenum, and tungsten disilicide under anodic polarization. Rep. Nat. Acad. Sci. Ukr. **12** (2006), 96 – 101. (in Russian)

44. Liu Y.Q., Shao G., Tsakiropoulos P. On the oxidation behaviour of $MoSi_2$. Intermetallics. **9** (2001), 125 – 136.

45. Cocke D.L., Schennach R., Hossain M.A., et al. The low-temperature thermal oxidation of copper, Cu_3O_2, and its influence on past and future studies. Vacuum. **79**, No. 1-2 (2005), 71 – 83.

46. Tremiliosi-Filho G., Dall'Antonia L.H., Jerkiewicz L.H. Growth of surface oxides on gold electrodes under well-defined potential, time and temperature conditions. J. Electroanal. Chem. **578**, No. 1 (2005), 1 – 8.

47. Willis G.C., Jr., Adams G.B., Van Rysselberghe P. Electrolytic formation of insulating oxide films on zirconium — II. Electrode kinetics at constant voltage. Electrochimica Acta. **9**, No. 1 (1964), 93 – 101.

List of Symbols, Abbreviations, and Acronyms

E – Young's module

ν – Poisson ratio

E_i, ν_i – elastic constants of indenter

HM – Meyer's hardness

H – hardness by Vickers

σ_s – yield stress

σ_θ – near-surface tensile stresses outside of indentation

σ_f – contact strength at tension (CST)

Y – contact strength at compression (CSC)

S – microstructural strength

C – a coefficient $HM = CY$

a – radius of contact area or half of indentation diagonal

l – crack length, calculated out of angle indentation

c – crack length, calculated out of centre of indentation

θ_0 – initial porosity

θ_c – porosity of a material at $r = a+0$

θ_k – average porosity in core

e – volumetric deformation

e_k – average volumetric deformation in core

e_c – volumetric deformation at $r = a+0$

e_{ks} – average volumetric deformation of a solid phase of core

e' – depth of pre-surface layer $e' \approx a/10$

p – average hydrostatic pressure in core

τ – average intensity of stresses of shear in core

φ, ψ – function of porosity

F – Weibull's function of distribution

m – Weibull's module (parameter of statistical distribution)

σ_0 – characteristic strength (parameter of statistical distribution)

P – loading on indenter, N

Φ – a coefficient ($H = \Phi \sigma_m$)

K_{1c} – fracture toughness

L_1, L_2 – the thicknesses of outer and inner oxide scales respectively

h_1, h_2 – chemical constants of outer and inner oxide scales

K_1, K_2 – physical constants of outer and inner oxide scales

t – time of oxidation

ξ – film thickness

i – current density

F – Faraday's constant,

V_{SiO_2} – molar volume of silicon dioxide.

v – molar volume of oxide

V – voltage drop in the oxide film

n – number of electrons in equation

n_i – concentration of diffusing ions

D_i – diffusion coefficient

k´ – effective parabolic constant.

Oleg Grigoriev

Project Manager

Appendix 1

Thermal and Electrical Properties of ZrB$_2$-SiC at High Temperatures

An Ultra High Temperature Material
Developed at IPMS Team - Kiev, UKRAINE
O. Grigoriev

Ali Sayir / RXC
NASA Glenn Research Center
Ali.Sayir-1@nasa.gov

(I) Phase Content: X-Ray Analysis

(II) Thermal Transport Properties:
- Heat Capacity (25 to 2000 °C)
- Thermal Diffusivity (25 to 2000 °C)
- Thermal Conductivity (25 to 2000 °C)

(III) Electrical Properties:
- Electrical Resistivity; Four point probe from 25 to 950 °C
- Seebeck Coefficient from 25 to 950 °C

(III) Mechanical Properties:
- Modulus via Sonic Velocity Measurements 500 to 1500 kHz

ZrB₂-SiC Phase Identification
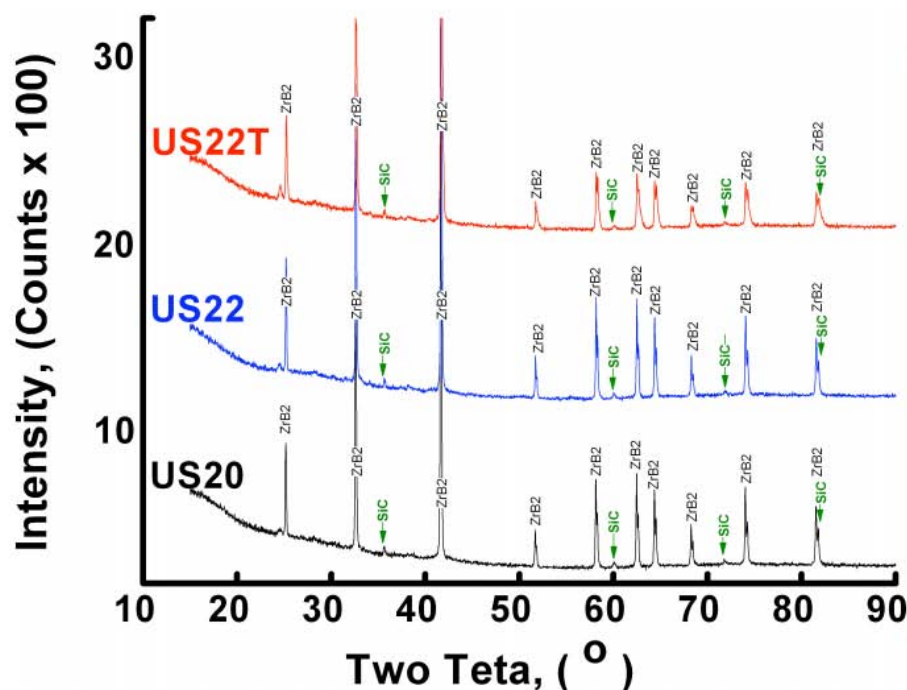
The x-ray phase identification was made with *BRUKER D8 ADVANCE*. The scans were run from 10 to 100 degrees, not much observed before 10 and past 90 degree so graph is reduced for better presentation:

- **The major phase was ZrB₂ and SiC**

- **Possible minor phase are not investigated.**

ZrB₂-SiC Phase Identification - US 22T
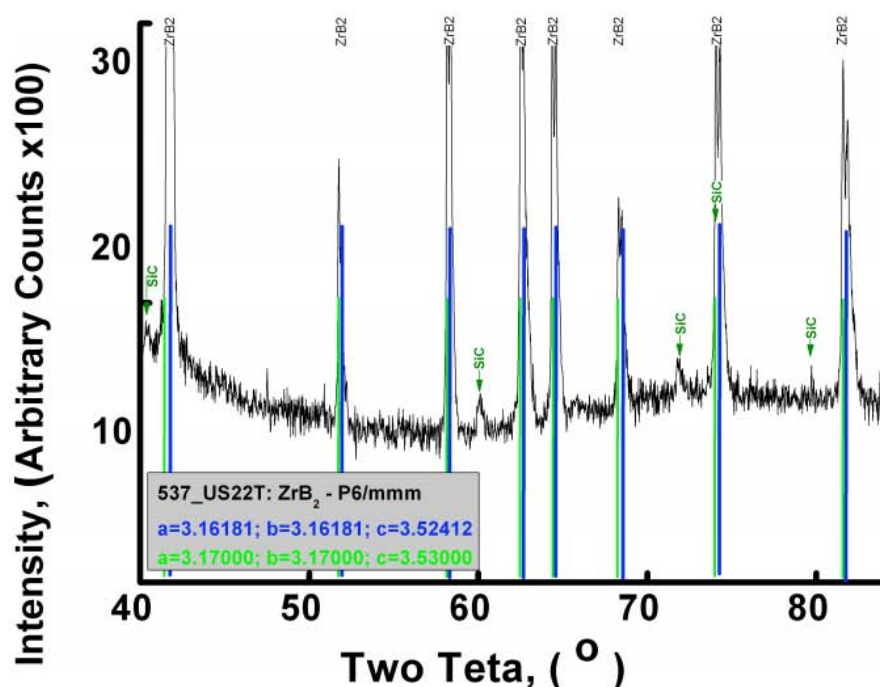
Sample 537_US22T appears to have peak separation, possibly a second ZrB₂ phase forming, both are hexagonal – Solid solution possible? The tuning of cell parameter of primitive hexagonal cell (P 6/mmm) by assuming a=3.16181, b=3.16181 and c=52412 fits the data very well (blue vertical lines). The x-ray data expected to originate from intrinsic cell parameters of pure ZrB₂ is shown in green vertical lines nad corresponds to a=3.15000, b=3.15000 and c=3.53000.

537_US22T: ZrB₂ - P6/mmm
a=3.16181; b=3.16181; c=3.52412
a=3.17000; b=3.17000; c=3.53000

Thermal Diffusivity : US20
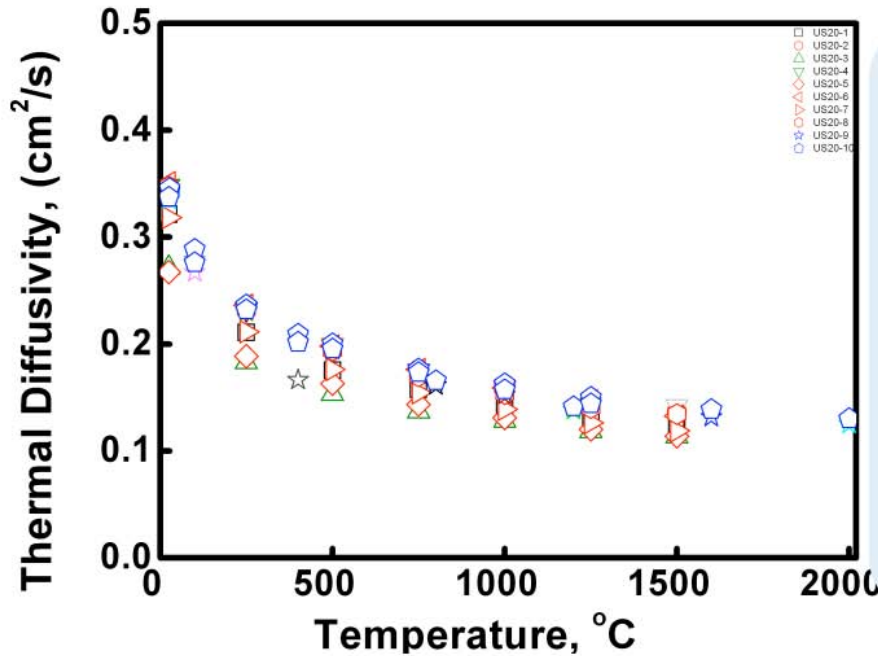
Thermal diffusivity tests were performed according to the specifications of ASTM E1461 test method. Thermal diffusivity is determined from the time interval after the flash for the sample's rear face to reach half of its ultimate temperature rise. A unique feature of the system is the full-time pulse mapping and recording capability that allows precise pulse shape and pulse width correction calculations. Standard configuration employs a 200-300μs pulse width.

Thermal Diffusivity : US22
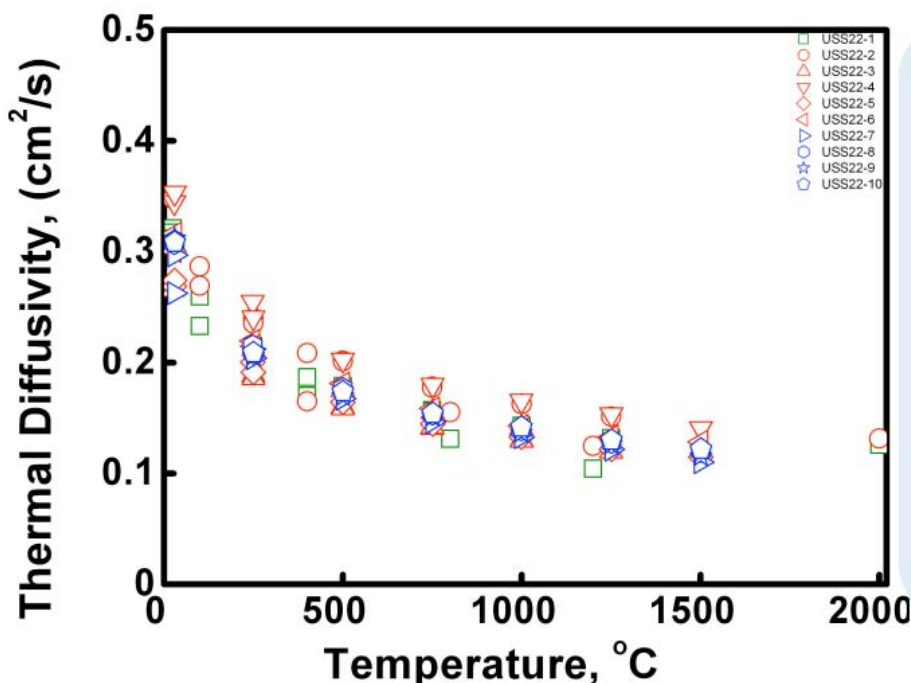
Thermal diffusivity of US20 and US22 are same for both compositions up 2000 °C. This can be stated with higher than 95 % confidence limit for whole temperature range (25 to 2000 °C)

The monotonic decrease of thermal diffusivity indicates phonon scattering characteristic even very high temperatures.

Thermal Diffusivity : US22T
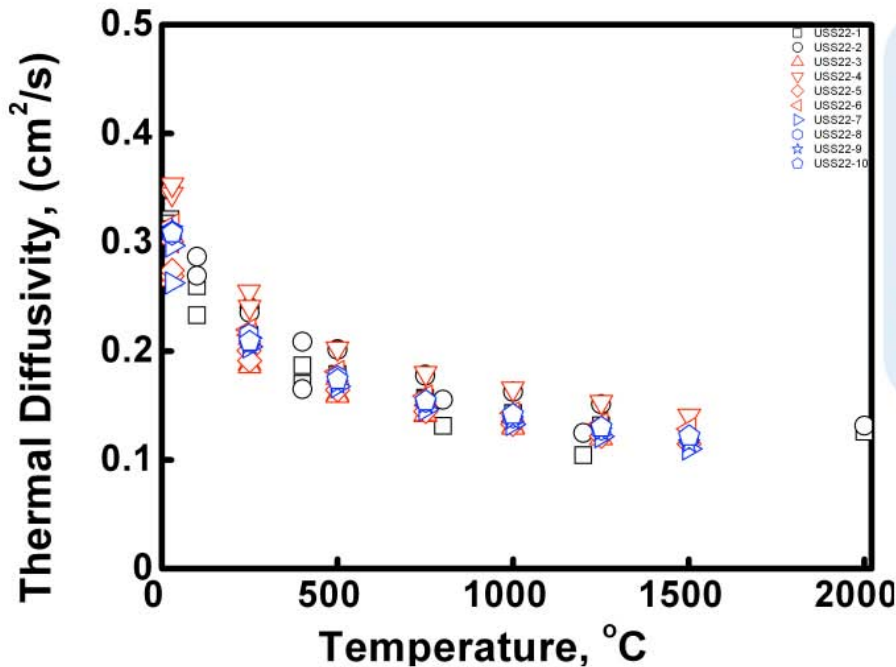
Thermal diffusivity of US22T was lower than US 20 and US22 at temperatures above 500 °C.

Microstructural characterization is required to explain the difference

Thermal Conductivity : US 20
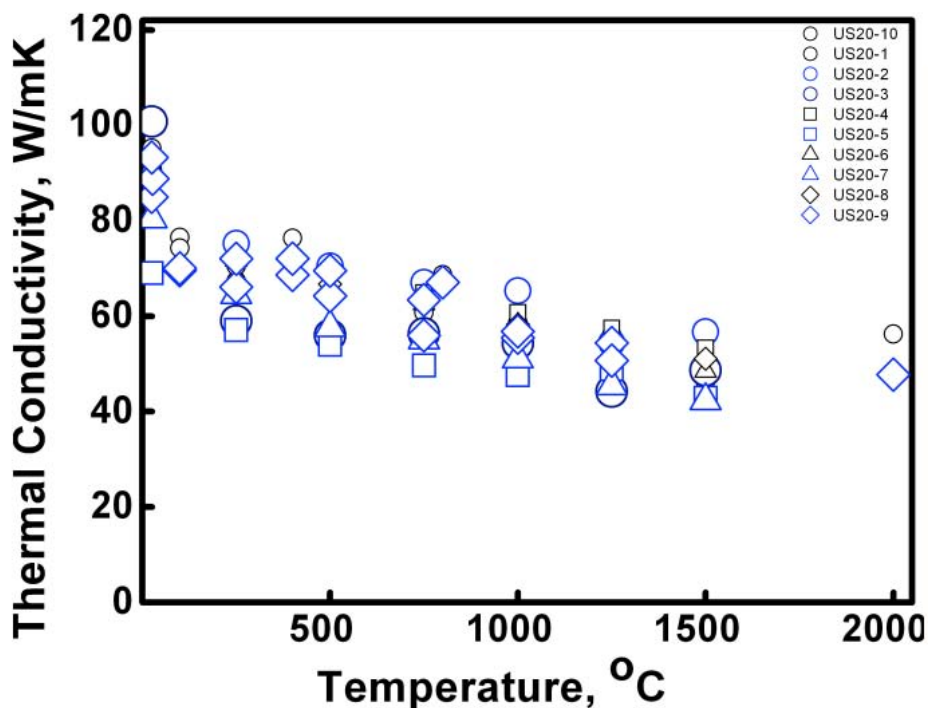
Thermal conductivity tests were performed according to the specifications of ASTM E1461 test method. The thermal conductivity derived from density, heat capacity, and thermal diffusivity measurements. Most of the estimated error expected to originate from heat capacity measurements and the error is less than 10 % of the heat capacity value.

Thermal Conductivity : US 22
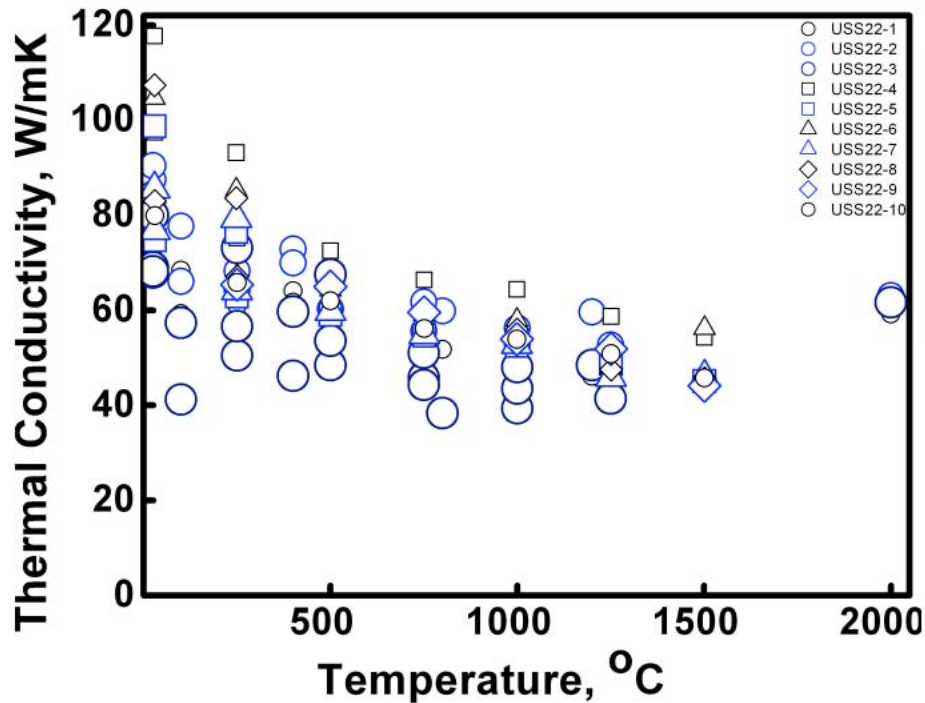
The scatter is due to sample to sample variation and additional errors originating from the heat capacity measurements.

Thermal Conductivity : US 22T
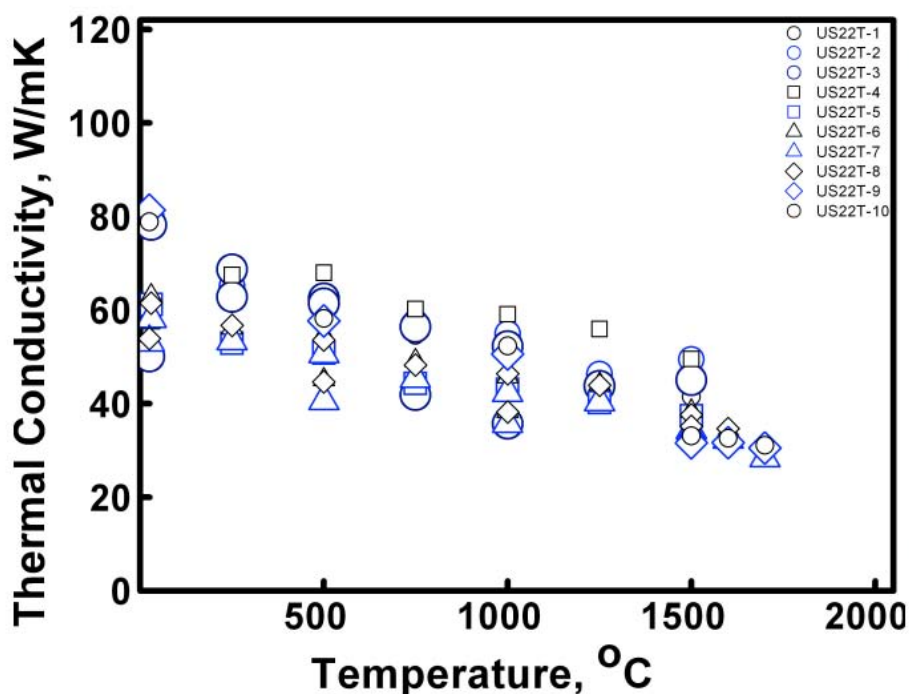
Thermal conductivity of US22T is lower than US20 and US22 at elevated temperatures. The correlation between thermal conductivity and microstructure could be investigated to elucidate property microstructure relationship.

Electrical Characterization

Impedance analysis:
Agilent 4294A, 40Hz-110Mhz, 25°C-1200°C
Agilent E4991A, 1Mhz-3Ghz, 25°C
Solarton SI 1260, 1Hz-1MHz, 25°C-1000°C, Air-10⁻¹⁰ parts O_2
SI 1296 Dielectric Interface
SI 1287 Electrochemical Interface

Ferroelectric/Piezoelectric/Pyroelectric measurements:
aixACCT TF Analyzer 2000, 25°C-250°C, up to 10kV
Bipolar, unipolar ferroelectric and piezoelectric analysis
Pyroelectric measurements
Leakage
High field capacitance and tangent delta
Radiant Technologies, 25°C, up to 10kV
Bipolar, unipolar ferroelectric and piezoelectric analysis
Leakage

Piezoelectric strain measurements:
PolyTec OFV-5000 Laser vibrometer coupled with aixACCT
MTI Technologies PhotonicTM sensor coupled with Radiant
KCF Technologies PM3001 d_{33}-meter

Other electrical characterization systems:
Lakeshore Model 665 Hall Measurement System (2 Tesla)
Ulvac-Riko ZEM3 Seebeck coefficient and four-point resistivity measurement - -70°C-950°C.
Agilent 33220A 20Mhz Function /Arbitrary Waveform Generator.

Electroding:
Physical Vapor Deposition
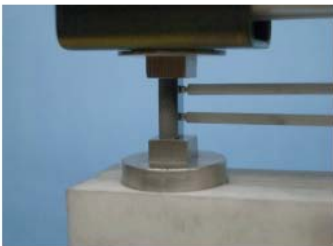
Ali Sayir (RXC / GRC)

Electrical Resistivity: US20, US22 & US22T

I) US20

II) US22

III) US22T
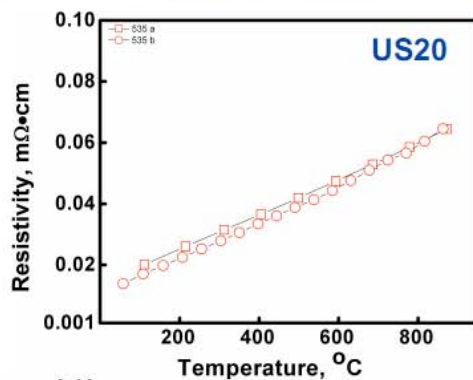
Electrical Resistivity of US20, US22 and US22T are approximately 0.2×10^{-5} Ωm range at room temperature. Resistivity increases monotonically to 0.8×10^{-5} Ωm at 950 °C.
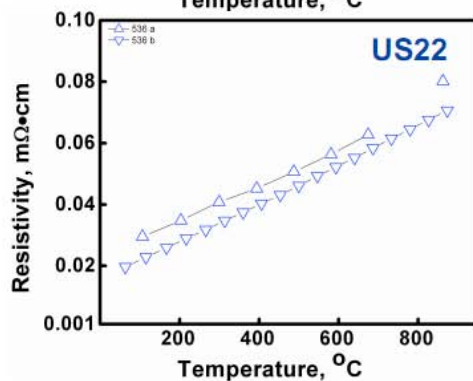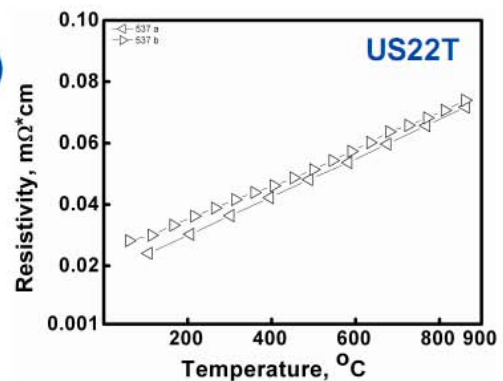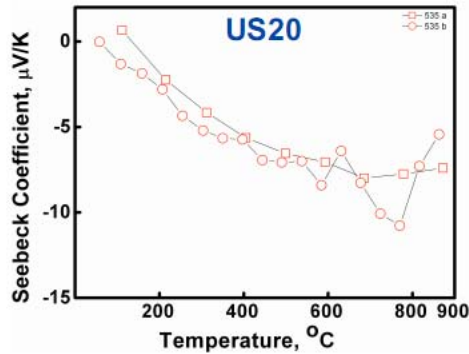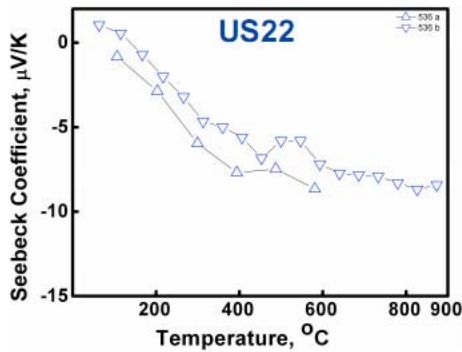
Seebeck Coefficient: US20, US22 & US22T

I)
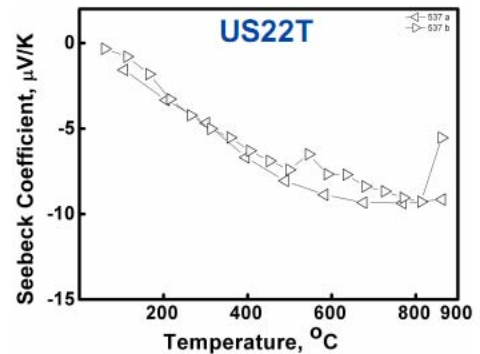

Seebeck coefficient of US20, US22 and US22T are low and less than 15 µV/K and negative.
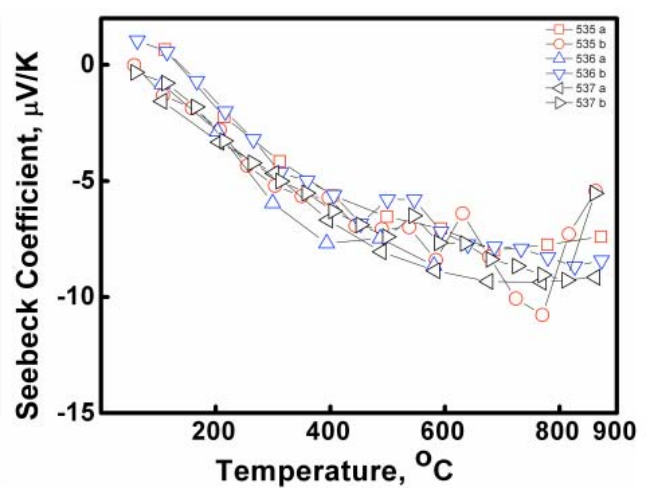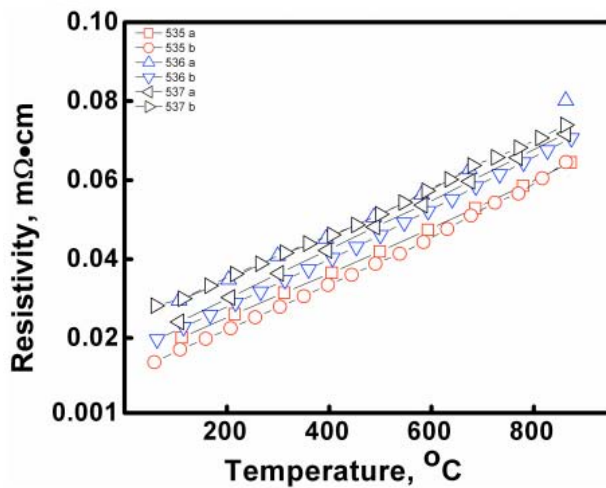
II)

III)

Transport Properties: US20, US22 & US22T

Comparison of transport properties indicates that electronicaly all US20, US22 and US22T compositions have similar characteristics: n-type semimetal with very low band gap.
The mobility and carrier concentration measurements are currently being investigated.

Thermal Transfer Properties

Flashline 5000 Graphite:
25 to 2500 °C @ inert gas

Flashline 5000 MoSi$_2$:
25 to 1600°C @ Air, O$_2$, N$_2$

Flashline LS-2 Module:
-180 to 200 °C @ air

The instruments used for the thermal transfer property measurement is the FlashLine™ 500 System that is able to perform thermal conductivity measurements with a expanded uncertainty of ±2.1 % for 95 % confidence limit. An additional systematic error is estimated to originate from temperature dependent density values. This error is minimized to zero by driving the density using expansion coefficients. The method involves uniform irradiation of a small, disc-shaped sample over its front face with a very short pulse of energy. The time-temperature history of the rear face is recorded through high-speed data acquisition from a solid-state optical sensor with very fast thermal response.
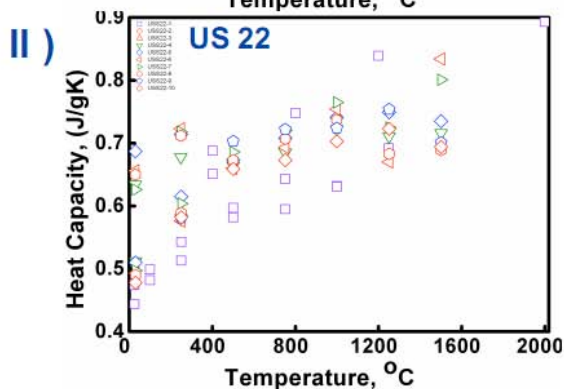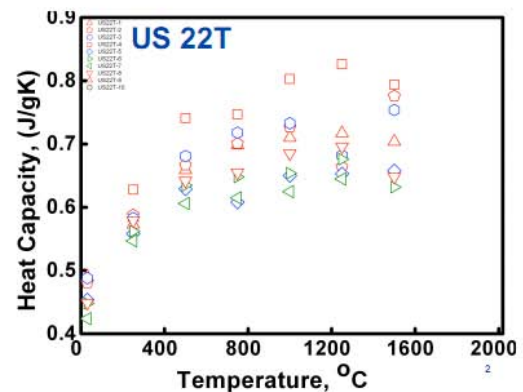
www.nasa.gov

Heat Capacity: US20, US22 & US22T

I) US 20

II) US 22

III) US 22T
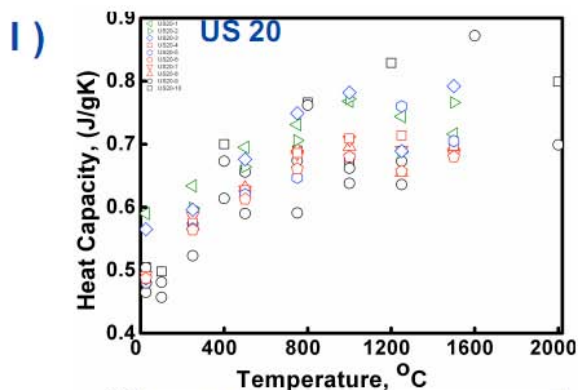
Specific heat capacity measured using multiple samples, side-by-side testing that greatly reduces overall error. The errors were in the same range as other calorimetric methods (i.e., DSC). Compare with differential scanning calorimeter data (next page).
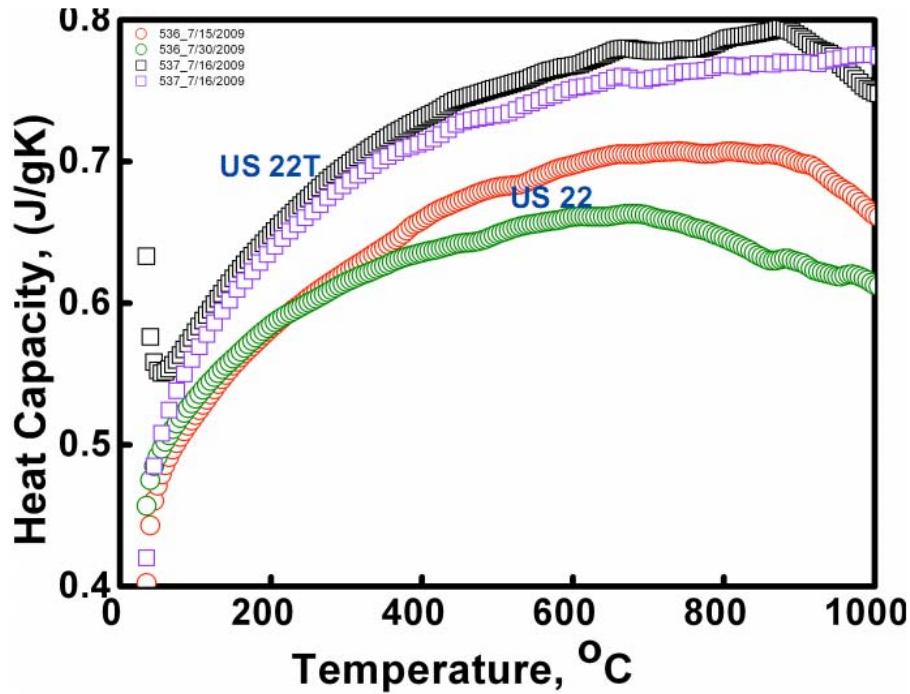
Heat Capacity: US22 and 22T

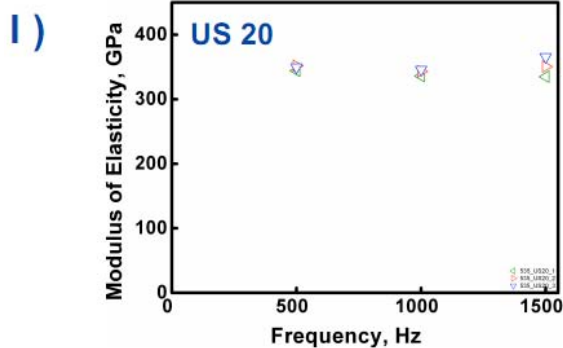## Calorimetric Method: Differential Scanning Calorimetry

Specific heat capacity measurement using differential scanning calorimeter (Nertzsch DSC 404F1).

We intend to investigate exact heat capacity with additional samples.

Modulus: US20, US22 & US22T

I)

SAMPLE	Density [kg/cm3]	Modulus [GPa]
#535_US20	5507.8	347 ± 9.3
#536_US22	5315.0	390 ± 7.1
#537_US22T	5380.5	370 ± 41

II)

III)